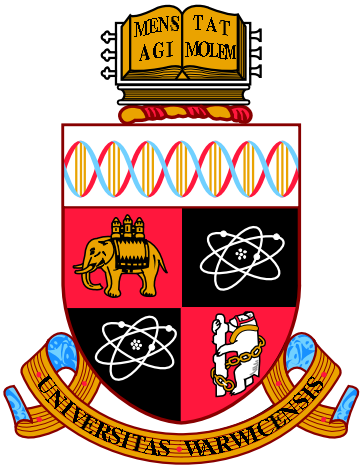

High Power Phased EMAT Arrays for Non-destructive Testing of As-Cast Steel

by

Jozef Antoni Francis Tkocz

Thesis

Submitted to the University of Warwick

for the degree of

Doctor of Philosophy

Department of Physics

1 1

THE UNIVERSITY OF WARWICK

Contents

List of Tables

List of Figures

Acknowledgments

This PhD has been a very isolating experience, and one I may not have completed if not for the support of many of the many people I have met during my time at Warwick. There are too many of you to name individually, but each of you have played some part in the support network I have relied on during these last four years, and you should know I would not have finished this thesis without that support. Special thanks go to the members of of the Warwick University mountaineering club for many enjoyable adventures; my time spent in the mountains (and even those times I was precariously suspended from the mountains) are some of the fondest memories I have of my time here. To the regulars of Physics pub Wednesday, your stimulating discussions and unwavering commitment to regular alcohol consumption have been invaluable for my sanity (though perhaps not so good for my liver), and I thank you. I would like to thank the members of Warwick's ultrasound group, in particular the inhabitants of office 244, for their help and advice during this project. Thanks also to my parents, Toni and Dawn, for their support over the years, and to Becca, for listening to my whinging for so long.

I would like to thank David Greenshields from the electronics workshop, whose work on the transducer pulsing system made the experimental sections of this thesis possible. Thanks to Rudi Kalter, Marco Duin, Daniel Ooi and Stephen Hill from Tata Steel for the provision of industrial samples. I would also like to thank Tata Steel in Europe and the EPSRC for funding this project, and should thank Steve Dixon for supervising this project.

Declarations

I declare that the work presented in this thesis is my own except where stated otherwise, and was carried out entirely at the University of Warwick during the period between October 2015 and March 2019, under the supervision of Professor Steven Dixon. The research reported here has not been submitted, either wholly or in part, to this, or any other academic institution, for admission to a higher degree. Parts of this work have been published in the following peer-reviewed journal articles:

- J. Tkocz, D. Greenshields and S. Dixon, *High power phased EMAT arrays for nondestructive testing of as-cast steel*, NDT & E Int., **102**, 47-55 (2019).
- J. Tkocz and S. Dixon, *Electromagnetic acoustic transducer optimisation for surface wave applications*, NDT & E Int., **107**, 102142 (2019).

Abstract

There is industrial motivation for the development of an online, non-destructive means of detecting internal defects during the continuous casting of steel, but to date, no methods have been reported, largely due to the hostile nature of the casting environment and the difficulty of performing volumetric inspections of thick steel slabs. Electromagnetic acoustic transducers (EMATs) have previously been identified as a means of generating and detecting ultrasound waves online during the continuous casting process for the purpose of surface quality inspection and solidification front detection, but their relatively poor transduction efficiency has thus far precluded the development of measurements for internal defects. This thesis outlines the development of a phased EMAT array for internal inspection of as-cast industrial steel samples, that would be suitable for adoption at high temperatures during the casting process.

An analytical model of the transduction mechanism of a coil-only Lorentz force EMAT device is presented and used to calculate the surface pressure magnitude for two-dimensional excitation current distributions corresponding to linear and racetrack geometry EMAT coils. These calculations are then used to support finite element models of the acoustic wavefields generated by coil-only EMAT devices. The motivation for the development of a four-element phased EMAT array is introduced, and finite element and experimental data are presented, which demonstrate a signal enhancement by a factor of 3.5 (compared to a single EMAT coil) when using the phased array system to transmit a longitudinal ultrasound pulse through a 225 mm thick as-cast steel slab sample. Defect detection experiments are then presented, demonstrating the possibility to perform image reconstruction using

mode-converted shear wave indication signals, and to detect vertical cracking defects in as-cast industrial steel slab samples by exploiting the beam-steering properties of the array.

A model of surface wave generation from a finite-width linear EMAT coil is also derived and used to determine the optimal coil width parameter for the case of sinusoidal and Gaussian current excitations. Optimal generation is shown to occur when the coil width, a, is equal to half the wavelength for the sinusoidal excitation case, and when $a/\delta c = 4.0$ for the Gaussian case, where δ is the Gaussian's width parameter and c is the Rayleigh wave speed. This result is verified using finite element and experimental data, and a means of improving the generated signal amplitude further, using phase delays to coherently add to a propagating Rayleigh wavefront, is demonstrated.

Abbreviations

- CT: computed tomography
- DPT: dye penetrant testing
- ECT: eddy current testing
- EMAT: electromagnetic acoustic transducer
- FMC: full matrix capture
- IRT: infrared thermography
- MFL: magnetic flux leakage
- MPI: magnetic particle inspection
- NDE: non-destructive evaluation
- PEC: pulsed eddy current
- SAFT: synthetic aperture focusing technique
- SH: shear-horizontal
- SNR: signal-to-noise ratio
- TFM: total focusing method

Chapter 1

Introduction

This PhD project is concerned primarily with the development of an ultrasonic measurement technique for diagnostic assessment of as-cast steel slabs, with the potential for eventual online application during the continuous casting process. Current capabilities for slab quality assessment are limited to destructive and offline methods, which neither permit comprehensive inspection of semi-finished cast products, nor permit real-time feedback to casting operators as issues arise during a casting run [1, 2, 3]. Non-destructive detection and evaluation of internal and surface-breaking defects on the casting line has the potential to dramatically increase production yields and facilitate the large-scale manufacture of novel, higher alloy content steel grades.

Non-destructive interrogation of thick metallic samples is desirable in a number of other industrial applications, such as in nuclear power station maintenance inspections, where components may be degraded or weakened due to stresses caused by thermal and mechanical cyclical loading [4, 5], or in civil engineering for the inspection of large, safety-critical structures [6, 7]. Although this thesis is concerned specifically with measurements of continuously cast steel, the contributions of this research are applicable to more general recent research efforts in the non-destructive evaluation field to develop means of performing practical measurements in difficult environments (particularly at elevated temperatures [8, 9]) and on samples that have been difficult for conventional non-destructive evaluation techniques due to their intrinsic properties (such as poor surface quality or high acoustic attenuation) or size.

1.1 Non-destructive Evaluation

Non-destructive evaluation (NDE) techniques are a range of analysis techniques used to measure material properties in such a manner as to not cause damage to the sample [10]. NDE is useful in a wide variety of situations where either economic benefits result from the ability to monitor product and asset quality [11], or where major incidents can be averted through the ability to detect and characterise defects in safety-critical components [5, 12]. Quantitative characterisation is a particular industrial demand, since common operating procedure in most industries is to permit the presence of defects below a specified safety or quality threshold [4, 13, 14]. Due to the changing requirements of industry as manufacturing, materials and engineering technologies evolve, research into NDE remains ongoing and active to ensure their implementation is economic and safe.

This thesis is concerned with the development of NDE techniques specifically for the application of defect detection during the continuous casting of steel. The remainder of this chapter is concerned with an introductory description of the steel casting process, the types of defects that can arise during casting, and the properties of cast steel that make the application of conventional NDE techniques challenging.

1.2 Continuous Casting

1.2.1 The Continuous Casting Process

Continuous casting describes the process of creating semi-finished metal products by continual extraction of partially-solidified metal from a mould. This process is more economical than the ingot casting process that it superseded, and allows for the manufacture of higher quality steel grades [15]. The first efforts to continuously cast metals with low melting points were undertaken by Laing in 1843 [16], but the high melting point and low thermal conductivity prevented the development of a reliable continuous casting method for steel until the mid-20th century [17]. The first production-scale continuous caster for steel was produced by the West German company Mannesman in 1950, which utilised a vertical design. Subsequent circular arc designs, first implemented in 1963, allowed for high-volume continuous production of steel, due to the ability to constantly feed material through the mould as the strand was still solidifying [17]. Continuous casting has since become the dominant method of steel manufacture, accounting for 96% of all steel cast worldwide in the year 2014 [18].

The continuous casting process can be described using the following steps [15] (see figure 1.1).

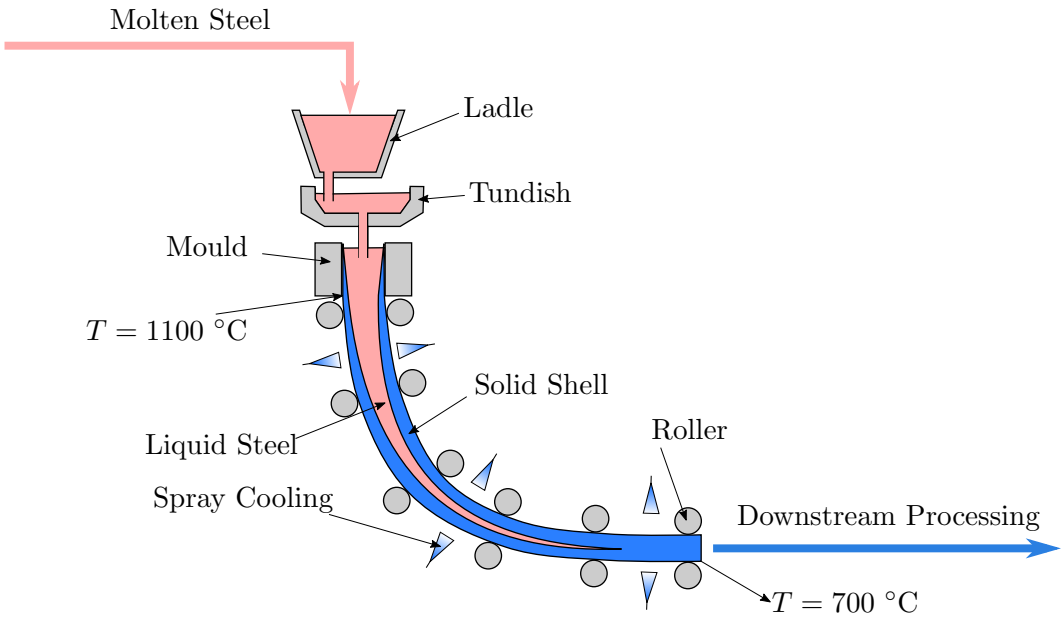

Figure 1.1: Schematic diagram of the continuous casting process.

1. Molten steel is poured from a ladle into a tundish, which controls the flow rate of the the molten steel entering the casting machine. The tundish also serves to facilitate the floatation removal of non-metallic components in the melt, to ensure a higher product quality.

2. Molten steel is fed into the mould through a nozzle. The nozzle geometry must be carefully considered to prevent defect formation in material that leaves the mould.

3. The liquid metal solidifies on contact with the edge of the water-cooled mould, giving a strand with an outer shell of solid steel, with liquid metal contained within it. The edge of the mould is powder-lubricated and the mould itself oscillated to aid steel flow. Oscillation of the mould can lead to so-called "oscillation marks", which are regular, ripple-like structures on the slab's surface. The slab's surface temperature at this stage of the cast can exceed 1100 °C.

4. Rollers support the strand as it leaves the mould. In most caster designs, the strand is passed initially through vertical rollers, before being bent and straightened into a horizontal position by the rollers. Bulging of the strand between support rollers, roll misalignment and the bending of the strand itself can all cause the development of defects in the strand. The steel is usually spray or mist cooled at this point. Realistic casting speeds can vary between

15 and 30 mm per second.

5. During this process, molten material is continually added to the tundish and solidified semi-finished product is continually cut from the strand in segments and sent for further processing. At the cutting stage, the semi-finished cast typically has quite a rough surface quality, due to oscillation marks and the formation of an oxide surface scale. The slab surface temperature at this stage is approximately 700 °C.

6. When starting a casting run, a so-called dummy bar, consisting of a rigid bar head with a claw-shaped recess attached to a flexible linked chain, is used to plug the mould. Once the liquid steel at the bottom of the mould has solidified, the dummy bar is withdrawn, pulling the strand through the support and straightening rollers. The dummy bar is then lifted away, leaving a cast strand with a claw-like protrusion; the continuous casting process is now underway and follows the steps outlined above.

Cast slab thicknesses can vary between 120-300 mm, depending on the design of the casting machine. The slab samples used in this thesis are 225 mm thick. The continuous casting of steel is a complex process with many variables that can affect the quality and structural integrity of the semi-finished product. The steel alloy composition, the presence of impurities, the geometry of the mould, the flow of molten material is fed into the caster, the roller alignment, the oscillation frequency of the mould, the lubricant used and the homogeneity of the cooling are some examples of parameters that can impinge on the quality of the steel produced [19]. Without rapid assessment of the product quality, an entire batch of material could be found to be defective at the final production stage, at great economic cost. Hence, there is industrial demand for a means of assessing product quality online in the caster itself, so that feedback can be given to the plant operators and appropriate adjustments made to the casting parameters to mitigate defect formation.

1.2.2 Defects in Cast Steel

Defects in cast steel can occur due to a variety of casting parameters. The defect geometry typically falls under one of the following descriptions (see figure 1.2):

1. Longitudinal surface cracks: surface cracks that occur parallel to the casting direction, typically several mm deep. These typically appear due to the steel alloy composition and the steel flow through the mould [20]. The type of powder lubricant, the mould oscillation, the surface roughness at the mould and the meniscus shape in the mould are the parameters that can be controlled

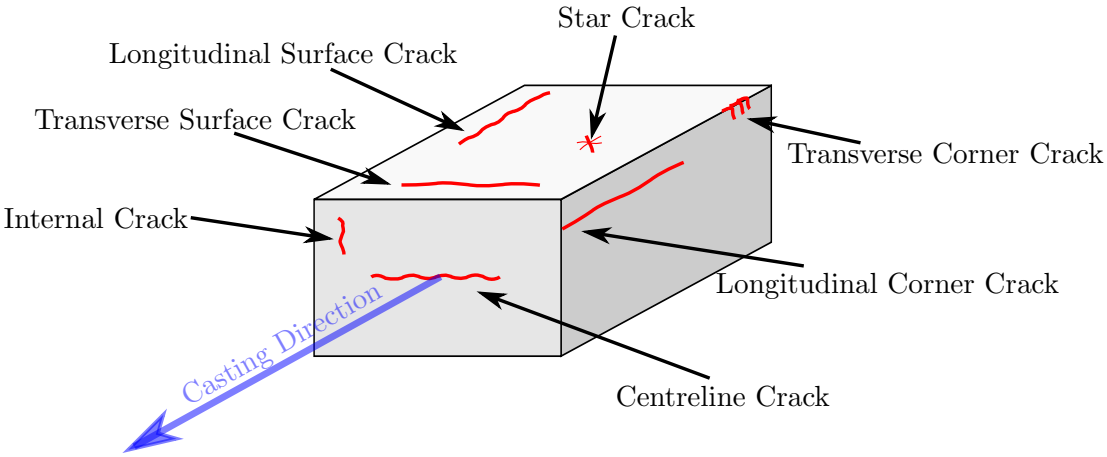

Figure 1.2: Depiction of the types of defects typically encountered in semi-finished steel products that have been continuously cast.

to reduce the number and size of longitudinal surface cracks in the product [15].

2. Star cracks: surface cracks that form radially around a localised centre point, approximately 3 mm in size. These occur due to the scraping of copper from the mould walls onto the strand, which subsequently causes localised cooling resulting in distinctive star-shaped defects. Star cracks can be prevented by chromium-plating of the mould and considering mould alignment [21].

3. Transverse surface cracks: surface cracks that lie perpendicular to the casting direction, usually in the range of 1 to 5 mm deep. These typically run along the valleys of the ripple marks on the surface of the steel from mould oscillation and appear due to stresses on the steel during straightening [15]. Transverse cracks can be avoided by using mist cooling ensure the temperature of the slab surface is reduced evenly and by trying to keep the strand out of the brittle temperature zone during the straightening stage of the cast [22].

4. Transverse corner cracks: transverse face cracks that lie at the corner of the strand. These typically occur when there are deep ripple marks or when the strand undergoes a quick temperature drop. The mitigation for transverse corner cracks is the same as for transverse surface cracks [15].

5. Internal cracks: cracks contained entirely within the volume of the strand, which can range in size from micro-scale cracking, to cracks that exist through the full thickness of the cast. These form due to tensile stresses on the solid-liquid interface during cooling as the strand becomes brittle [23]. The stresses

may be related to the strand temperature distribution, support roll misalignment or displacement, strand bulging between support rolls and tension from the straightening stage of the cast [19]. Internal cracks can be prevented by ensuring roller alignment and by carefully controlling casting temperature and cooling mechanisms to prevent reheating of the strand surface.

6. Centreline cracks: planar longitudinal voids in the centre of the strand that lie parallel to the casting direction, often several tens of millimetres in size. Usually, ferrostatic pressure from the weight of molten steel being poured through the mould is applied to the liquid steel between the two solid outer shells of the strand. When a bridge is formed between the solid shells, ferrostatic pressure is unable to ensure molten steel is pushed into the gap. Hence, because the steel density increases as it solidifies, a void is left in the centre of the slab in the region behind the site of the bridging. Centreline cracks can be prevented by ensuring correct roll alignment or controlling the casting speed with consideration for the thickness of the liquid core [15].

7. Centreline porosity and macrosegregation: small cavities and variations in alloy composition around the centreline of the cast, usually less than 1 mm in size, although typically highly clustered. The solidification of the strand is associated with a volume shrinkage, which is compensated for by a decrease in support roll gap in the later stages of the casting machine. However, improper roll settings can cause bulk flows of segregated melt, since ferrostatic pressure from molten steel higher up the caster will push the melt into areas of low pressure created by inadequate support roll pressure [24]. This movement of segregated melt leads to inhomogeneous alloy composition in the semi-finished product. Centreline porosity generally occurs simultaneously with macrosegregation. In the late stages of solidification, the centre of the strand consists of dendritic crystals, between which lies the microsegregated melt. Bulk flow of this melt (due to, e.g. improper roll separation) is impeded by the dendritic crystal structures, leading to porous centreline structures if the melt solidifies before any cavities can be filled by the flow [24].

The presence of defects in cast slabs is problematic for the steel industry; surface-breaking defects affect the aesthetic quality of the finished rolled sheets they are used to produce, which severely affects their monetary value if the intended market is one in which appearance is important, such as in the production of vehicles. Surface defects can be mitigated by processes such as scarfing or grinding, in which material is removed from the slab surface to leave a more uniform finish, although

this can be costly. Internal slab defects, on the other hand, can severely compromise the structural integrity of the finished products they are used to make, and are much more difficult to identify. Since steel manufacture is an energy-intensive industry that relies on high-volume production of a relatively low-value product, the ability to identify manufacturing defects early in the process would be extremely advantageous from an economic perspective.

Diagnostic measurements of slab quality, encompassing both destructive tests and NDE techniques, are typically applied to the semi-finished product only after several days, when the sample has cooled enough to permit application of conventional NDE tests or the cutting of samples for chemical analysis. This is of limited use to plant operators, who would require product quality feedback on timescales of minutes or hours in order to alter the machine parameters and prevent the casting of a defective batch, and hence there is demand for the development of novel NDE techniques which can provide this kind of information on the caster.

1.2.3 Grain Structures in Continuously Cast Slabs

The grain size and distribution throughout the cross section of a cast slab is influenced by the choice of casting parameters and has a large effect on the quality and mechanical properties of both the cast steel and the finished products that are rolled from it [25]. The high cooling rates and small product cross sections inherent to the continuous casting process lead to highly inhomogeneous solidification structures [26].

Locally, the steel's microstructure is defined by three parameters; the temperature gradient ahead of the interface at the solidification zone, G, the velocity of the solidification zone, v, and the alloy composition. For any given composition, a high ratio of G/v leads to a planar microstructure. As the ratio G/v is reduced, the instability of the solid-liquid interface increases, since there is insufficient thermal transport to carry heat away from the liquid ahead of the solidification front, leading firstly to a cellular microstructure and then to dendritic structures [27]. The cooling pattern of the slab therefore has a large influence on the microstructure throughout the cast's cross section.

The macrostructure of the slab is typically described by three zones (see figure 1.3). The outer edge of the cast consists of a fine-grained equiaxed zone formed by rapid solidification of the molten steel in direct contact with the water-cooled mould [28]. This layer has a variable thickness in the range of 2 - 8 mm and is compositionally similar to the liquid steel poured from the ladle [25]. The layer thickness is controlled by the steel superheat (the difference between the temperature

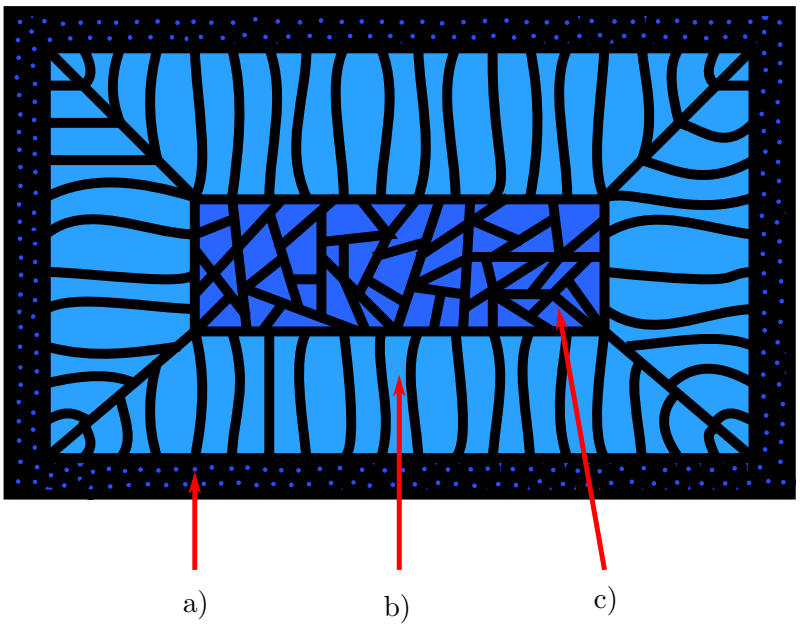

Figure 1.3: Schematic cross section of the macrostructure of a cast slab. The region at the cross section's margins (a) consists of fine equiaxed grains. Secondary cooling influences the development of columnar dendritic structures (b) that grow inwards from the outer shell. In the later stages of cooling, a coarsely-grained central equiaxed region (c) can develop.

at which liquid steel enters the mould and the liquidus temperature [29]), cooling rate and casting speed.

The interior of the cast then typically consists of a combination of columnar dendrites that grow inwards from the equiaxed margins, and a central region of larger equiaxed structures [30]. The dendritic structures usually form during secondary cooling, where the application of water spray to the outer slab surface causes large thermal gradients normal to the slab surface, and so inhibits crystal growth parallel to the slab surface [25]. The growth of the dendritic crystal structures is eventually self-limited by the increase in shell thickness and corresponding reduction in both the heat transfer rate and temperature gradient. This inhibits further growth of the dendrites and the recrystallisation of the liquid steel in the strand's centre. Dissociative nuclei and broken dendrites enter the liquid phase and form nucleation sites for solidification of the residual liquid steel, resulting in the growth of the central equiaxed zone. The low cooling rate generally leads to coarser grain structures in this region [25]. In curved casting machines, such as that depicted in figure 1.1, the central equiaxed zone is larger on the outer radius of the strand, due to the effect of broken dendrites and dissociative nuclei being brought preferentially to the outer

radius under the influence of gravity [25]. An additional consideration during this stage of cooling is the segregation of alloy components that precipitate from the melt due to bulk liquid flows around the dendritic structures, leading to locally-varying alloy compositions (as discussed in section 1.2.2 [31].)

The proportion of the relative sizes of the dendritic and equiaxed regions is predominantly governed by the superheat of the cast, although the alloy content, cast cross sectional size, casting speed and cooling pattern also influence it [32, 33]. In cases where the superheat is very high, there may be no internal equiaxed zone, so that the cast's interior consists only of columnar dendrites. Conversely, the slab interior may consist only of equiaxed grains if the superheat is very low [34, 26]. Although low superheats give largely equiaxed grains and a generally more-desirable macrostructure, low superheats cannot always be used due to the practical considerations of completely emptying the ladle [35], and because low casting temperatures can affect other measures of slab quality [26]. Typical slab casts can therefore contain dendritic structures of up to several cm in length [36, 37].

The inhomogeneous and coarse grain structures present in as-cast steel, the high casting temperatures, rough and oxide-covered surface and large sample thickness all present challenges for the non-destructive online detection of defects. The following chapter outlines conventional NDE techniques and aims to justify the choice of EMAT-based ultrasound measurements for the research presented in this thesis.

1.3 Thesis Overview

This chapter has introduced the motivation for the development of a non-destructive, online test of semi-finished product quality during the continuous casting process, and outlined the difficulties any proposed method must overcome: namely, the high temperatures of the sample under inspection, the large sample thickness and coarse grain structures, the roughness of the sample surface and presence of oxide scale. The following chapter introduces some common NDE methods and presents an argument for the development of an ultrasound-based measurement using EMATs. Thereafter, chapters 3 and 4 introduce the theory of acoustic wave propagation and theory of EMAT operation respectively.

In chapter 5, the argument that a high power device would be required to maximise the signal-to-noise ratio is made, suggesting that the dominant transduction mechanism of the EMAT would be the Lorentz force due to the dynamic field. Chapter 5 therefore contains an original derivation of the equivalent surface pressure of an EMAT device operating using this mechanism so that both the mag-

nitude of the resulting surface pressure and its time-variation can be estimated. The remainder of this chapter concerns finite element modelling of the acoustic wavefields radiated by these devices, to underpin modelling assumptions made in later chapters.

Chapter 6 presents the concept of a phased array of EMAT generators for the purpose of improving the amplitude of a bulk acoustic wave transmitted through an as-cast steel slab sample. Finite element modelling is used to determine the array element separation and width parameters that lead to optimal beam characteristics. Experiments are then performed to demonstrate the improved signal amplitudes that are possible when using the phased array generator, compared to a single-element transducer, and to demonstrate the signal enhancement when several detection elements are used. A preliminary defect detection experiment demonstrates that the largest defect indications are provided by forward-scattered, mode-converted shear waves.

Chapter 7 follows from the defect detection experiment presented in chapter 6 and investigates image reconstruction using mode-converted shear waves and an array of detection elements. Experimental measurements conducted on a 225 mm thick as-cast steel slab sample containing a 10 mm diameter side-drilled hole defect suggest that the developed experimental setup is not capable of detecting defects of this size due to the low signal-to-noise ratio of the scattered acoustic waves. Experiments are then conducted which concern the detection of larger internal vertical cracking defects by steering the incident longitudinal wave at an angle away from normal incidence to maximise insonication of the target defect. In this case, the experimental setup is shown to be capable of detecting hidden internal defects that are of potential concern to steel operators.

Chapter 8 concerns the problem of generating high-amplitude Rayleigh waves for the purpose of surface-breaking defect detection. A theoretical model of surface wave generation from a finite-width pulsed pressure source is introduced and used to derive the optimum transducer width for surface wave generation for a given Gaussian excitation pulse width. The result is then confirmed using finite element analysis and experimental measurements, before the concept of a phased array of Rayleigh wave generators is introduced for the purpose of enhancing the generated wavefront.

The thesis is concluded in chapter 9, with a summary of key results, a discussion of the next steps for this research in terms of industrial application, and suggestions for further research.

Chapter 2

An Overview of NDE Techniques

A summary of available NDE technologies is provided in this chapter, with the purpose of establishing a general overview of the field without specific reference to applications in steel casting, and to provide some context for the contributions made in this thesis. A brief discussion of the suitability of the highlighted techniques for the measurement of steel during the continuous casting process is provided at the end of this chapter as a justification for the chosen measurement strategy for this project (see section 2.8).

2.1 Visual Inspection

Simple visual inspection of a sample is perhaps the oldest form of NDE. Visible light is reflected or absorbed by the surface of the test piece and detected by the human eye, with defects indicated by changes in light intensity or colour. The reason such optical inspection is not routinely performed is that this is a time-consuming and error-prone process requiring highly experienced individuals [38], who are still constrained by the sensitivity limits of the human eye [39]. This is also only suitable as a surface inspection technique, since optical light wavelengths generally do not penetrate far into the samples most often subject to quality and integrity assessment in industry.

2.2 Dye Penetrant Testing

In dye penetrant testing (DPT), the sample's surface is coated with a dye, which is drawn into any cracks by capillary action. Upon removal of the dye, the location and approximate dimensions of any surface defects on the sample become apparent

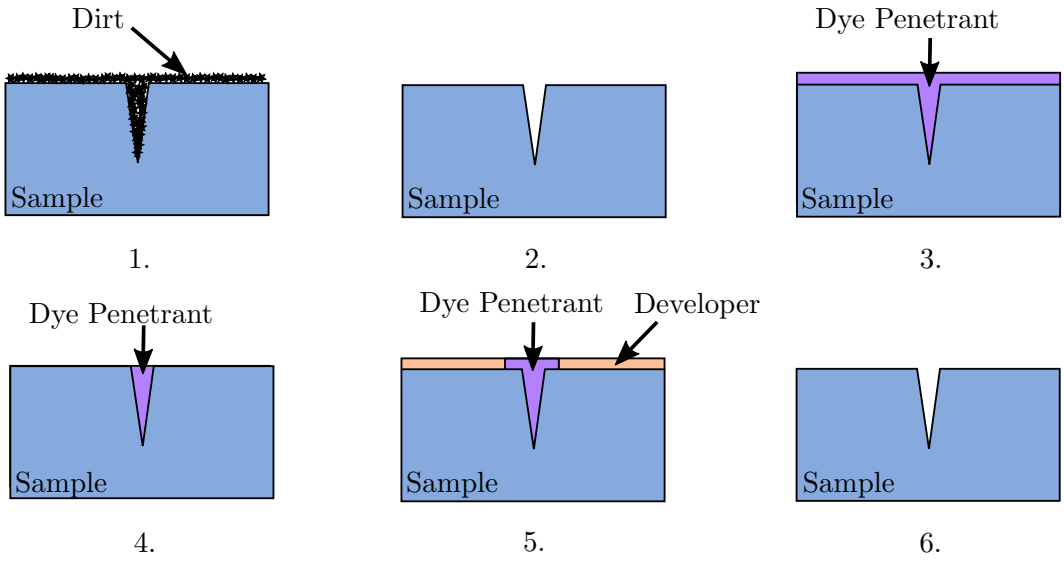

Figure 2.1: To perform a dye penetrant test, the test piece (1.) must first be cleaned (2.) before a liquid dye is applied and allowed to seep into surface breaking defects (3.). Excess dye is then wiped from the surface (4.) before a developer is applied to draw the dye from any cracks to provide indications for defect location (5.). The sample must then be cleaned again (6.).

due to the visual contrast between the dye and the sample. These principles limit a DPT test to the identification of defects that break the surface only and it cannot be used on porous materials. A DPT inspection typically involves several steps [40] (see figure 2.1):

1. The sample surface must be pre-cleaned to remove any detritus that may contaminate the dye or prevent dye ingress into defects.
2. The penetrant must then be applied to cover the sample's inspection area entirely and given time to penetrate any defects.
3. Excess penetrant dye must then be removed from the sample's surface by rinsing or wiping. Emulsifying solutions are sometimes used to assist in dye removal.
4. A developer solution is then applied to the surface of the test area, which is a substance used to draw the dye out of any cracks and provide a good contrast to the dye for easy defect identification.
5. The test piece then undergoes a visual inspection. Defects are identified through the presence of dye visible on the sample's surface, and defect dimensions in the surface plane can be approximately sized by direct measurement.

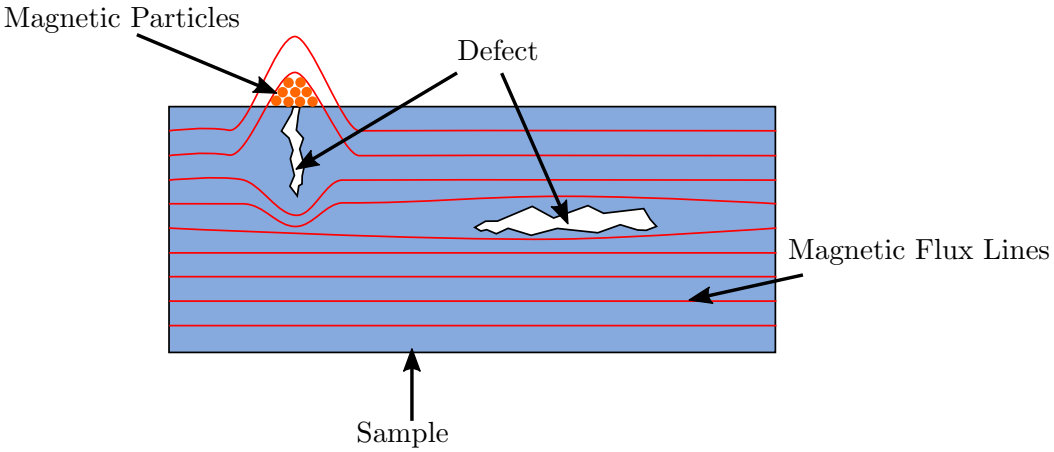

Figure 2.2: In a magnetic particle test, the sample is first magnetised before the application of a magnetic power. Powder accumulations occur where there is flux leakage, which indicates the presence of a defect.

6. Post cleaning of the sample is then performed to remove any excess dye and developer.

The DPT method is an inconvenient and time-consuming process, and is therefore unable to provide real-time defect characterisation. It is possible to run automated DPT processing lines for online applications [41], however the process still requires human inspection, the baths used for immersing the test piece in dye place limits on the sample size, and the technique remains relatively insensitive, only being able to reliably detect surface-breaking cracks with depths of 5 mm or more [40]. In addition to the ability of the inspector to carry out the above steps correctly, the inspector's eyesight and training also have an effect on the method's sensitivity [42].

2.3 Magnetic NDE Methods

Magnetic particle inspection (MPI) relies on the leakage of magnetic flux from a sample in the vicinity of a defect, and as such can only be used on materials with ferromagnetic properties. MPI is well-established for inspections of surface-breaking defects; it is possible to identify internal defects using MPI, however the defects must lie close to the surface and the test conditions must be favourable [43].

Prior to testing, the sample must first be magnetised. This is typically achieved by either directly injecting currents into the sample, placing the sample in an electromagnet coil to magnetise the test piece along its axis or inducing currents in the sample through the use of an inductor, such as a handheld alternating current magnetic yoke. Fine ferromagnetic particles (usually suspended in solution in a 'magnetic ink', although occasionally in the form of a dry powder) are then applied

to the sample surface in order to detect defects [43].

In a defect and discontinuity-free sample, the magnetic flux lines are contained within the sample and the magnetic particle distribution at the surface should be homogeneous. The presence of a defect causes flux leakage outside of the sample's surface, leading to an accumulation of magnetic particles at the site of the defect that can easily observed visually (see figure 2.2). Sensitivity can be improved by first spraying the test piece with a coloured dye that contrasts with the magnetic particle colour, or through the use of pigments that fluoresce under the application of ultraviolet light [43]. The location of the defects on the sample become immediately obvious to the inspector, as well as the orientation and length of the flaws. The magnetisation of the sample must be large enough to ensure indications occur, but not so large as to give false-positive indications. As with DPT, the eyesight and training of the human inspector also affect the sensitivity of MPI [42]. Since MPI relies on magnetisation of the test piece, these methods can only be used to test ferromagnetic materials. In addition, this method is only sensitive to surface or near-surface defects [43].

Magnetic flux leakage (MFL) is an extension of the MPI technique that is more suited to automated and quantitative measurement. The sample is prepared and magnetised in the same way, but magnetic sensors (such as Hall effect sensors or induction coils) are used to quantify the flux leakage instead of simply using powder accumulation [44]. This has the advantage of not requiring contact, or even direct access, to the sample, and the electrical output of the magnetic sensors allows for data logging and automated inspection. The technique's sensitivity is dependent on the sensor's liftoff, so the magnetic sensors often have to be held in close proximity to the sample. Other sources of noise include eddy currents from the relative motion of a sensing or magnetising magnet to the sample, surface roughness and magnetic permeability variations [45, 46]. As with MPI, MFL is only suitable for inspection of ferromagnetic objects and the sensitivity is limited to surface or near-surface defects [47].

2.4 Radiography

Conventional radiography is a shadow technique that uses highly-penetrating electromagnetic radiation to probe the internal structure of a test piece. Photon interaction with regions of high electron density causes absorption of the incident radiation and reduces the transmitted beam intensity, allowing for measurement of one or two-dimensional image projections of the object. Using many such one-dimensional measurements taken from many angles around the object, it is possible to recon-

struct three-dimensional images of the test piece using computed tomography (CT) algorithms [48]. The radiography technique used depends upon the requirements of the test; the complexity of the instrumentation and the measurement time increases with the dimensionality of the measurement. CT especially can be a computationally expensive and time-consuming process depending on the required image contrast and resolution, which makes it unsuitable for many routine industrial applications [48]. Sub-micrometer resolutions can be achieved with specialised x-ray nanotomography systems, however higher resolution scans require longer measurement times and specialised instrumentation [49].

In order to achieve sufficient penetration through the test piece, high energy photons in the x-ray or gamma range are typically used for radiographic testing. X-rays are generally produced using x-ray tubes or linear accelerator devices, and so are less portable and restrict the choice of photon energy range [48]. Gamma photons are sourced from radioisotope decay, allowing for a more portable radiation source and wider range of available energies, though the continual decay of the isotope has safety implications, the lower photon flux increases scan time and the source must be replaced once the activity becomes too low [48]. The use of radiography in industry presents a safety hazard due to the use of ionising radiation.

2.5 Infrared Thermography

Infrared thermography (IRT) is a technique related to the optical and radiographic techniques described above, in that information about the sample is obtained through measurements of electromagnetic radiation that has interacted with it. However, whereas optical techniques typically involve the measurement of photons that are either reflected from or transmitted through the sample after being applied from an external source, IRT methods measure photons that are emitted from the test piece itself. All objects above 0 K radiate an electromagnetic spectrum that can typically be well-approximated by a black body spectrum [50]. Spectrographic measurements of the radiation from an object can be used to obtain surface temperature profiles, which can then then be used to obtain information about internal defects if the nature of the object's heat source is known. Internal defects will distort the heat flow through the test piece and the will manifest as thermal anomalies in the surface temperature profile [51]. A two-dimensional image of the temperature profile can often provide sufficient information for defect identification, however more sophisticated data processing and tomographic techniques may be employed to obtain further information pertaining to the defect dimensions or to improve the SNR [52, 53].

IRT tests can usually be categorised as either active, where an external stimulus is applied to the sample, or passive, where the ambient temperature profile of the sample is measured [54]. Active thermography is more often used as an NDE technique, since heating of the sample facilitates heat flow through the bulk and hence provides a means to probe internal defects, whereas passive thermography is more suited to continuous system temperature or surface quality monitoring [55, 56]. Thermal excitation for active thermography can be achieved in a number of ways depending on the requirements of the test and the nature of the sample. Examples of excitation sources include eddy current induction heating, optical excitation using flash lamps and lasers, application of a thermal blanket or use of a hand-held heat gun [56].

IRT is desirable as an NDE method since it allows for remote sensing of internal defects, measurements can be done at high speed in real-time, can be performed when only one side of the sample is accessible and the photons emitted are typically in the infrared range (well below ionising energies, so there is no radiation hazard) [56]. The drawbacks of this technique are that the two-dimensional images produced can sometimes be difficult to interpret, sophisticated data processing may be required to obtain quantitative information regarding the defect's dimensions, the sensors are typically expensive, sensitivity is highly dependent on sample characteristics (such as emissivity and surface roughness), and that the measurement is highly sensitive to environmental conditions (humidity, background temperature, airflow etc.), so the technique will require frequent re-calibration where absolute control of environmental conditions is not possible [56].

2.6 Eddy Current Testing

Eddy current testing (ECT) is used for defect detection and evaluation on electrical conductors. It is a non-contacting technique, and so is suitable for measurements on moving and high temperature samples. It can also be used for thickness measurements of non-conductive coatings and to evaluate parameters related to a sample's conductivity such as heat treatment and alloy composition [57].

Eddy current probes consist of a coil used to induce eddy currents in the test piece. Detection is either done using the primary inductor coil or with separate detection coils (or other magnetic sensors). The eddy current coil may be modeled as the primary coil of a transformer, with the sample itself forming the secondary coil. The mutual inductance of the coil and sample form part of the imaginary component of the coil's complex impedance, hence conductivity variations in the sample will manifest in an impedance measurement of the probe coil [58]. Cracks in the test

piece obstruct eddy current flow, reducing the current density in the vicinity of the crack (the eddy current path becomes larger), hence reducing the magnitude of the magnetic field produced by the eddy currents and hence increasing the inductance of the coil while reducing its resistance.

The coil impedance measurement is sensitive to several parameters, all of which must be accounted for in order to obtain a reliable measurement. In principle, ECT provides a localised conductivity measurement on the sample's surface, so variations in material properties that affect the sample's conductivity will contribute to the impedance measurement of an eddy current scan. In addition, highly-conductive materials give rise to more intense eddy currents and hence a better SNR; measurements on poor conductors using ECT can be difficult [57]. The magnetic properties of the material strongly affect the impedance signal, so that a sample with an inherently-variable magnetic permeability profile must first be magnetised to saturation before reliable eddy current measurements can be performed [59]. The coil impedance also depends strongly on the lift off from the sample, hence accurate measurements rely on a constant separation between the test piece and the sensor or a reliable liftoff calibration measurement [60]. Rough surfaces therefore present a challenge when using ECT [61].

Conventional eddy current methods use continuous sinusoidal eddy current induction to probe a sample, allowing defects to be evaluated by the phase lag between a signal from near a flaw and a reference signal [57]. The depth of induced eddy current penetration is characterised by the electromagnetic skin depth, δ [62]:

$$\delta = \sqrt{\frac{2}{\mu\omega\sigma}}, \tag{2.1}$$

where μ is the sample's magnetic permeability, ω is the frequency of the electromagnetic radiation and σ is the sample's conductivity. Hence the depth to which the ECT method can probe is dependent on the frequency content of the input signal. In the case of conventional eddy current techniques, the ability to probe the sample bulk is limited by the use of a single frequency correlating to a single skin depth [63]. To overcome this limitation and obtain depth profile measurements, pulsed eddy current (PEC) excitations using non-sinusoidal pulses may be used. PEC techniques probe a test piece with multiple frequencies, allowing spectral analysis of measured signals to be used to infer crack depth information [64]. Multi-frequency techniques can also be used to mitigate some noise sources and improve SNR [65].

Eddy Current methods can reliably detect surface-breaking cracks with lengths over 0.75 mm and depths greater than 0.38 mm [66], and so offer a highly-sensitive

and rapid means of evaluating defects without contact with the sample, which is desirable when the sample is moving, covered in a non-conducting coating or at a high temperature. The limited penetration depth offered by eddy currents means the technique is only suitable for surface defect measurements.

2.7 Ultrasonic Testing

The basis of ultrasonic testing (UT) is the propagation of dynamic displacement fields to probe samples. Although the sample does undergo mechanical deformation, the wave amplitudes used are small, so that the stresses induced in the material lie below the elastic limit and there is no permanent deformation. If a defect is present the properties of the incident sound wave pulse are changed and this can be detected using either reflection or transmission measurements. Defect identification is possible using several techniques [67]:

- By identifying reflections from scatterers in the signal amplitude profile.
- By identifying a drop in signal intensity when the detected wave propagates through or around a defect.
- By identifying a change in the frequency content of a signal corresponding to interaction with a defect.
- From direct ultrasonic imaging using tomographic techniques.

In addition, ultrasonic testing can also be used to measure material properties that correlate with the acoustic velocity, such as microstructural texture, and for dimensional measurements [68, 69]. Ultrasonic waves can propagate in the bulk of a sample and can be localised to medium interfaces, allowing both internal and surface defects to be probed using the corresponding wave modes [70]. Calibrated amplitude and frequency measurements of waves that have interacted with the defect can provide information pertaining to the defect size, and the spatial position of defects can be calculated from measurements of pulse arrival time if the wave's speed is known [67]. Ultrasonic tests are suitable for a wide variety of samples, but may not be practical for measurements of materials with high acoustic attenuation or complex internal structures.

Acoustic waves are conventionally generated and detected in a sample using piezoelectric contact transducers, which often require the use of a liquid medium to couple the acoustic energy from the sensor to the sample. Although piezoelectric transducers are relatively efficient, the requirement for acoustic contact reduces their suitability for industrial applications, and the piezoceramics are often not robust to

high temperatures. A more complete description of piezoelectric transduction is given in section 3.6.1.

Alternative methods of ultrasound transduction include laser generation and detection, electromagnetic acoustic transducers (EMATs) and air-coupled ultrasonics. Laser ultrasound transduction is an inherently non-contacting technique, which overcomes some industrial application issues, such as high temperature operation, but lasers are relatively expensive [71], and interferometric detection of acoustic waves can be difficult on optically rough samples. EMATs are non-contact devices that can generate and detect acoustic fields in electrically-conducting and magnetic samples, though the separation must be low, special design considerations must be taken into account for high temperature operation, and they are relatively inefficient devices. More complete descriptions of laser and EMAT generation and detection of acoustic waves are given in sections 3.6.2 and 3.6.3 respectively. Air-coupled ultrasonic transduction is inherently non-contacting, although this technique is fundamentally limited in its efficiency by the large acoustic impedance mismatches present between the transducer and the air, and typically the large acoustic impedance mismatch between the air and the target. Care must also be taken to align the transducers correctly with respect to the sample's surface, to ensure the incident ultrasonic energy is not reflected or refracted to an undesired location [72].

2.8 Technique Summary and Suitability for High Temperature Steel Diagnostics

The sections detailing NDE technologies presented above relate to non-destructive measurements generally, and not specifically for the problem of high temperature steel measurements that this project aims to address. Presented here is a brief summary and assessment of the described techniques with consideration for this application, for the purpose of justifying the decision to use an EMAT-based ultrasound system in this thesis. In order to perform suitable online measurements of steel during casting, the measurement system must be:

- Capable of continuous operation on a moving sample with a rough surface.
- Capable of operating at temperatures exceeding 700 - 1000 °C.
- Sensitive to internal defects in as-cast slab samples of up to 225 mm in thickness (surface defects may also be of interest).
- Robust to the oxide scale and mould powder present in the steel mill environment.

	Contactless	High Temperatures	Internal Defects	Oxide Scale	Vibrations
Visual Inspection	✓	✓	✗	✗	✗
Dye Penetrant Testing	✗	✗	✗	✗	✗
Magnetic NDE Methods	✗	✗	✗	✗	✗
Radiography	✓	✓	✓	✓	✓
Infrared Testing	✓	✓	✓	✗	✓
Ultrasonic Testing	✓	✓	✓	✓	✓
Eddy Current Testing	✓	✓	✗	✓	✓

Table 2.1: Summary of reviewed NDE technique suitability for online measurement of internal defects in cast steel.

- Robust to the large amplitude vibrations of heavy machinery.
- Able to produce quantitative digital output for automated flaw detection, since the measurement data sets are likely to be large.

For ease of presentation, a summary is presented in table 2.1 comparing the capabilities of the discussed NDE technologies against this specification. The technologies that satisfy enough requirements to merit consideration are radiography, infrared thermography, ultrasonic testing and eddy current testing.

Radiography potentially offers a suitable method of detecting internal defects, however the high electron density of steel and relatively thick sample cross section would require either high radiation flux or long exposure times to achieve a suitable image contrast; work by Hanke *et al.* in 2004 demonstrated image acquisition times of approximately 1 minute for a 150 mm diameter circular cross section aluminium test samples [73], suggesting that this method would be impractical for online inspection of a 225 mm thick steel slab continuously extruded from the casting machine. In addition, the measurement system would be expensive to implement, and the radiation hazard posed by the system would require significant adaptations to the safety culture of the steel mill.

Infrared thermography would avoid the radiation hazard, but the system would require frequent re-calibration due to the uncontrolled ambient conditions of the steel mill. In addition, oxide scale at the sample surface would be hard to distinguish from indications of defects and the system would not be sensitive to smaller internal defects due to the sample thickness. The difficulty of exciting a transient thermal pulse in a material that is already at 700 °C would likely make this technique unsuitable for measurements of internal defects; active laser thermography measurements during continuous casting have been reported [74], however these measurements are limited to surface-breaking defects and are prone to false indications due to surface oxide scale. Thermography using thermocouple measurements

has been reported for mapping the temperature distribution in the cast strand to anticipate ruptures in the steel shell, but to date no thermographic methods have been reported for internal defect detection during continuous casting [75].

Ultrasonic testing would be most viable when using either laser ultrasound or EMAT technology, since piezoelectric sensors would be unsuitable for high temperature measurements of a moving sample with a rough surface, and the acoustic impedance mismatch between air and steel would preclude the use of air-coupled sensors. An ultrasonic system should be sensitive to both surface and internal defects, but measurement of internal defects would likely be difficult due to the high acoustic attenuation of coarse-grained steel and the high temperatures. An entirely laser-based system would be prohibitively expensive [71], since an interferometer array would be required for detection, and any system using lasers would require additional safety considerations. EMATs have been shown to be capable of operation at these high temperatures [11, 76, 77], however their design requires careful consideration.

Eddy current methods are only sensitive to surface or near-surface defects, making them unsuitable for measurement of internal defects. These techniques are also highly sensitive to sample liftoff and surface geometry, which would make distinction between genuine surface defects and surface roughness or oscillation marks difficult during data processing. However, eddy current probes should be robust to the harsh environment of the steel mill and high temperatures, and as a non-contacting technique would be suitable for online measurements of moving steel.

The two most viable candidates for online inspections of hot steel are laser or EMAT-based ultrasonics or eddy current testing. The project specification outlined in chapter 1 requires characterisation of internal defects, which leaves an ultrasound-based test as the only viable method of non-destructively probing the internal slab quality. A more complete overview of ultrasonic transduction and NDE methods is given in the following chapter.

Chapter 3

Acoustics in Solid Media

In section 2.8 a case was made for the use of ultrasonic methods to detect internal defects in as-cast steel samples. It is therefore necessary to introduce the underlying physics governing acoustic wave propagation in solids, in order to understand the challenges associated with ultrasonic detection of internal and surface-breaking casting defects, and to develop strategies for conducting the measurement. In this chapter, the physics governing the propagation of bulk acoustic wave modes in solids is discussed, along with the physical processes that occur when an acoustic wave encounters an interface and the processes that govern wave attenuation. The physics of the propagation of surface acoustic waves is also introduced, as this is relevant to the detection and interrogation of surface-breaking defects. An overview of ultrasound transduction methods and measurement techniques is then presented to provide a more complete overview of ultrasonic NDE methods.

3.1 Bulk Wave Propagation in Isotropic Solids

The equation of motion in an isotropic solid is described by the Navier equation [78];

$$(\lambda + \mu)\, u_{j,ij} + \mu u_{i,jj} + \rho f_i = \rho \frac{\partial^2 u_i}{\partial t^2}, \tag{3.1}$$

where λ and μ are Lame's first and second parameters respectively, u_i is the displacement component in the i^{th} direction, t is time, ρ is the medium's density and f_i is the component of force applied parallel to i. Note that the Einstein summation convention applies. The first term corresponds to the force due to compression or rarefaction of a volume element, the second term corresponds to rotational distortion, the third term represents external body forces. In the absence of external

forces, equation 3.1 can be written in vector notation as;

$$(\lambda + \mu)\,\nabla\,(\nabla \cdot \mathbf{u}) + \mu\nabla^2\mathbf{u} = \rho\frac{\partial^2\mathbf{u}}{\partial t^2}. \tag{3.2}$$

Since the displacement field, $\mathbf{u}$, should be continuous in three-dimensional space and should vanish as the coordinates tend to infinity, Helmholtz's theorem states that this field can be represented by the sum of a curl-free scalar field and a divergence-free vector field [79];

$$\mathbf{u} = \nabla\phi + \nabla \times \mathbf{H}, \tag{3.3}$$

where ϕ is a scalar potential field, $\mathbf{H}$ is a vector potential field and there is a condition that $\nabla \cdot \mathbf{H} = 0$. Substituting this Helmholtz decomposition into equation 3.2 and simplifying with appropriate vector identities yields [70]:

$$\nabla\left((\lambda + 2\mu)\,\nabla^2\phi - \rho\frac{\partial^2\phi}{\partial t^2}\right) + \nabla \times \left(\mu\nabla^2\mathbf{H} - \rho\frac{\partial^2\mathbf{H}}{\partial t^2}\right) = 0. \tag{3.4}$$

The solutions to this equation are given by setting the terms in brackets to zero, hence:

$$(\lambda + 2\mu)\,\nabla^2\phi = \rho\frac{\partial^2\phi}{\partial t^2}, \tag{3.5}$$

and

$$\mu\nabla^2\mathbf{H} = \rho\frac{\partial^2\mathbf{H}}{\partial t^2}. \tag{3.6}$$

These are wave equations, with propagation velocities of:

$$c_L = \sqrt{\frac{(\lambda + 2\mu)}{\rho}} \tag{3.7}$$

and

$$c_T = \sqrt{\frac{\mu}{\rho}} \tag{3.8}$$

respectively. To gain some intuition regarding the physical interpretation of these results, it is helpful to consider in isolation the individual components of the Helmholtz decomposition in equation 3.3. Setting $\nabla\phi = 0$ and recalling from the Helmholtz condition that $\nabla \cdot \mathbf{H} = 0$, the first term in equation 3.4 is removed, leaving equation 3.7 as the sole equation defining motion in the solid. Hence it follows that a displacement field consisting only of rotational components excites travelling waves with propagation speed c_T (see figure 3.1a). These are shear or transverse waves and are characterised by particle displacements perpendicular to the direction of travel.

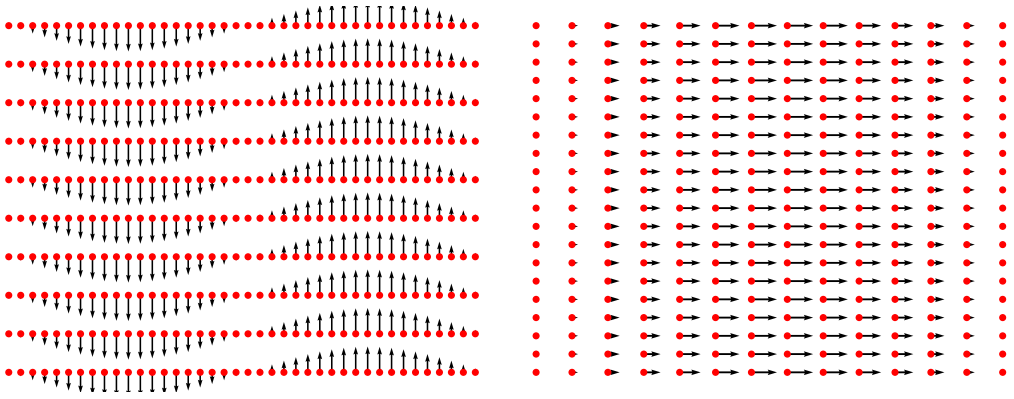

(a) (b)

Figure 3.1: Particle displacement plots, in which the particle's equilibrium position is marked by a red circle, and the displacement vector by a black arrow. Figure 3.1a depicts a divergenceless displacement field that would lead to shear wave oscillations. Figure 3.1b depicts a rotationless displacement field that would lead to longitudinal wave oscillations.

Likewise, setting $\nabla \times \mathbf{H} = 0$ removes the second term in equation 3.4, indicating that a rotationless compressed or rarefied displacement field excites travelling waves with propagation speed c_L (see figure 3.1b). These are compressional or longitudinal waves, and are characterised by particle displacements that are parallel to the propagation direction. It should be noted that equations 3.7 and 3.8 are independent of each other, and hence so are the wave modes that they correspond to.

3.2 Surface Acoustic Waves

In finite solids, there also exist waves that propagate along boundaries or interfaces known as guided waves, which can be useful for interrogating defects in samples with particular, constrained geometries. The guided waves that exist on the surface of an elastic half space are known as Rayleigh waves, and are particularly useful for the detection and measurement of surface-breaking defects in samples that are large relative to the ultrasonic wavelength.

Consider an infinite two-dimensional half space with spatial coordinates as defined in figure 3.2. As detailed in section 3.1, following Helmholtz decomposition of the particle displacement vector, it can be shown that there exist general solutions to the Navier equation that describe travelling waves with longitudinal and transverse particle motion (given by equations 3.5 and 3.6). On the surface of the infinite two-dimensional half-space, there can only exist particle motion in the x - z plane.

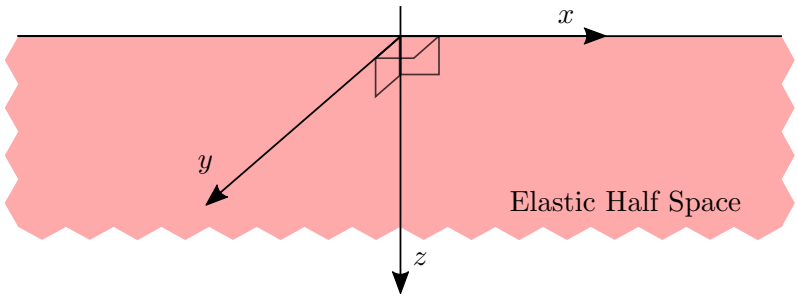

Figure 3.2: Definition of the coordinate system on a two-dimensional elastic half-space used in the Rayleigh wave derivation.

Therefore the particle displacement vector $\mathbf{u} = u_x\hat{i} + 0\hat{j} + u_z\hat{k}$, and hence the surviving components of the decomposed displacement vector (given by equation 3.3) are:

$$u_x = \frac{\partial \phi}{\partial x} + \frac{\partial \psi}{\partial z}, \tag{3.9}$$

and

$$u_z = \frac{\partial \phi}{\partial z} - \frac{\partial \psi}{\partial x}, \tag{3.10}$$

where ϕ is a scalar potential field and ψ is a vector potential field. The general plane wave solutions to equations 3.5 and 3.6 describing waves travelling along the interface in the x direction are given by [70]:

$$\phi = D_1(z)\, e^{i(kx-\omega t)}, \tag{3.11}$$

and

$$\psi = D_2(z)\, e^{i(kx-\omega t)}, \tag{3.12}$$

where D_1 and D_2 are functions describing the amplitude variation with depth. Substitution of these general solutions into the wave equations (equations 3.5 and 3.6) and discarding the unphysical solutions that increase exponentially with depth into the material yields:

$$\phi = A_1 e^{-qkz} e^{i(kx-\omega t)}, \tag{3.13}$$

and

$$\psi = B_1 e^{-skz} e^{i(kx-\omega t)}, \tag{3.14}$$

where A_1 and B_1 are integration constants. Here $q = \sqrt{1 - c^2/c_L^2}$ and $s = \sqrt{1 - c^2/c_T^2}$, where c is the surface wave phased speed ($c = \omega/k$, where ω is the angular frequency and k is the wave number). Substitution of these wave solutions into equations 3.9

and 3.10 yields the following forms for the particle displacement vector components:

$$u_x = k\left(iA_1e^{-qkz} - sB_1e^{-skz}\right)e^{i(kx-\omega t)}, \tag{3.15}$$

$$u_z = -k\left(qA_1e^{-qkz} - iB_1e^{-skz}\right)e^{i(kx-\omega t)}. \tag{3.16}$$

It is now necessary to calculate the stress components at the interface to impose physical boundary conditions. Hooke's law can be used to calculate the relevant stress components [70]:

$$\sigma_{33} = k^2\mu\left(rA_1e^{-qkz} + 2isB_1e^{-skz}\right)e^{i(kx-\omega t)}, \tag{3.17}$$

$$\sigma_{13} = k^2\mu\left(-2iqA_1e^{-qkz} + rB_1e^{-skz}\right)e^{i(kx-\omega t)}, \tag{3.18}$$

where here $r = 2 - (c/c_T)^2$. The appropriate boundary conditions describing the surface of the half-space as being free of stresses are described by $\sigma_{33} = \sigma_{13} = 0$ at $z = 0$, which leads to the following expressions:

$$rA_1 + 2isB_1 = 0, \tag{3.19}$$

$$-2iqA_1 + rB_1 = 0. \tag{3.20}$$

By rearranging equations 3.19 and 3.20 for A_1 and then eliminating B_1, it can be shown that:

$$r^2 - 4sq = 0, \tag{3.21}$$

which is the characteristic equation for the surface wave phase velocity, c. Solution of this equation requires the introduction of new variables, $\eta = k_T/k = c/c_T$ and $\zeta = k_L/k_T = c_T/c_L$, where the relations $r = 2-\eta^2$, $q = \sqrt{1-\eta^2}$ and $s = \sqrt{1-\eta^2\zeta^2}$ have been used, and $k_T = \omega/c_T$, $k_L = \omega/c_L$. Substitution of these new variables into the characteristic velocity equation then yields:

$$\eta^6 - 8\eta^4 + 8\eta^2\left(3 - 2\zeta^2\right) + 16\left(\zeta^2 - 1\right) = 0. \tag{3.22}$$

Now note that $\zeta = c_T/c_L = \sqrt{(1-2\nu)/2(1-\nu)}$, where ν is Poisson's ratio. Hence, there are three roots of η that are a function of Poisson's ratio only, and the Rayleigh phase speed c can be computed by determining those roots and setting $c = c_R$, since $\eta = c_R/c_T$. An approximate solution for the physically-relevant real root of equation

3.22 was found by Viktorov [80]:

$$\eta = \frac{0.87 + 1.12\nu}{1 + \nu}, \tag{3.23}$$

which allows for evaluation of the Rayleigh surface wave phase velocity from the elastic properties of the medium only. Note that η does not depend on ω, and hence Rayleigh waves are non-dispersive.

Rearranging equations 3.19 and 3.20 for A_1 and substituting into equations 3.15 and 3.16 gives the following forms for the particle displacement vectors subject to the stress-free surface boundary conditions:

$$u_x = A\left(re^{-qkz} - 2sqe^{-skz}\right)e^{i(kx-\omega t)}, \tag{3.24}$$

$$u_z = iAq\left(-re^{-qkz} + 2e^{-skz}\right)e^{i(kx-\omega t)}, \tag{3.25}$$

where $A = kB_1/2q$. A Rayleigh wave propagating along the surface of a half-space therefore has time-dependent displacement vector components that vary both in the plane of the surface and perpendicular to the plane of the surface. The displacement vectors in equations 3.24 and 3.25 describe retrograde elliptical particle motion at the surface with an amplitude that decays exponentially with depth into the medium over a length scale characterised by the wavelength (see figure 3.3). In sufficiently thick samples, Rayleigh waves can therefore be considered to be localised to the sample surface, in a layer with a thickness of the order of the wavelength. The implications for applications in NDE are that for maximum sensitivity, target defects must have a depth similar to, or significantly larger than, the wavelength. A Rayleigh wave incident on a surface-breaking crack with a depth much smaller than the wavelength will propagate beneath the defect relatively unaffected, since the majority of the wave's energy is contained in a layer with a thickness greater than the defect's length scale. This effect has been exploited to aid in the characterisation of surface-breaking cracks with similar depths to the wavelength; since the energy for a given frequency corresponds to a particular decay length scale, the frequency response of a broadband pulsed Rayleigh wave can be analysed to infer which frequency components are most-heavily attenuated by a surface-breaking defect, and hence to relate those frequencies to the crack depth through appropriate calibration measurements [81]. This property can also present difficulties when using Rayleigh waves for inspections of rough surfaces, since Rayleigh wave interactions and scattering from features associated with surface roughness can heavily attenuate Rayleigh waves and reduce the signal-to-noise ratios of measurements conducted

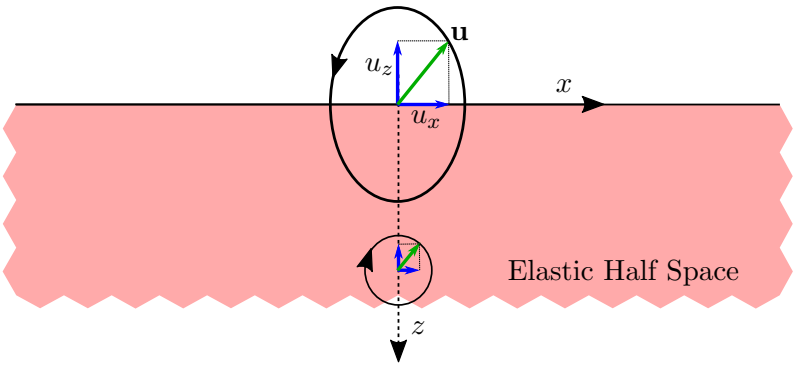

Figure 3.3: Particle displacement vectors **u**, with components u_x and u_z, for a Rayleigh wave, showing retrograde elliptical motion at the surface.

using them [80].

Equations 3.24 and figure 3.25 demonstrate that perturbations both into and perpendicular to the plane of the sample's surface lead to the generation of Rayleigh waves, which likewise can be detected by a transducer sensitive to either normal or parallel displacement vector components. Bulk ultrasound modes are most-commonly generated using piezoelectric transducers, though these cannot efficiently excite Rayleigh wave modes directly. Instead, Rayleigh waves are most-commonly excited by using an angled wedge of material attached to a piezoelectric bulk wave transducer to generate non-normally incident longitudinal ultrasound modes at the sample's surface, giving displacement vector components both into and out-of the plane of the material [70]. Rayleigh waves can alternatively be generated by ablative laser sources [11], which act as normally-acting piston pressure sources, or electromagnetically, using EMATs [82].

3.3 Acoustic Wave Interactions with Interfaces

A defect in a sample can be considered, in terms of acoustics, as a region in which there is an abrupt change in the material properties that are related to acoustic wave propagation. The boundaries of a defect are defined by the interface between the two types of media. In order to understand how an acoustic wave can be used as a probe to detect defects in solids, it is necessary to understand the behaviour of a propagating acoustic wave when it encounters such an interface.

3.3.1 Reflection and Transmission At Normal Incidence

When an acoustic plane wave encounters an interface between two media that is perpendicular to its propagation direction, the wave's energy will be partially transmitted into the second medium and partially reflected back from the interface (see

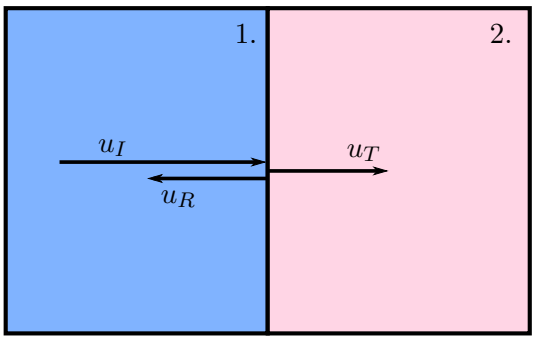

Figure 3.4: Schematic diagram showing the incidence of an acoustic wave, u_I on an interface between two media, 1 and 2. This leads to both a transmitted acoustic wave, u_T and a reflected acoustic wave, u_R.

figure 3.4). The ratio of reflected to incident wave energy and transmitted to incident wave energy is determined by the reflection and transmission coefficients of the interface respectively. In order to determine what these coefficients are, first consider a plane wave propagating in the x direction, incident normally on the interface. Due to symmetry about the y axis, the governing wave equation can be written as;

$$\frac{\partial^2 u_x}{\partial x^2} = \frac{1}{c}\frac{\partial^2 u_x}{\partial t^2}, \tag{3.26}$$

where c is the appropriate wave speed for the nature of the propagation (see section 3.1). The Ansatz solution for a travelling plane wave is given by $u_x(x,t) = A\exp(i(kx \pm \omega t))$, where the $+$ and $-$ signs in the exponent denote a wave travelling in the negative and positive x direction respectively, A is a constant representing the amplitude.

When such a wave is incident on an interface between two media, there will be partial transmission of the wave from the first medium into the second and partial reflection at the interface. It follows that the total displacement field can be represented by the transmitted wave in the second medium and by the sum of the incident and reflected waves in the first medium. Hence, the acoustic field in medium 1 can be written as;

$$\begin{aligned} u_1 &= u_I + u_R \\ &= A_I e^{i(k_1 x - \omega t)} + A_R e^{-i(k_1 x + \omega t)}, \end{aligned} \tag{3.27}$$

and in medium 2 the acoustic field is given by;

$$\begin{aligned} u_2 &= u_T \\ &= A_T e^{i(k_2 x - \omega t)}, \end{aligned} \tag{3.28}$$

where the subscripts I, R and T denote incident, reflected and transmitted waves respectively, and the subscripts 1 and 2 denote the first and second media respectively.

In order for the model to provide an accurate physical description, the displacement at the interface must be continuous. This imposes the boundary condition;

$$u_x^{(1)}(0,t) = u_x^{(2)}(0,t), \tag{3.29}$$

where the superscripts 1 and 2 refer to the media illustrated in figure 3.4. Applying this boundary condition and simplifying gives:

$$A_I + A_R = A_T. \tag{3.30}$$

It must also hold that the force per unit area at the interface is continuous, otherwise the two media would separate. The force per unit area is otherwise known as the stress, σ, and is related to particle displacement by Hooke's law [70]:

$$\sigma_x = (\lambda + 2\mu) \frac{\partial u_x}{\partial x}, \tag{3.31}$$

and the boundary condition for continuous stress across the interface is;

$$\sigma_x^{(1)}(0) = \sigma_x^{(2)}(0). \tag{3.32}$$

Calculating the stresses using equations 3.31, 3.27 and 3.28 and applying the boundary condition in equation 3.32 leads to the following condition on the wave amplitudes;

$$(\lambda_1 + 2\mu_1) k_1 (A_I - A_R) = (\lambda_2 + 2\mu_2) k_2 A_T. \tag{3.33}$$

Since $k_n = \omega / c_n$ and $(\lambda_n + 2\mu_n) = \rho c_{Ln}^2$ (where c_{Ln} is the longitudinal wave velocity in medium n), equations 3.33 and 3.30 lead to the expressions for the wave amplitude reflection and transmission coefficients:

$$R_A = \frac{A_R}{A_I} = \frac{\rho_1 c_{L1} - \rho_2 c_{L2}}{\rho_1 c_{L1} + \rho_2 c_{L2}} \tag{3.34}$$

and

$$T_A = \frac{A_T}{A_I} = \frac{2\rho_1 c_{L1}}{\rho_1 c_{L1} + \rho_2 c_{L2}}. \tag{3.35}$$

For any given material, the quantity $\rho_n c_{Ln}$ is defined as its acoustic impedance, Z_n. The above relations give the reflected and transmitted particle displacement amplitudes in terms of the acoustic impedances of the media either side of the interface, though in practice it is rarely the particle displacement that is measured. It is therefore helpful to provide transmission and reflection coefficients that relate the pressures of the incident, reflected and transmitted waves. These can be derived from the expression for stress given by Hooke's law in equation 3.31:

$$R = \frac{\sigma_x^{(R)}}{\sigma_x^{(I)}} = \frac{-A_R}{A_I} = \frac{z_2 - z_1}{z_1 + z_2} \tag{3.36}$$

and

$$T = \frac{\sigma_x^{(T)}}{\sigma_x^{(I)}} = \frac{\rho_2 c_{L2}^2}{\rho_1 c_{L1}^2} \frac{k_2}{k_1} \frac{A_T}{A_I} = \frac{2z_2}{z_1 + z_2}. \tag{3.37}$$

It is interesting to note the anticipated behaviour of acoustic waves in two limiting cases: $z_1 \gg z_2$ and $z_1 = z_2$. In the first case, $\frac{z_1}{z_2} \to \infty$, $R \to -1$, and $T \to 0$. This describes the case of a perfectly reflecting boundary, through which there is no acoustic transmission.

In the case that $z_1 \to z_2$, $R \to 0$ and $T \to 1$, there is no reflection from the boundary and all of the wave energy is transmitted through the interface. This limit describes the case in which there is no acoustic interface; although the two media may be made of different materials, if the difference in acoustic impedance is small, then the interface will not strongly reflect the acoustic wave. This is an important consideration when using ultrasound to measure defects; acoustic waves are only sensitive to substantial changes in acoustic impedance.

3.3.2 Reflection, Refraction and Mode Conversion

When an acoustic wave meets an interface between media of contrasting acoustic impedance at oblique incidence, several processes may occur. As shown in section 3.3.1, the wave energy will be partially transmitted across and partially reflected from the interface, but due to the contrasting speeds in the two media, the transmitted wave will also be refracted. Mode conversion may also occur, which describes the excitation of a wave oscillation type different to that of the incident wave at the interface [70]. This process can be understood by considering the force acting on particles due to a compressional wave near the interface. It can be shown that for any angle other than normal incidence, force components exist both parallel and

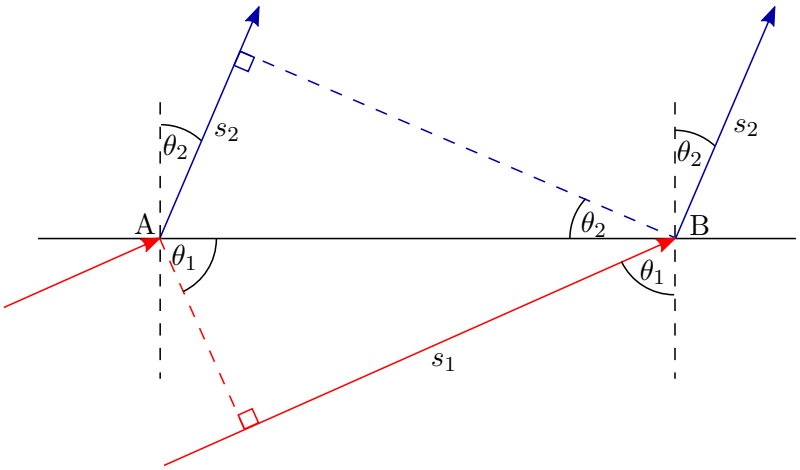

Figure 3.5: The relationship between the angle of incidence, θ_1, and of refraction, θ_2, is given by Snell's law, which can be derived by considering the distances travelled by an incident wavefront (red) and a refracted wavefront (blue) in the same time step.

perpendicular to the interface. The abrupt change in acoustic impedance at the boundary layer causes separation of these components, leading to separate compressional and shear wavemodes (see section 3.1). Likewise, by resolving the forces acting on particles due to a transverse wave at the interface, it can be shown that oblique shear wave incidence will also lead to mode conversion.

The refraction of acoustic waves is governed by Snell's law. Consider a plane wave at oblique incidence on a material interface (see fig 3.5). It is helpful to consider the wave's behaviour in terms of Huygens' principle, in which points of disturbance on an advancing wavefront themselves act as spherical point sources of acoustic waves [83]. When the edge of the wavefront encounters the interface at point A at an incidence angle of θ_1, a transmitted wave will start to propagate through the second medium at a refraction angle of θ_2. The furthest side of the wavefront must travel a distance s_1 before it encounters the interface at point B, which it does in a time $\delta t = s_1/c_1$. The wave refracted from point B will have travelled a distance s_2 in the same time, hence

$$\delta t = \frac{s_1}{c_1} = \frac{s_2}{c_2}. \tag{3.38}$$

Using trigonometry, it can be shown that $s_1 = AB\sin(\theta_1)$ and $s_2 = AB\sin(\theta_2)$. Substituting this into expression 3.38 gives Snell's law for refraction:

$$c_2 \sin(\theta_1) = c_1 \sin(\theta_2). \tag{3.39}$$

Note that this derivation contains no consideration of the mode of oscillation and so is valid for longitudinal, shear and surface waves. It is also valid for mode-converted waves; considering the point of mode conversion at the interface as a point source for spherically-propagating mode-converted waves, the above analysis gives the same relation between the angles of the reflected and refracted mode converted waves.

3.4 Acoustic Attenuation

The attenuation mechanisms affecting an ultrasonic wave can generally be described as absorption or scattering phenomena. Absorption mechanisms encompass a range of processes by which the propagation of an acoustic wave leads to energy losses. Particle displacements due to acoustic perturbations amount to deformations, which remove energy from the acoustic wave if the medium has viscoelastic properties. Absorption is therefore present in most materials and occurs even in homogeneous samples [84]. Several experimental studies indicate that the attenuation due to acoustic absorption mechanisms increases monotonically with frequency [85, 86].

Conversely, scattering processes are attributable to inhomogeneous structures in a sample. In general, acoustic wave scattering can be described as the result of the variation of elastic or acoustic properties between the medium of propagation and the structures contained within it. There are three scattering regimes characterised by the relative size of the acoustic wavelength, λ, to the characteristic size of the scatterer, d:

1. Specular scattering, in which $\lambda \ll d$. This case corresponds to the interaction of an acoustic wave with a macroscopic discontinuity [84], as described in sections 3.3.1 and 3.3.2. Thus the processes of reflection, refraction and mode conversion can all contribute to the attenuation of an acoustic wave.

2. Stochastic scattering, in which $\lambda \approx d$. In this regime, the intensity of the scattered wave is proportional to $\omega^2 d$ [87].

3. Rayleigh scattering, in which $\lambda \gg d$, which is analogous to the more familiar case of the scattering of electromagnetic radiation from particles much smaller than the wavelength. In the case of Rayleigh scattering, the scattered wave intensity is proportional to $\omega^4 d^3$ [85, 87].

It follows that the effect of scattering and absorption processes on wave intensity has a strong frequency dependence, and that greater penetration is achieved by the use of low frequency acoustic waves. The caveat is that low frequency waves are less sensitive to small inhomogeneities, so the greater penetration is compromised by a lower sensitivity to smaller targets of interest, such as defects.

The sum of all these contributing factors leads to a complex dependence of ultrasonic attenuation on a medium's properties, but in general the acoustic attenuation in a specific medium for a specific wavelength is governed by an exponential relation. The change in intensity, dI, of a linear beam of intensity I when travelling through an element of length dz is given by $dI = -I\alpha dr$, where α is the attenuation coefficient. Hence [84]:

$$I = I_0 e^{-\alpha z}, \tag{3.40}$$

where I and I_0 are the intensities at the wavefront and at the wave source respectively and z is the depth of penetration.

Note that equation 3.40 is only valid when a plane wave is considered and that real acoustic waves are generally diffuse. Geometrical attenuation describes the loss of acoustic intensity due to the spatial expansion of the wavefront. Considering the example of a point source as the origin of a spherically-propagating acoustic bulk wave, the total area of the wavefront is given by $4\pi r^2$, where r is the radius of propagation from the point of origin. It follows that the acoustic intensity at the wavefront will have in inversely proportional relationship to r^2, assuming there are no energy losses through the other mechanisms outlined above. The intensity of an acoustic wave is proportional to the square of the wave's displacement amplitude, so the displacement amplitude of a bulk wave is correspondingly proportional to $1/r$. Likewise, a wave localised to a two-dimensional surface has a wavefront with length $2\pi r$, hence an inversely proportional relationship is expected between the wave intensity and r, and the surface wave displacement amplitude is proportional to $1/\sqrt{r}$.

3.5 Scattering of Mode Converted Waves from Cylindrical Voids

The theoretical investigation of wave scattering from inclusion-like defects and cavities first received attention in the 1950s, with the investigation of acoustic wave scattering from spherical objects that may be regions of void, fluid-filled or have elastic properties [88]. Of relevance to the experimental studies presented later in this thesis, in chapter 7, is the consideration of the interaction of an incident compression wave on a cylindrically-symmetric object and the subsequent excitation and scattering for mode-converted shear waves. The directivity function of the scattered shear wave for this case, $D_s(\theta)$, was determined by Faran in 1951 to be [89]:

$$D_s(\theta) = \left| \sum_{m=1}^{\infty} -\frac{2\epsilon_m i^{m+1}}{\pi} \frac{\Delta_{2m}}{\Delta_m} \sin(\theta) \right|, \tag{3.41}$$

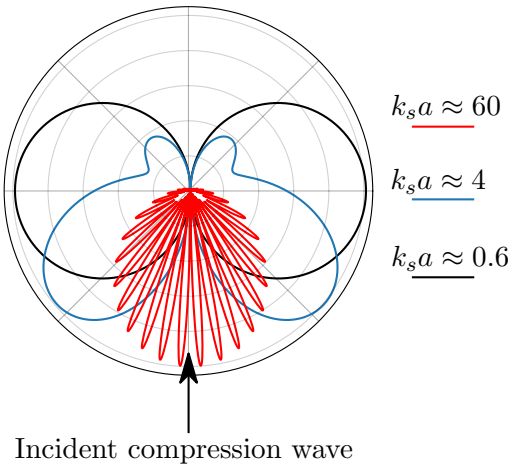

Figure 3.6: Mode converted shear wave directivity function for different values of k_sa.

where θ is the scattering angle, m is an integer, $i = \sqrt{-1}$, ϵ_m is the Neumann factor ($\epsilon_m = 1$ for $m = 0$, $\epsilon_m = 2$ for $m > 0$) and the coefficients Δ_{2m} and Δ_m are determined by the boundary conditions at the cylinder's interface. Note that the appearance of $\sin\theta$ in equation 3.41 enforces that the scattered wave field is always zero at propagation angles of 0°, demonstrating that the wave fields resulting from these interactions can be highly directional, and directed at angles away from normal incidence. For the purposes of investigating scattering from the structures relevant to this thesis, the derivation outlined in reference [90] concerns mode converted waves scattered by embedded inclusion cylinders with some elastic properties surrounded by some other medium. In the special case where the cylindrical inclusion is rigid, the coefficients Δ_{2m} and Δ_m can be written as:

$$\begin{aligned}\Delta_m = k_s^2 a^2 \left[(m^2 - m) - \frac{1}{4}k_s^2 a^2\right] \frac{\mathcal{H}^{(1)}_{(m)}(k_c a)}{k_c a \mathcal{H}^{(1)}_{(m+1)}(k_c a)} \frac{\mathcal{H}^{(1)}_{(m)}(k_s a)}{k_s a \mathcal{H}^{(1)}_{(m+1)}(k_s a)} \\ + \left(-m^3 + m + \frac{1}{2}k_s^2 a^2\right)\left(\frac{\mathcal{H}^{(1)}_{(m)}(k_c a)}{k_c a \mathcal{H}^{(1)}_{(m+1)}(k_c a)} + \frac{\mathcal{H}^{(1)}_{(m)}(k_s a)}{k_s a \mathcal{H}^{(1)}_{(m+1)}(k_s a)}\right) \\ + m^2 - 1,\end{aligned} \tag{3.42}$$

and

$$\Delta_{2m} = \frac{m^3 - m - \frac{1}{2}mk_s^2 a^2}{k_c k_s a^2 \mathcal{H}^{(1)}_{(m+1)}(k_c a)\,\mathcal{H}^{(1)}_{(m+1)}(k_s a)} \tag{3.43}$$

where k_c is the wavenumber of the compressional mode, k_s is the wavenumber of the shear mode, $\mathcal{H}^{(1)}_{(m)}(x)$ is a Hankel function of the first kind, with order m and

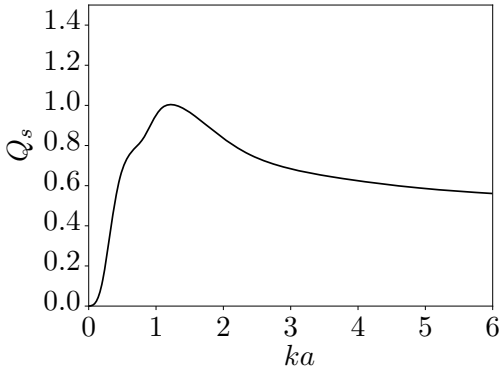

Figure 3.7: Scattering cross section for a 1 MHz shear wave mode-converted from an incident compression wave at a 6mm diameter cylindrical void in steel.

argument x and a is the cylinder radius. $D_s(\theta)$ can be calculated numerically using equations 3.41, 3.42 and 3.43. Shown in figure 3.6 is $D_s(\theta)$ calculated over an angular range from 0 - 2π for a cylinder where a = 2 mm, 0.2 mm and 30 mm in a medium where k_c = 1.05 mm^{-1} and k_s = 1.99 mm^{-1}, corresponding to elastic waves propagating at 1 MHz in typical steel sample with a compressional wavespeed of 5950 ms^{-1} and a shear wave speed of 3150 ms^{-1}. In each case, the series summation was truncated once convergence appeared to be reached, to avoid numerical instabilities associated with the computation of Hankel functions with small arguments and high orders. The results of the calculations, shown in figure 3.6, demonstrate that as the value of $k_s a$ is reduced, the directivity pattern changes from a specular interaction with a large interface at high ka, through a scattering regime with high directionality and a greater likelihood of forward-scattering occurring as the wavelength approaches the characteristic size of the scatterer, followed by a diffuse scattering regime when ka is small. In general, the angular distribution of the scattered wave becomes more complicated as ka increases, with the appearance of highly-directional lobes.

The equations above describe the angular distribution of the energy transferred from the incident compressional wave to the scattered shear wave, but do not describe the efficiency of this process. The amount of energy transferred from the incident compressional mode to the scattered shear mode is given by the appropriate scattering cross section component, derived by considering the ratio of energy in the scattered wave to the incident wave. In this case, the cross section Q_s is given by

[90]:

$$Q_s = \frac{1}{k_c a} \sum_{m=1}^{\infty} \left| -\frac{2\epsilon_m i^{m+1}}{\pi} \frac{\Delta_{2m}}{\Delta_m} \right|^2 . \tag{3.44}$$

The scattering cross section can similarly be evaluated for a given material by choosing appropriate values of k. As above, for the case of steel, the scattering cross section for a mode-converted shear wave scattered from a void cylinder with radius $a = 6$ mm is plotted in figure 3.7. The intensity of the scattered wave increases rapidly with ka at low values. This corresponds to a diffuse, Rayleigh scattering regime, where scattering efficiency approximately scales with the third power of the defect's size (see section 3.4). A local maximum appears in this case when $k \approx a$ (though this varies depending on the ratio of k_c to k_s and hence on the specific material), due to interference effects in the scattered wavefields. In the limit of higher ka, corresponding to a specular scattering regime, the scattering cross section is invariant with a. Figure 3.7 demonstrates that this limit in the efficiency of mode conversion is applicable beyond values of approximately $ka = 2$, even though the directivity is still strongly affected (as demonstrated in figure 3.6).

3.6 Ultrasound Transduction Methods

So far in this chapter, the physics governing the propagation of ultrasound in solid media has been introduced, but the experimental details concerning the transduction of ultrasound have not been discussed. This section describes methods of generating and detecting ultrasound for non-destructive testing.

3.6.1 Piezoelectric Transduction

The piezoelectric effect describes a material property in which a material undergoes mechanical strain in the presence of an externally-applied electric field, and likewise induces an electrostatic potential when an external stress is applied [91]. The origin of this effect is the noncentrosymmetric charge distribution present in the unit cells of piezoelectric materials; the charge separation means each unit cell acts as an electric dipole, and manipulation of this dipole through deformation of the unit cell by externally-applied stress leads to a change in the electric field in the unit cell [92] (see figure 3.8). In a polycrystalline material, the orientation of these electric dipoles is random, such that the net electric field when all dipoles are summed over is zero. Thus, to manufacture usable piezoelectric elements without resorting to the expensive process of growing single crystals, a poling process is used to align the piezoelectric domains along a desired axis through the application of strong external electric fields [92, 93].

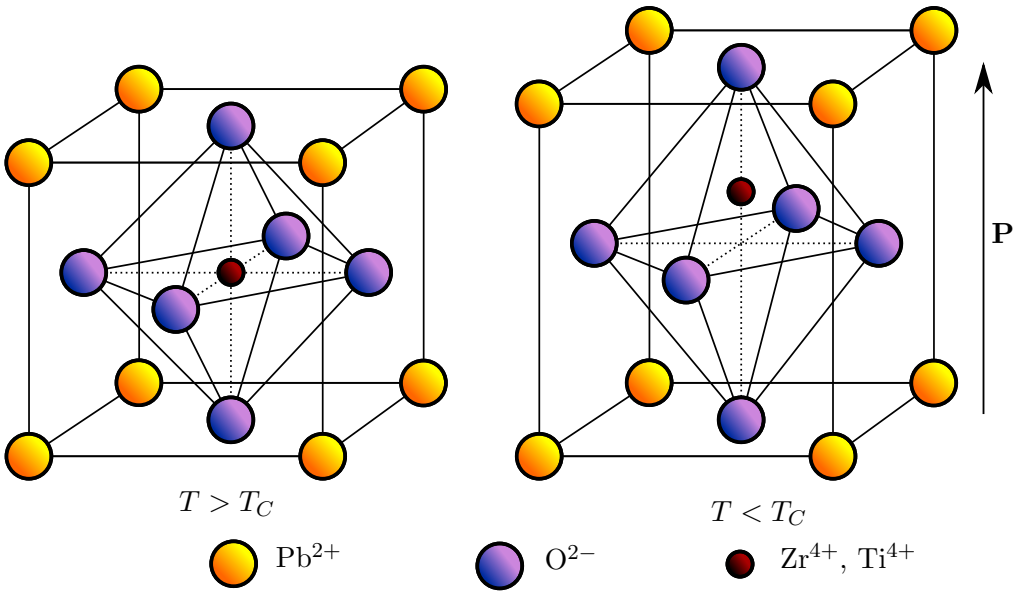

Figure 3.8: Unit cell of piezoelectric material lead zirconium titanate (PZT). Shown left is the cubic structure the material adopts when its temperature, T, is above the Curie point, T_C. As the material cools, it undergoes a phase change into the tetragonal perovskite structure shown on the right, which is noncentrosymmetric and hence has a spontaneous polarisation due to the charge separation. A strain applied across this unit cell modulates the strength of the polarisation vector, $\mathbf{P}$, which is the basic principle on which piezoelectric transducers operate.

Traditional ultrasound NDE methods involve the use of piezoelectric transducers. Whilst these are relatively efficient generators of ultrasound, they do require good acoustic coupling between the sensor and the sample, usually through the use of a liquid couplant. In order to achieve good acoustic transmission into the sample, the sensor must be held flush against the test piece and the surface in contact with the transducer must be relatively smooth [67]. The quality of the coupling is highly dependent on a number of factors including surface roughness, pressure applied to the transducer and amount of couplant used, which inhibits the reliability of many amplitude-based quantitative NDE methods and limits their use for automated measurements. These types of sensors are generally unsuitable for inspection of samples moving relative to the transducer, require direct access to the sample surface and good acoustic contact [67].

Non-contacting adaptations of piezoelectric technology have been developed to improve suitability for automated inspections, and utilise a fluid coupling medium between the transducer and the test piece in the form of an immersion bath or a pressurised jet. These suffer from greatly reduced generation and detection efficiency

due to inherent impedance differences, and (in the case of immersion ultrasound) require immersion of the test piece in liquid [72, 94]. Conventional piezoelectric technology is also generally unsuitable for high temperature inspections, since lead zirconium titanate (PZT - the most commonly used piezoelectric material due to its large piezoelectricity coefficients) undergoes a structural phase transition at a Curie temperature of approximately 360 °C [9] (see figure 3.8); the practical limit of operation for piezoelectric materials half of the Curie temperature, due to the gradual loss of polarisation at higher temperatures [8, 95]. Some piezoelectric materials do have higher Curie temperatures, up to 1210 °C in the case of lithium niobate [96], but they are less-efficient than PZT and still require good acoustic coupling; this is normally achieved by permanently bonding the sensor to the sample, since liquid couplants would evaporate at high temperatures, which prevents the use of these sensors for spot checking or scanning [97]. High temperature measurements can be performed using more efficient lower-temperature piezoelectric materials with the use of acoustic waveguides; Celga *et al.* [98] used thin, rectangular cross-section waveguide strips to sustain large temperature gradients over short distances, allowing acoustic waves to be coupled from a piezoelectric transducer to a sample without requirement for additional cooling. They reported wall thickness measurements at temperatures exceeding 700 °C. However, the propagation of ultrasound with wavelengths comparable to the waveguide's dimensions can lead to dispersive wave modes which complicate measurements, multiple reflections from the end of the waveguide can complicate interpretation of received signals, and the problem of bonded coupling is still not overcome [97, 98, 8].

3.6.2 Laser Transduction

Ultrasonic signals can be generated in solids by pulsed laser irradiation, which has the advantage of being a non-contacting technique that does not require a coupling medium [71]. The non-contacting and point-like nature of laser beam irradiation allows for ultrasonic generation in rough and high-temperature samples, however high-power laser sources are expensive and can pose a safety risk in industrial settings. Ultrasonic generation by a pulsed laser source can be categorised into the thermoelastic and ablative regimes. In the thermoelastic regime, a laser beam is used to provide localised heating to the sample's surface. This heating results in a localised thermal expansion, which produces a transient strain field and subsequent oscillatory motion which leads to acoustic wave propagation [99, 100]. In the ablative regime, a high intensity laser beam is used to ablate the surface of the test piece locally, causing the ejection of plasma from the surface. A special case of ablative

generation, using a carbon dioxide laser on a metallic surface, induces breakdown and plasma formation in the air above the sample, rather than in the sample itself [101]. In both cases, the formation and subsequent expansion of the plasma causes a momentum transfer to the surface near the beam, which produces a strain field and in turn excites acoustic wave modes [102, 103]. With the exception of the case of carbon dioxide laser ultrasound generation in metals, ablative generation is not strictly non-destructive as it typically forms an ablation pit with a depth of approximately 5 μm, though the improved wave amplitudes relative to thermoelastic generation can make this slight damage an acceptable trade-off, depending on the application [71]. The ablation damage to the sample can be minimised through the use of a sacrificial layer, such as a thin layer of paint, though this requires the surface preparation step of applying the sacrificial layer [104]. Both thermoelastic and ablative generation lead to broadband ultrasonic generation of compressional, shear and surface wavemodes, allowing for the application of a wide variety of measurement techniques on structures with a wide range of characteristic length scales [71]. Laser optics can also be used for interferometric measurements of ultrasound, however the measurements are less sensitive on optically rough, or low reflectivity surfaces and the small footprint of the laser beam can necessitate several interferometers, making ultrasonic detection using lasers technique prohibitively expensive for many applications [105].

3.6.3 Electromagnetic Transduction

Ultrasonic waves can be generated on electrically conducting or magnetic samples using EMATs [106]. EMATs are coupled to the test piece surface electromagnetically and therefore do not require mechanical contact with the sample, and so are more tolerant than conventional probes to transducer misalignment, surface roughness, sample motion and high temperatures. The operating principle of an EMAT relies on the generation of electromagnetic fields in the test piece at its surface (using induction coils and permanent magnets), which interact with induced eddy current distributions or magnetic domains in the sample to induce mechanical strain, and subsequent acoustic wave propagation. The primary operating principle of most EMAT designs is the Lorentz mechanism, which induces mechanical forces in conducting materials by moving conduction band electrons with transient magnetic fields. In magnetic materials other mechanisms are present; namely, magnetisation forces, and the magnetostrictive effect [106]. A more complete overview of the physics of EMAT transduction is presented in chapter 4.

Regardless of the intended transduction mechanism, most EMAT designs rely

on a bias magnetic field. Early EMAT designs relied on electromagnets to generate a bias field, although the introduction of strong rare-earth magnetic materials with large remnant magnetic fields has made permanent magnets made from materials such as NdFeB popular for use in most EMAT applications. Such permanent magnet EMAT designs are limited by the Curie temperature and the remnant magnetic field of the magnet (≈ 300 °C and 1.4 T respectively [107]) and must be actively cooled for operation above the Curie temperature [108]. Pulsed electromagnet designs may be used, as these are not limited by a Curie temperature and can produce fields with variable strength, though the supporting electronics for these designs are more complex [109]. Recent investigations have been undertaken into self-field generation with EMATs, where the dynamic field from the inductor coil itself is used to interact with the eddy currents and generate ultrasound, removing the need for a bias field altogether [110, 111].

EMATs are inefficient generators of ultrasound and are only suitable for measurements on conducting samples or samples with high magnetostrictive coefficients. However, the non-contacting and repeatable nature of their generation makes EMATs useful sensors when designing automated scanning systems and probes that operate at high temperatures [112, 11]. EMAT efficiency can be enhanced when used on ferromagnetic samples due to magnetostrictive generation in the sample, and this phenomenon has been exploited for diagnostic tests of boiler tubes, which develop a thick ferromagnetic oxide coating with high magnetostrictive coefficients which would otherwise have to be removed for conventional ultrasonic inspection [113].

3.7 Ultrasonic NDE

This chapter has so far introduced the underlying physics of acoustic wave propagation and the methods by which ultrasound can be generated and detected experimentally. The following section outlines some specialised areas of ultrasonic NDE that are still areas of active research.

3.7.1 Ultrasound Arrays and Imaging

Conventional ultrasound tests involve the use of a single element piezoelectric probe, most-commonly operated as a send-receive transducer. The incident acoustic wave is generated by the transducer, and the same sensor is used to measure the arrival time of reflected signals; knowledge of the acoustic wave speed in the inspection material and accurate measurement of reflected pulse arrival times allows for calculation of the ultrasound path length, and hence for defect size and position quantification [10, 114]. The limitation of these tests is that they only introduce the incident

ultrasound at a single incidence angle and require manual or mechanical scanning in order to provide information about a plane or volume of material.

Ultrasound transducer arrays consist of the close arrangement of many individual transducers (up to 256 have been reported for NDE applications, with the possibility for more with multiplexing [115]) and offer a number of advantages over conventional, single element transducers. If the array elements are sufficiently small, each can be considered as an individual point source of acoustic waves. Application of appropriate time delays (known as delay laws) when sending ultrasonic signals introduces corresponding phase shifts in the generated acoustic field, which allows for electronic manipulation of the resulting wavefield through coherent interference. Time delays can be applied so as to steer the generated beam, which allows for a range of inspection angles to be covered from a single location, or alternatively delay laws can be applied so as to focus the beam at a chosen point [115]. Since beam directivity and positioning is controlled electronically and not mechanically, piezoelectric phased array probes overcome the inherent unreliability of traditional piezoelectric contact coupling, where acoustic contact must be broken and re-made between adjacent points in a scan. Phased array probes are therefore capable of performing ultrasonic imaging scans, since intensity variations between adjacent pixels in the image can be attributed to the acoustic properties of the sample, rather than artefacts arising from unreliable coupling [116].

Traditional phased array imaging takes the form of B-scanning. In a phased array B-scan, time domain A-scan signals are recorded as a function of the beam's steering angle and plotted as a colourmap [114]. Since the time that a signal arrives at a transducer is dictated by the path length of that signal and the wave propagation speed, signals appearing at a time t can be correlated with a spatial position in the sample, however the features in a B scan image do not directly match the depth at which a scatterer lies, since reflections are recorded over a range of spatial positions at the surface of the sample, and because mode-converted signals complicate the determination of the ultrasound path length. B-scan images hence require some effort to interpret and do not produce direct images of internal defects, but have the advantage of being easily produced in realtime, due to low computation costs [117].

B-scan imaging suffers from resolution limitations related to manipulation of the acoustic beam itself, which reduces its suitability for imaging smaller defects [118]. Improvements in readily-available computing power for data processing in the early 2000s allowed for the development of alternative imaging methods with higher spatial resolutions, such as the total focusing method (TFM), which allows direct ultrasonic imaging of defects in a three-dimensional volume beneath the transducer

(or in a two-dimensional plane within that volume) [119]. This imaging algorithm requires the use of a phased array probe and is more computationally-expensive than B-scan imaging, but has a much finer spatial resolution, since there is no manipulation of the acoustic beam [118]. TFM imaging is performed entirely in post-processing, which means that data acquisition must be performed prior to the TFM image calculation. The recording method employed is the full matrix capture (FMC), in which each element of the array is sequentially individually pulsed, while all elements are simultaneously used as receivers [120]. In doing this, a matrix can be constructed with data corresponding to each possible generator/receiver pair. Post-processing of these data to reconstruct an image involves the definition of a grid, onto which the image should be computed. For each point, or pixel, in this grid, the expected arrival time of a signal traveling along a path from each generator to each receiver via this point is calculated. The data point at this calculated time in the A-scan corresponding to the generator/receiver pair is then added to the brightness value of this pixel. The algorithm iterates across the defined image space, through all transmitter/receiver pairs, to reconstruct a brightness image that is a sum of the contributions from each generating element. Mathematically, this is expressed as [118]:

$$I(x,y) = \left| \sum_{t,r} h_{t,r} \frac{\sqrt{(x_t - x)^2 + y^2} + \sqrt{(x_r - x)^2 + y^2}}{c} \right|, \tag{3.45}$$

where $I(x,y)$ is the intensity at point (x,y) in the image space, $h_{t,r}$ is the time domain A scan data matrix (with subscripts t and r denoting the transmitting and receiving elements), x_t and x_r are the x positions of the transmitting and receiving elements respectively and c is the ultrasonic wavespeed in the sample. The amplitude envelope function of the time domain data, calculated from the Hilbert transform, is usually used to populate the matrix h to remove artefacts associated with wave interference. One drawback of the TFM is that it requires prior knowledge of the ultrasonic wavespeed in the sample, making image reconstruction particularly difficult if the wavespeed is not constant. Implementation of the TFM in layered test pieces with complex geometries is non-trivial, since wave refraction at any interfaces must be accounted for [120].

Care must be taken when designing phased arrays to ensure that artefacts associated with the finite element size do not arise in the transmitted beam. Real phased arrays do not consist of an infinite number of infinitesimal point sources; the elements themselves are finite, and so do not behave like point sources once the width is comparable to the wavelength, which gives rise to side lobes in addition

to the main beam (the same is true of single element transducers) [121]. The finite spacing of sources is equivalent to a diffraction grating, so grating lobes can occur in the transmitted field. Both side lobes and grating lobes are undesirable because they reduce the directivity of the beam and hence reduce the SNR, and reflections from these lobes can lead to false attribution of indications at a given focus or incidence angle [122]. To avoid the presence of lobe artefacts, the array should adhere to the diffraction limit, in which the array elements are spaced $\lambda/2$ (or less) apart [123]. These considerations set limitations on the practically-achievable operating frequency of arrays constructed using current manufacturing techniques.

Since each individual element must have a relatively small footprint, workable signal-to-noise ratios are most-practically achieved by using efficient piezoelectric materials, such as PZT, to generate and detect the ultrasound for each channel [115]. Most conventional phased array probes are therefore not suitable for many industrial applications, since they require liquid coupling to the test piece and are made of materials not robust to high temperature applications. Some studies have reported the development of phased arrays using alternative transduction mechanisms more suitable for specific applications; for example, a low power phased EMAT array has been reported that uses coded excitation to improve the signal-to-noise ratio [124].

Chapter 4

Electromagnetic Transduction of Acoustic Waves

In section 2.8 the case was made for an EMAT-based ultrasonic system for defect detection during the continuous casting of steel. The physics of ultrasonic wave propagation was discussed in chapter 3, along with a brief overview of experimental transduction techniques. This chapter elaborates specifically on electromagnetic acoustic transduction mechanisms, since these form the basis of the experimental measurements presented later in this thesis.

4.1 Electromagnetic Acoustic Transducers

Electromagnetic generation of acoustic waves in solid media was first discovered accidentally during experimental studies of helicons (low frequency, circularly polarised electromagnetic waves that propagate in bounded plasmas in the presence of a magnetic field [125, 126, 127]) at cryogenic temperatures in a single crystal aluminium samples [128, 129]. The experimental observation of acoustic resonance coupled to the helicon modes lead to initial speculation that this phenomenon was related to the physics of helicon propagation [128], but subsequent investigations first demonstrated that acoustic wave generation could occur well outside the regime where the acoustic and helicon phase velocities coincide [130], and later demonstrated that acoustic wave generation was possible in large, polycrystalline metal samples at ambient temperatures and in the presence of relatively low bias magnetic fields [131]. The effect was therefore attributed to classical physical effects, and the realisation that the required conditions for the phenomenon were not as restrictive as initially thought made it possible to investigate applications in solid state physics and non-destructive examination of materials [129].

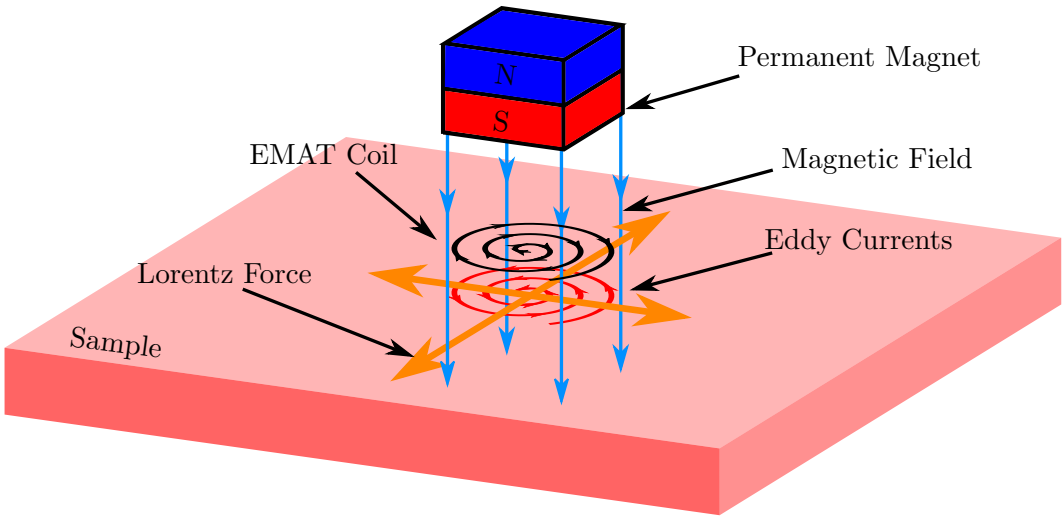

Figure 4.1: Schematic diagram of a typical EMAT configuration demonstrating the Lorentz mechanism. A typical EMAT usually consists of a magnet, which provides a static bias field, and an induction coil, which induces dynamic magnetic fields near the sample's surface.

The advantages of electromagnetic generation of acoustic waves were identified early, as a means to overcome the inherent limitation of piezoelectric generation, which is that there must be good acoustic contact between the transducer and the test piece. This made possible the development of industrially-robust ultrasound sensors which could operate at some small distance from the samples and were therefore more tolerant to surface roughness and coatings [132, 133], which could operate at elevated temperatures due to the ability to protect the requisite sensor components from hot samples [11, 108, 109], which can operate on samples in motion [132, 11], and which have a more reliable coupling efficiency between individual measurement point when performing scanning measurements [11, 82].

The components of a typical EMAT sensor are an inductor coil and a bias permanent magnet or electromagnet, or arrangement of several magnets (see figure 4.1). The arrangement of the coil and magnet(s) in an EMAT are dependent on the specific intended application of the device. Careful design of the inductor coil and consideration of the bias magnetic field geometry allows for control over the direction and distribution of forces generated in the sample's surface, and hence some control over the mode of oscillation, polarisation, directivity and frequency content of the ultrasound wave that is generated or detected by the sensor [106]. This allows for the transduction of wavemodes and wavefront geometries that can be difficult to generate and detect when using piezoelectric transducers [82, 134, 135].

The basic principle of operation is that the induction coil is used to generate a dynamic magnetic field within the sample's electromagnetic skin depth, which then is used to modulate the application of mechanical forces through one of three transduction mechanisms (outlined in detail later in this chapter). The same procedure for quantification of electromagnetic ultrasound generation applies in each case as follows:

1. Calculation of the electromagnetic fields induced in the sample.
2. Calculation of the resulting body forces.
3. Calculation of the resulting acoustic fields.

Item 1 of this list is dependent on the geometry and electrodynamics of the specific application, and can be computed analytically in some simplified cases (see chapter 5 for an example as applied to coil-only EMAT generation). Item 3 concerns the wave fields generated by a stress distribution, and again can be computed analytically in simplified cases, or evaluated numerically. The remainder of this chapter concerns the physics of item 2; namely how mechanical forces are induced in a sample electromagnetically, provided the requisite electromagnetic fields are known.

It is now necessary to introduce the physical laws governing electrodynamic interactions as described by Maxwell's equations. Hereinafter, the total magnetic field in a material, $\mathbf{B}$, is defined as:

$$\mathbf{B} = \mu_0 \mathbf{H} + \mathbf{M}, \tag{4.1}$$

where $\mathbf{H}$ is an applied magnetic field, μ_0 is the vacuum permeability and $\mathbf{M}$ is the magnetisation. The Maxwell-Ampere law describes the electromagnetic fields produced by a current source [136]:

$$\nabla \times \mathbf{H} = \mathbf{J} + \epsilon_0 \epsilon_r \frac{\partial \mathbf{E}}{\partial t}, \tag{4.2}$$

where $\mathbf{J}$ is the current density, ϵ_0 is the vacuum permittivity, ϵ_r is the material's relative permittivity, $\mathbf{E}$ is an electric field and t is time. The Maxwell-Faraday law of induction describes the generation of an electric field by a time-varying magnetic field [136]:

$$\nabla \times \mathbf{E} = -\frac{\partial \mathbf{B}}{\partial t}. \tag{4.3}$$

Gauss' law for magnetism states that magnetic field lines form closed loops [136]:

$$\nabla \cdot \mathbf{B} = 0. \tag{4.4}$$

Ohm's law states that the current density is proportional to the electric field [136]:

$$\mathbf{J} = \eta \mathbf{E}, \tag{4.5}$$

where η is the electrical conductivity of the sample.

These equations are general, provide a complete description of electrodynamic processes and are the fundamental governing equations that describe EMAT operation. Solution of these equations for specific cases relating to an EMAT transduction problem allows for quantification of the induced body forces, provided the transduction mechanisms are well-understood, and hence for subsequent calculation of the acoustic fields. What follows now is a physical explanation of the three known EMAT transduction mechanisms; the Lorentz force, the magnetisation force and the magnetostrictive effect.

4.2 The Lorentz Force Mechanism

The Lorentz force is the transduction mechanism most-commonly exploited by EMAT designs [106], since it is often the dominant transduction mechanism [137], and because it occurs in all electrically-conducting media and does not rely on any magnetic properties inherent to the sample itself. The interaction relies on the force induced on electrically-charged particles in motion in the presence of a magnetic field.

Consider an arbitrary-geometry EMAT coil above an infinite conducting half space as shown in figure 4.1. Time-varying currents in the EMAT coil will induce a current density profile, $\mathbf{J}$, in the sample, and there exists a magnetic field in the material, $\mathbf{B}$, which is related to the applied magnetic field, $\mathbf{H}$, through the definition given in equation 4.1. Under the quasi-static approximation (see section 5.1 for a justification of this approximation in relation to EMAT operation), the displacement current in equation 4.2 can be ignored and the eddy current distribution induced by a pulsed EMAT coil can be found by solving:

$$\mathbf{J} = \nabla \times \mathbf{H}. \tag{4.6}$$

To then determine the mechanical stress imparted onto the sample, the interactions of the conduction band electrons with the sample lattice must be considered. An assumption is made that the sample is a metallic conductor at ambient temperatures, hence the classical description of electron transport provided by the Drude model is valid [138]:

$$m_e \dot{\mathbf{v}}_e = -e\left(\mathbf{E} + \mathbf{v}_e \times \mathbf{B}\right) - \frac{m_e \mathbf{v}_e}{\tau}, \tag{4.7}$$

where m_e is the electron mass, $\mathbf{v}_e$ is the mean electron velocity, e is the electron's charge, and τ is the mean electron scattering time, with $\tau \backsimeq 10^{-14}$ s for common metals at room temperature [106]. Further assuming that if the electric field, and hence the mean electron velocity, oscillates with frequency ω and that the period of that oscillation is much greater than the mean electron scattering time, $1/\omega \gg \tau$, the system therefore exists in an equilibrium state, where $\dot{\mathbf{v}}_e = 0$:

$$n_e \frac{m_e \mathbf{v}_e}{\tau} = -n_e e \left(\mathbf{E} + \mathbf{v}_e \times \mathbf{B}\right), \tag{4.8}$$

where n_e is the charge carrier (electron) density. The left hand term in equation 4.8 is equal to the change in total momentum of the conduction electrons per unit volume in the scattering time τ. This is equal to the momentum transferred to the ionic lattice of the conductor in the same time, hence the total force on the ionic lattice is given by the sum of Lorentz forces due to the motion of ions in electromagnetic fields and the forces due to conduction electron collisions:

$$\mathbf{f} = N Z_e \left(\mathbf{E} + \dot{\mathbf{u}} \times \mathbf{B}\right) - n_e e \left(\mathbf{E} + \mathbf{v}_e \times \mathbf{B}\right), \tag{4.9}$$

where N is the ion density and Z is the ionic charge. Noting that to maintain charge neutrality, $N Z_e = n_e e$ must be true, that the term $-n_e e \mathbf{v}_e = \mathbf{J}$ and assuming that $\dot{\mathbf{u}} \ll \mathbf{v}_e$ due to the significantly larger mass of the lattice ions compared to an electron, an expression is obtained for the Lorentz force acting on the conductor in terms of the electric current density:

$$\mathbf{F}_{Lorentz} = \int_V \mathbf{J} \times \mathbf{B} \; dV. \tag{4.10}$$

Using equation 4.6 to make the substitution for $\mathbf{J}$, the Lorentz force density can be expressed in terms of the applied magnetic field $\mathbf{H}$ and the total magnetic field $\mathbf{B}$ [106]:

$$\mathbf{F}_{Lorentz} = \int_V (\nabla \times \mathbf{H}) \times \mathbf{B} \; dV. \tag{4.11}$$

Equation 4.11 demonstrates that the Lorentz force is a vector cross product between the eddy current distribution and the total magnetic field, indicating that the generated mechanical forces will be orthogonal to both. The skin effect is a phenomenon whereby the amplitude of an electromagnetic wave incident on a conducting material decreases exponentially with depth into the material. The characteristic length scale of this decay is called the skin depth. Due to the skin effect, the induced eddy current distribution will always lie effectively in a plane parallel to the surface of a

sample. Careful selection of appropriate applied field geometries is therefore required to produce mechanical forces with a desired orientation; applied fields parallel to the surface (but still requiring components normal to the eddy current distribution) will induce stress fields that are directed out of the surface plane, while applied fields that are directed normal to the surface will induce stress fields that lie parallel to the surface's plane. Appropriate choice of applied field and eddy current geometries allows for selection of generated bulk and guided wave modes [106].

4.3 The Magnetisation Force

In ferromagnetic materials, interaction between an externally-applied magnetic field and the internal fields resulting from the magnetic ordering in the material can give rise to mechanical forces through the magnetisation force. The magnetisation, $\mathbf{M}$, of a material is defined as the volume density of the net magnetic moment in the material. The total moment from a volume of ferromagnetic material composed of individual dipole sources is therefore [139]:

$$\mathbf{m}_{tot} = \int_V \mathbf{M} \; dV. \tag{4.12}$$

For any individual magnetic moment, $\mathbf{m}$, in an externally-applied magnetic field, there exists a potential equal to [139]:

$$U = -\mathbf{m} \cdot \mathbf{H}. \tag{4.13}$$

The force on the dipole is hence given by the potential gradient. The volume magnetisation force is therefore:

$$\begin{aligned} \mathbf{F}_{mag} &= \int_V \nabla \left(\mathbf{M} \cdot \mathbf{H} \right) \; dV \\ &= \int_V \left(\mathbf{M} \cdot \nabla \right) \mathbf{H} + \left(\mathbf{H} \cdot \nabla \right) \mathbf{M} + \mathbf{M} \times \left(\nabla \times \mathbf{H} \right) + \mathbf{H} \times \left(\nabla \times \mathbf{M} \right) \; dV. \end{aligned} \tag{4.14}$$

The time-varying component of $\mathbf{H}$ which leads to ultrasound generation is confined to within a few electromagnetic skin depths of the surface. Over this short length scale, the magnetisation is assumed to be constant and hence its derivatives vanish. Therefore, the total force exerted is [106]:

$$\mathbf{F}_{mag} = \int_V \left(\mathbf{M} \cdot \nabla \right) \mathbf{H} + \mathbf{M} \times \left(\nabla \times \mathbf{H} \right) \; dV. \tag{4.15}$$

The integrand in equation 4.15 is the body force density due to the magnetisation force. In an electrically-conducting magnetic material, both the magnetisation and the Lorentz forces contribute to electrodynamic stresses. To quantitatively describe the effect of these forces in combination, it is helpful to evaluate the components of the magnetisation body force density:

$$\begin{aligned}\mathbf{f}_{mag} = &\left(M_x\frac{\partial H_x}{\partial x} + M_y\frac{\partial H_y}{\partial x} + M_z\frac{\partial H_z}{\partial x}\right)\hat{\mathbf{i}} \\ &+ \left(M_x\frac{\partial H_x}{\partial y} + M_y\frac{\partial H_y}{\partial y} + M_z\frac{\partial H_z}{\partial y}\right)\hat{\mathbf{j}} \\ &+ \left(M_x\frac{\partial H_x}{\partial z} + M_y\frac{\partial H_y}{\partial z} + M_z\frac{\partial H_z}{\partial z}\right)\hat{\mathbf{k}},\end{aligned} \tag{4.16}$$

where $\hat{\mathbf{i}}$, $\hat{\mathbf{j}}$ and $\hat{\mathbf{k}}$ are unit vectors in the x, y and z directions respectively. Likewise, evaluation of the body Lorentz force density described by equation 4.11 yields:

$$\begin{aligned}\mathbf{f}_{Lorentz} = &\left(B_y\left(\frac{\partial H_x}{\partial y} - \frac{\partial H_y}{\partial x}\right) + B_z\left(\frac{\partial H_x}{\partial z} - \frac{\partial H_z}{\partial x}\right)\right)\hat{\mathbf{i}} \\ &+ \left(B_x\left(\frac{\partial H_y}{\partial x} - \frac{\partial H_x}{\partial y}\right) + B_z\left(\frac{\partial H_y}{\partial z} - \frac{\partial H_z}{\partial y}\right)\right)\hat{\mathbf{j}} \\ &+ \left(B_x\left(\frac{\partial H_x}{\partial z} - \frac{\partial H_z}{\partial x}\right) + B_y\left(\frac{\partial H_z}{\partial y} - \frac{\partial H_y}{\partial z}\right)\right)\hat{\mathbf{k}}.\end{aligned} \tag{4.17}$$

For a dynamic magnetic field in a conducting medium, the lines of magnetic flux are mostly confined within a few skin depths of the material's surface. Since the skin depth is much smaller than the horizontal extent of the magnetic fields for most EMAT coils, and due to the condition that field lines must form closed loops, it can be assumed that horizontal applied field components are much larger than vertical components; $H_x, H_y \gg H_z$. In this limit, terms containing $\partial H_z \to 0$, and the sum of the Lorentz and magnetisation body forces reduces to:

$$\begin{aligned}\mathbf{f}_{Lorentz} + \mathbf{f}_{mag} = &\\ &\left(\frac{\partial H_x}{\partial x}M_x + \frac{\partial H_y}{\partial x}(M_y - B_y) + B_z\frac{\partial H_x}{\partial z} + B_y\frac{\partial H_x}{\partial y}\right)\hat{\mathbf{i}} \\ &+ \left(\frac{\partial H_x}{\partial y}(M_x - B_x) + \frac{\partial H_y}{\partial y}M_y + B_z\frac{\partial H_y}{\partial y} + B_x\frac{\partial H_y}{\partial x}\right)\hat{\mathbf{j}} \\ &+ \left(\frac{\partial H_x}{\partial z}(M_x - B_x) + \frac{\partial H_y}{\partial z}(M_y - B_y)\right)\hat{\mathbf{k}}\end{aligned} \tag{4.18}$$

It is important to note here that the mixed terms in $\mathbf{M}$ and $\mathbf{B}$ are subtracted from each other, and hence their magnitudes are reduced. Under the approximation that

the bias field is parallel to the sample's surface (i.e. the only non-negligible components of B are B_x and B_y), there still exist in-plane components (in $\hat{\mathbf{i}}$ and $\hat{\mathbf{j}}$) that are not mixed terms, however the vertical ($\hat{\mathbf{k}}$) component contains only mixed terms. Hence, in the case where the bias field is parallel to the sample's surface, the Lorentz and magnetisation body forces largely cancel and the induced out-of-plane stress field is reduced in magnitude. The efficiency of EMAT generation of longitudinal ultrasound modes in electrically-conducting ferromagnetic materials is therefore lower than for non-magnetic materials. If the applied field is predominantly normal to the sample's surface, the non-mixed terms of the in-plane force components still survive, and hence shear wave generation is significantly less affected [106].

4.4 The Magnetostriction Mechanism

Magnetostriction is a phenomenon analogous to the piezoelectric effect (see section 3.6.1), in which an applied magnetic field can cause dimensional changes in a sample. The magneto-crystalline anisotropy of a material means that there are preferential (low energy) magnetisation axes related to the principal axes of the unit cell, which themselves are associated with different lattice parameter values. In the absence of an applied field, magnetic domains of uniform polarisation form in a ferromagnetic material in order to reduce the total magnetostatic energy of the sample. Subsequent application of an external magnetic field can induce a net torque on dipole moments in the material, leading to a propagating reorientation of individual lattice sites, which corresponds to shifting of the magnetic domain walls, and rotation of individual domains, to reduce magnetostatic energy. This induces a strain in the material if the lattice parameters differ between the relevant crystallographic directions, hence leading to a dimensional change in the sample in the presence of an applied field [140]. Application of time-varying magnetic fields therefore induces time-dependent strains in the material, leading to acoustic wave propagation [106].

The quantitative description of the magnetostrictive effect is complex and highly non-linear [141], but typically when modelling EMATs, the biasing magnetic field is much larger than the dynamic field. In this limit, the modulation of the dynamic field can be modeled as a small perturbation of the bias field, and the magnetostrictive effect can be assumed to be locally linear about the chosen bias field value [142, 137]. The strain induced in a magnetic material can then be expressed as [142]:

$$\epsilon = S^H \sigma + D\mathbf{H}, \tag{4.19}$$

where ϵ is the strain tensor, S^H is the elastic compliance matrix for a constant value of applied magnetic field, $\mathbf{H}$, σ is the stress tensor and D is the magnetostriction

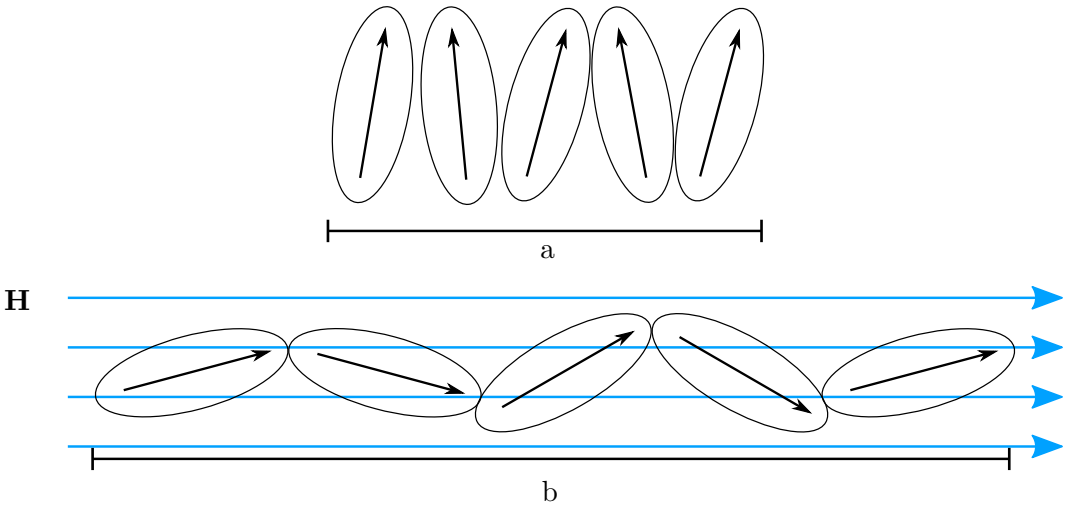

Figure 4.2: Schematic representation of the magnetostriction mechanism. Realignment of magnetic domains under the influence of an applied magnetic field induces strain in the lattice, leading to acoustic wave propagation.

matrix. If a magnetic field is applied in the absence of an external stress, the strain field produced is $\epsilon = D\mathbf{H}$. This strain can be used to evaluate an equivalent applied stress field, and hence the magnetostriction stress can be written [142]:

$$\begin{aligned} \sigma &= c_k \epsilon, \\ &= c_k D\mathbf{H}. \end{aligned} \tag{4.20}$$

Hence the body forces due to magnetostrictive effects can be evaluated if the coefficients of the magnetostriction tensor are known. In practice, because the magentostrictive effect is highly non-linear and varies with the direction, magnitude and oscillation frequency of the applied field, these coefficients are found empirically from measurements of the magnetostriction curve for a given material.

The magnetostrictive effect depends on the presence of magnetic domain structures in the material, and so is only observed in ferromagnetic materials. Although almost all ferromagnetic materials exhibit magnetostriction, recent finite element method numerical studies conducted by Ribichini *et al.* [137] suggest that this transduction mechanism is only dominant in highly magnetostrictive materials such as ferrite oxides, and that the Lorentz force is the dominant transduction mechanism in most samples, including ferritic steels. In samples with very high magnetostriction coefficients, this transduction mechanism can lead to very high signal-to-noise ratios that are comparable to those obtained with conventional piezoelectric probes. One such example is found in boiler tubes, which develop thick

oxide coatings over time and make conventional inspections difficult, but which are highly magnetostrictive, allowing for reliable inspection with EMATs optimised for magnetostriction transduction [143].

4.5 Ultrasonic Reception with EMATs

This chapter has so far detailed the generation of acoustic waves using EMATs operating using the principles of the Lorentz, magnetisation and magnetostriction mechanisms, but EMATs are also suitable for use in the detection of ultrasonic waves in conducting and magnetic materials.

4.5.1 The Reverse Lorentz Mechanism

The Lorentz mechanism is specific to electrically-conducting materials, and hence the receiving mechanism is discussed here in terms of metallic samples. A plane wave incident on the surface of a material leads to a surface particle displacement $\mathbf{u}(\mathbf{r}, t)$. The ions of a metal are fixed in the metallic lattice and so must move with the acoustic wave, and the conduction band electrons move with the lattice ions to maintain charge neutrality. If this motion occurs in the presence of a biasing magnetic field, the electrons experience a Lorentz force [136]:

$$\mathbf{F}_{Lorentz} = e\left(\dot{\mathbf{u}} \times \mathbf{B}\right) \tag{4.21}$$

In accordance with Faraday's law of induction, and because the force on a charged particle is equivalent to the electric field $\mathbf{E}$ multiplied by the particle's charge, this is equivalent to an electric field, and hence the induced current density can be expressed using Ohm's law (equation 4.5):

$$\mathbf{E} = \dot{\mathbf{u}} \times \mathbf{B} \tag{4.22}$$

$$\mathbf{J} = \eta\left(\dot{\mathbf{u}} \times \mathbf{B}\right) \tag{4.23}$$

The eddy currents induced by the time-varying surface displacement caused by an incident acoustic wave in turn generate a dynamic magnetic field in accordance with equation 4.2. Currents are induced in the EMAT detection coil by the dynamic field, and hence the EMAT is able to detect ultrasonic signals. It is important to note that the motion of the conductor due to an acoustic wave only generates eddy currents in the presence of a magnetic field, hence a bias field must be present if the EMAT is to function as a detector.

The bias field orientation must be considered carefully, depending on the type of particle motion the EMAT sensor is designed to detect. Equation 4.23

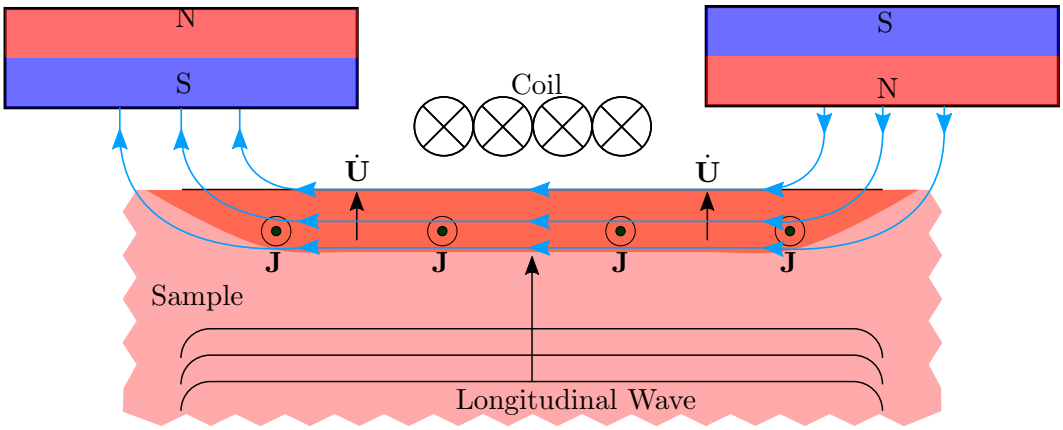

Figure 4.3: Schematic diagram of an EMAT coil and magnet configuration operating via the Lorentz mechanism that is sensitive to out-of-plane displacements.

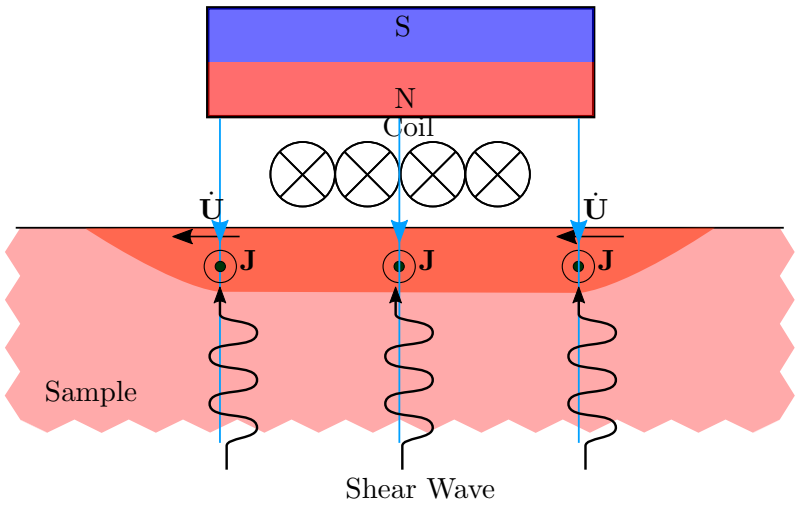

Figure 4.4: Schematic diagram of an EMAT coil and magnet configuration that is sensitive to in-plane displacements.

shows that the induced eddy currents, and hence the currents in the detection coil, are proportional to the vector cross product of the surface particle velocity and bias field, indicating that the detection coil direction, bias field and particle velocity vector must all be mutually orthogonal to maximise sensitivity. Since the detection coil must generally lie parallel to the sample's surface, the applied bias field must lie either perpendicular to the sample's surface to detect in-plane particle motion, or parallel to the surface to detect out-of-plane particle motion (see figures 4.3 and 4.4).

4.5.2 The Reverse Magnetostriction Mechanism

In ferromagnetic materials, the deformation due to an acoustic wave leads to perturbation of the magnetic domain structure of the material. This causes a local change in the magnetisation of the sample and hence in the magnetic flux density above the sample. The time-varying flux density induces currents in the EMAT detection coil, hence allowing the detection of ultrasonic signals via the reverse magnetostriction mechanism, or Vilari effect. In this case, the magnetic field produced by a magnetostrictive material due to an applied stress is given as [137]:

$$B = D^T \sigma \mu^\sigma \mathbf{H} \tag{4.24}$$

where D^T is the transposed magnetostriction matrix, σ is the stress tensor, μ^σ is the magnetic permeability tensor for the material under constant stress and $\mathbf{H}$ is an externally-applied field. As with the magnetostriction generation mechanism, evaluation of this effect requires knowledge of the magnetostriction tensor coefficients, which can only be found empirically from measurements of magnetostrictive curves. In general, Lorentz force detection is the dominant measurement mechanism, excepting special cases where the material has high magnetostrictive coefficient values, such as for magnetite [137].

Chapter 5

High Power EMAT Operation

As discussed in section 1.2.3, as-cast steel slabs are thick and contain coarse, inhomogeneous grain structures, and so are expected to highly attenuate ultrasonic signals. Sufficient ultrasound penetration for measurements with a practicable signal-to-noise ratio in these thick samples requires the use of lower frequency signals (at the expense of lower spatial resolution), or high-power EMAT generators, such as those described in section 5.3. Due to the required high currents, and associated large dynamic field values, the transduction mechanism is predominantly the Lorentz force due to the dynamic magnetic field (hereinafter referred to as the "self-field"). This chapter introduces the concept of the self-field EMAT in detail, and provides a theoretical framework for quantifying the pressure profiles generated by these devices, so that the generated acoustic wavefields can be evaluated and compared for arbitrary choices of generation coil configuration. This analysis forms the basis of the finite element modelling used for the EMAT array optimisation presented in chapter 6.

5.1 Lorentz Force EMATs as Magnetic Pressure Sources

In order to quantitatively model the effect of different choices of generation coil geometry on the acoustic wavefield radiated by self-field Lorentz mechanism EMATs, the electromagnetic fields within the sample material must first be calculated, so that the Lorentz force can be evaluated (see equation 4.11). Consider an infinite linear induction coil above a two-dimensional conducting half space as shown in figure 5.1. The following arguments can be made according to the symmetry of the problem:

- The currents, both those in the coil, and those induced by the coil, are purely in the y direction, so the only non-zero component of $\mathbf{E}$ is E_y.
- The coil's extent is infinite in the x direction, so the only non-zero component

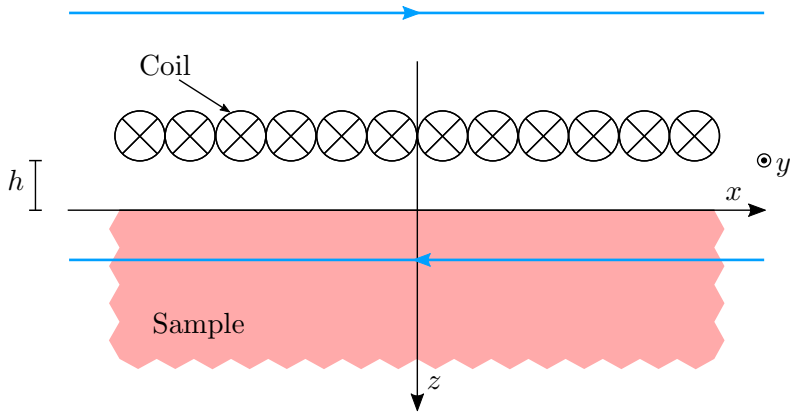

Figure 5.1: Schematic diagram of the self-field coil model, showing an infinite, unidirectional induction coil above an infinite conducting half-plane.

of $\mathbf{H}$ is H_x.

- the model is infinite and symmetric in both the x and y directions, so derivatives with respect to x or y are zero.

The following analysis can be simplified if the displacement current in equation 4.2 is ignored (i.e. the magnetostatic approximation is made). The condition that must be satisfied for this approximation is that the displacement current is much smaller than the induced current density:

$$\epsilon_0 \frac{\partial \mathbf{E}}{\partial t} \ll \mathbf{J}, \tag{5.1}$$

$$\epsilon_0 \frac{\partial \mathbf{E}}{\partial t} \ll \sigma \mathbf{E}. \tag{5.2}$$

An order of magnitude evaluation of this inequality can be made by replacing the time derivative of $\mathbf{E}$ with a ratio of quantities on the correct scale for the problem. If a harmonic approximation for time dependence is made, the value of the derivative can be approximated by taking the maximum amplitude of the electric field and dividing by the period of one oscillation.

$$\frac{\partial \mathbf{E}}{\partial t} = \frac{\Delta \mathbf{E}}{\Delta t} \approx \frac{\mathbf{E}}{\Delta t}. \tag{5.3}$$

The appropriate timescale, Δt, for the variation of the electric field is given by the period of a harmonic oscillation with frequency f. The appropriate condition for

the justification of the magnetostatic approximation therefore reduces to:

$$\frac{\epsilon_0 f}{\sigma} \ll 1. \tag{5.4}$$

The typical operating frequencies for an EMAT range from 0.01 to 10 MHz [106], the permittivity of free space is approximately 8.85×10^{-12} Fm^{-1} [136] and the conductivity of most metals falls in the range of 10^6 - 10^8 Sm^{-1} [144]. Inserting these values into the left hand side of the magnetostatic inequality yields a number of order 10^{-12}, hence the inequality in equation 5.4 is satisfied and the magnetostatic approximation is justified.

Applying the symmetry arguments and imposing the magnetostatic condition, the Maxwell-Faraday and Maxwell-Ampere equations (equations 4.2 and 4.3) can be written as:

$$\frac{\partial E_y}{\partial z} = -\frac{\partial B_x}{\partial t}, \tag{5.5}$$

and

$$\begin{aligned} \frac{\partial B_x}{\partial z} &= \mu J_y, \\ &= \mu\sigma E_y, \end{aligned} \tag{5.6}$$

where Ohm's law (equation 4.5) has been used to substitute for J_y. The coupled partial differential equations 5.5 and 5.6 can be solved by first taking the z derivative of equation 5.6 and the substituting in the expression from equation 5.5:

$$\frac{\partial^2 B_x}{\partial z^2} = \mu\sigma \frac{\partial B_x}{\partial t}. \tag{5.7}$$

Now the assumption is made that the driving current, and therefore its associated magnetic field, have a harmonic time dependence, i.e. that $B_x(t) = B_x \sin(\omega t)$, and that this can be represented in complex exponential notation as $B_x(t) = B_x e^{i\omega t}$. Equation 5.7 can therefore be written as:

$$\frac{\partial^2 B_x(t)}{\partial z^2} = i\omega\mu\sigma B_x(t). \tag{5.8}$$

Inserting a trial solution of the form $B_x(t) = B_x^0(t)e^{\lambda z}$, where $B_x^0(t)$ and λ are arbitrary constants, and enforcing the boundary condition that $\lim_{z\to\infty} B_x(t) = 0$ leads to the following solution for $B_x(t)$:

$$B_x(t) = B_x^0(t) \exp\left(-\frac{z}{\delta}\right) \exp\left(-\frac{iz}{\delta}\right), \tag{5.9}$$

where $B_x^0(t)$ is the x component of the magnetic field at the surface of the conducting half space and δ is the electromagnetic skin depth, here defined as:

$$\delta = \sqrt{\frac{2}{\omega\mu\sigma}}. \tag{5.10}$$

Equation 5.9 describes the variation of the electromagnetic field with depth into the conducting half-space. In order to calculate the inductive Lorentz force, it is also necessary to determine the variation of the electric field with depth. To do this, the z derivative of equation 5.5 and the t derivative of equation 5.6 are taken, and the two sides of the equations set equal to obtain:

$$\frac{\partial^2 E_y}{\partial z^2} = i\omega\mu E_y(t), \tag{5.11}$$

where again, a harmonic time dependence of the form $E_y(t) = E_y(t)e^{i\omega t}$ has been assumed. This equation has the same functional form as equation 5.8, and hence the electric field at any depth is given by:

$$E_y(t) = E_y^0(t)\exp\left(-\frac{z}{\delta}\right)\exp\left(-\frac{iz}{\delta}\right), \tag{5.12}$$

where $E_y^0(t)$ is the value of the y component of the electric field at the material boundary. Making use of equation 4.5, the eddy current density distribution is therefore:

$$J_y(t) = J_y^0(t)\exp\left(-\frac{z}{\delta}\right)\exp\left(-\frac{iz}{\delta}\right), \tag{5.13}$$

where J_y^0 is the value of the y component of the current density at the material boundary. In order to correctly evaluate the Lorentz force, the phase lag between J_y and B_x must be accounted for by expressing J_y in terms of B_x. This is done by substituting the obtained forms for J_y and B_x into equation 5.5. Firstly, evaluating the left hand side of equation 5.5:

$$\begin{aligned} -\sigma\frac{\partial B_x(t)}{\partial t} &= \frac{\partial J_y(t)}{\partial z}, \\ &= -\left(\frac{1+i}{\delta}\right)J_y^0\exp\left(-\frac{z}{\delta}\right)\exp\left(-\frac{iz}{\delta}\right)\exp\left(i\omega t\right). \end{aligned} \tag{5.14}$$

The time-derivative of the magnetic field in the left hand side of equation 5.5 is given by:

$$\frac{\partial B_x(t)}{\partial t} = i\omega B_x^0\exp\left(-\frac{z}{\delta}\right)\exp\left(-\frac{iz}{\delta}\right)\exp\left(i\omega t\right), \tag{5.15}$$

and hence, substituting equation 5.15 into the left hand side of equation 5.14 yields:

$$\begin{aligned} J_y^0 \exp(i\omega t) &= \left(\frac{i}{1+i}\right) \omega\delta\sigma B_x^0 \exp(i\omega t), \\ &= \omega\delta\sigma B_x^0 e^{i\omega t} e^{i\pi/4}. \end{aligned} \tag{5.16}$$

It is now possible to obtain an expression for the Lorentz force, $\mathbf{F}_{Lorentz} = \mathbf{J} \times \mathbf{B}$, in terms of the applied magnetic field only. This is simply a multiplication of the expressions for J_y and B_x given in equations 5.16 and 5.9, since they are already the appropriate components for evaluating the cross product, leaving a Lorentz force component in the z direction:

$$F_{Lorentz} = \omega\delta\sigma \left(B_x^0\right)^2 \exp\left(-\frac{2z}{\delta}(1+i)\right) e^{2i\omega t} e^{i\pi/4}. \tag{5.17}$$

This equation gives the expression for the time-dependent Lorentz force as a function of depth. Note that the exponential terms in equation 5.17 show that the Lorentz force is proportional to the multiplication of two cosine terms with the same frequency, one of which has a phase lag of $\pi/4$ with respect to the other, which would suggest that the Lorentz force is not exclusively repulsive. At any given depth in the material, this statement is true and there is an attractive component of the Lorentz force, however empirical studies of self-field Lorentz force EMAT generation suggest that the induced force is exclusively repulsive [106]. This can be reconciled with the result in equation 5.17 by considering that the length scale over which these variations occur, $\delta/2$, is much smaller than the acoustic wavelength, and the force can therefore be considered as a surface pressure, not a body force as described here. It is therefore necessary to integrate equation 5.17 over all depth to determine an equivalent surface pressure:

$$\begin{aligned} F_{Lorentz}^{total} &= \int_0^\infty \omega\delta\sigma \left(B_x^0\right)^2 \exp\left(-\frac{2z}{\delta}(1+i)\right) e^{2i\omega t} e^{i\pi/4}\, dz, \\ &= \left[-\frac{\delta}{2(1+i)} \omega\delta\sigma \left(B_x^0\right)^2 \exp\left(-\frac{2z}{\delta}(1+i)\right) e^{2i\omega t} e^{i\pi/4}\right]_0^\infty, \\ &= 0 + \frac{\delta}{2(1+i)} \omega\delta\sigma \left(B_x^0\right)^2 e^{2i\omega t} e^{i\pi/4}. \end{aligned} \tag{5.18}$$

The factor $1/(1+i)$ is equivalent to a phase shift of $e^{-i\pi/4}$, so integrating over all

depth removes the phase term and leads to a purely repulsive force:

$$\begin{aligned} F_{Lorentz}^{total} &= \frac{\omega\sigma\delta^2\left(B_x^0\right)^2}{4}e^{2i\omega t}, \\ &= \frac{\left(B_x^0\right)^2}{2\mu}e^{2i\omega t}, \\ &= \frac{\left(B_0(t)\right)^2}{2\mu}. \end{aligned} \tag{5.19}$$

This quantity is known as the magnetic pressure; it is a well-known result in electrodynamics and is familiar as a term in the Maxwell stress tensor [136]. This result indicates that the magnitude of the self-field Lorentz pressure is proportional to the square of the surface magnetic flux density, and hence that there is a rapid increase in induced stress with increasing excitation current magnitudes. This property also suggests that if the dynamic field has harmonic time dependence with an angular frequency of ω, the Lorentz force will have a harmonic time dependence with an angular frequency of 2ω. The direction and sign of the Lorentz pressure expression in equation 5.19 demonstrates that the self-field Lorentz force is exclusively repulsive, since at the start of this derivation, the positive z direction was defined in figure 5.1 as being into the material's depth. These results are in agreement with previously-acknowledged properties of the self-field Lorentz force, however these properties have not been explicitly derived in the literature [106, 145].

This derivation relates exclusively to harmonic driving currents, however the analysis can be generalised if the assumption is made that an arbitrary pulsed driving field can be represented as a Fourier series. If this is true, the field is just the sum of many individual sinusoidal components. Since electromagnetic fields add linearly, the analysis valid for a single frequency component is also valid for other frequency components and for sums of different frequency components. Hence, for a self-field Lorentz force induced by an arbitrary pulsed excitation, the magnitude scales with the square of magnetic field.

The other main assumption made in this derivation is that the applied magnetic field only has components parallel to the x direction and that derivatives taken in the x direction are zero, due to the infinite extent of the coil. The model for calculation of the field geometry due to a wire above a conducting plane detailed in section 5.2 shows that the magnetic field is not in fact exclusively directed in the x direction at the material's surface; the vertical field components are however shown to be much smaller than the horizontal components, and hence this approximation is justified.

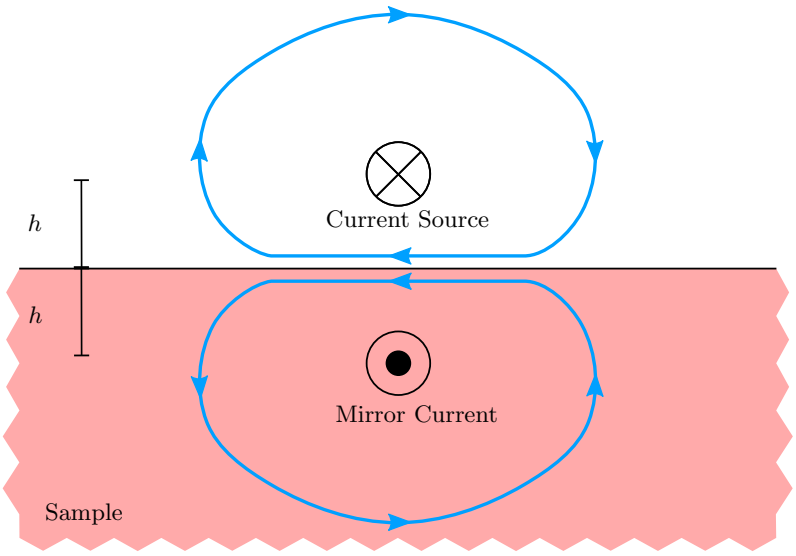

Figure 5.2: Schematic diagram of the method of images. In high frequency limits, field penetration into the material can be considered negligible, and the field outside the material can be calculated from the summation of the source field with that of a mirror current reflected in the plane of the material boundary.

For non-magnetic materials where $\mu \approx \mu_0$, the result in equation 5.19 appears initially to be invariant of material properties, however, as shown in section 5.2, the magnitude of the surface magnetic flux density, B_x^0, is a function of the material's electromagnetic skin depth, and hence the Lorentz pressure magnitude varies with the magnetic permeability and electrical conductivity of the target material. The effect of the properties of the target material on the magnetic flux density at the surface of the half space is discussed in further detail in the following section, which concerns evaluating the Lorentz force distribution from a single wire above a conducting medium.

5.2 Semi-analytic Coil Modelling

5.2.1 Calculation of Lorentz Pressure due to a Single Wire Source

The derived result in equation 5.19 shows that the equivalent surface pressure resulting from the Lorentz generation mechanism of a self-field pulsed EMAT coil is equivalent to the magnetic pressure due to the surface magnetic field. This allows for easy evaluation of the Lorentz force magnitude from an arbitrary EMAT coil configuration provided the magnetic field at the sample's surface can be calculated. Outlined here is a method for modeling the magnetic field from an infinite line current source, since distributions of line current sources can be used to represent

arbitrary finite one-dimensional coils.

In free space, the magnetic field around an infinite line of current is given by Ampere's law, which in integral form is expressed as [136]:

$$\oint \mathbf{B} \cdot \mathbf{dl} = \mu_0 \mathbf{I}, \tag{5.20}$$

where, **dl** is a line element of a closed loop surrounding a current source and I is the current enclosed within the loop. The magnetic field around a point-like wire is hence given by:

$$\mathbf{B}_\phi = \frac{\mu_0 I}{2\pi r}\hat{\phi}, \tag{5.21}$$

where $\mathbf{B}_\phi$ is the magnetic field vector, r is the radial distance from the wire and $\hat{\phi}$ is the azimuthal unit vector. This equation describes a free wire, however, as shown by equation 5.9, the magnetic field amplitude decays rapidly with depth in a conducting medium. Gauss' law for magnetism (equation 4.4) stipulates that magnetic field lines must form closed loops, and hence the magnetic field above a conducting plane will be distorted; it is therefore necessary to account for the effects of the conducting medium when determining the surface magnetic field profile for evaluation of the Lorentz force. In the high-frequency limit, the electromagnetic skin depth is sufficiently small that penetration of the magnetic field into the sample can be considered negligible, and the divergenceless condition on the magnetic field from Gauss' law then requires that the surface magnetic field is directed exclusively in the horizontal direction, with vertical components vanishing. This condition on the boundary magnetic flux density can be achieved through the use of an oppositely-directed image current reflected in the plane of the conducting surface, (see figure 5.2), and due to the uniqueness theorem for Poisson's equation, the sum of the field from the current source and image charge therefore gives an exact solution for the magnetic field above the conducting half space. This methodology was employed by Rueter when modeling the self-field Lorentz force induced by annular current sources in the high liftoff limit [110]. This model, however, assumes there is no penetration of the magnetic field into the target medium and hence incorrectly leads to the statement that the self-field Lorentz pressure is material invariant. In practice, many problems of interest (such as self-field Lorentz force EMAT generation) do not consider media of infinite conductivity; a direct application of the method of images is insufficient for these cases, and the effect of field penetration into the material must be accounted for.

An exact solution describing the magnetic flux density above an infinite half-space of finite conductivity can be obtained using complex image theory, which was

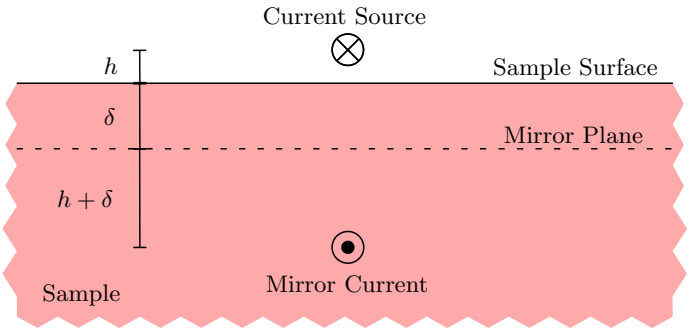

Figure 5.3: For a current distribution above an infinite half space with finite conductivity, the magnetic field above the medium can be described by the superposition of the field due to the free current source with a mirror field reflected about a plane at depth δ below the material's surface, where δ is the complex skin depth.

developed originally for the study of geophysical electrodynamic fields above the Earth [146, 147]. In low frequency limits where electromagnetic field penetration into a material is sufficient, complex image theory states that the finite conducting half space can be replaced by an infinitely conducting half space at some complex-valued depth, $h + 2\delta/(1+i)$ beneath the physical surface of the medium, where h is the vertical separation between the boundary of the half space and the current source (see figure 5.3). This modified version of the method of images fully accounts for the effects of material properties as parameterised by the electromagnetic skin depth, and for the effects of field interference from an induced volume current distribution (as opposed to a mirror current, which models a field that does not penetrate the material), which leads to a phase dependence on the observed electrodynamic fields and hence requires complex representation.

For the case of an infinite line current source above a half-space of finite conductivity, the magnetic field at the interface was derived by Boteler and Pirjola [148], who started with the field due to a free wire given in equation 5.21 and considered the sum of the incident and reflected magnetic field components. The magnetic field components at the interface are given by [148]:

$$B_x = \frac{\mu_0 I}{2\pi}\left(\frac{h}{h^2+x^2} + \frac{h+2p}{(h+2p)^2+x^2}\right), \tag{5.22}$$

and

$$B_z = -\frac{\mu_0 I}{2\pi}\left(\frac{x}{h^2+x^2} - \frac{x}{(h+2p)^2+x^2}\right), \tag{5.23}$$

where $p = \delta/(1+i)$. Evaluation of the surface Lorentz force profile using equation 5.19 is possible using the field components derived by Boteler and Pirjola, however

practical use of this result is complicated because there are two field components, and hence two components to the Lorentz pressure, and each is a complex function of x, indicating that the phase of the Lorentz force changes with distance away from the current source along the material surface.

Evaluation of the Lorentz pressure components demonstrates that the Lorentz pressure due to the vertical field component and spatial phase variation can be justifiably ignored; in the context of this thesis, the material of interest is steel, which has an electrical conductivity of approximately 7×10^6 Sm^{-1} [144], a relative magnetic permeability in a range from approximately 1 - 2000 [149, 150], and the transducer frequency of operation is approximately 1.0 MHz (see section 5.3). Since magnetoelastic generation mechanisms are not considered here, it is appropriate to choose a low relative permeability value consistent with a non-magnetic steel, such as austenitic stainless steel. Higher values would nevertheless further justify the approximations made in this analysis, since they would correspond to a smaller skin depth value and hence closer agreement with the high frequency limit. Choosing values of 7×10^6 Sm^{-1} and 1.0 for the conductivity and relative magnetic permeability respectively therefore gives an electromagnetic skin depth, $\delta = 0.47$ mm, which can then be used to evaluate the surface magnetic flux components using equations 5.22 and 5.23. The liftoff of the current source from the material surface, h, is chosen to be 0.2 mm, since this is a reasonable approximation for the liftoff values used during experimental studies later in this thesis, and the current magnitude is chosen to be 1.75 kA, on the basis of the measurements presented in section 5.3.

The magnitude of the Lorentz force can then be evaluated by computing $|B_i|^2 / 2\mu_0$ for each force component, i; the x and z components of the Lorentz force due to an infinite line source at a vertical separation of 0.2 mm from a material with an electromagnetic skin depth of 0.47 mm are shown in figure 5.4. Although the tangential Lorentz force is clearly non-zero, its magnitude is sufficiently small in comparison to the out-of-plane force component that it can be neglected; in terms of peak amplitude, the out-of-plane force component is approximately 6 times greater than the tangential force component.

The phase variation of the Lorentz force profile as a function of x is difficult to account for, because the excitation currents concerned are typically non-sinusoidal and hence consideration of phase lags for arbitrary pulse excitations becomes non-trivial. The phase variation can be computed by considering that the surface flux density is a complex number with real and imaginary components B_i and B_r respectively:

$$B = B_r + iB_i. \tag{5.24}$$

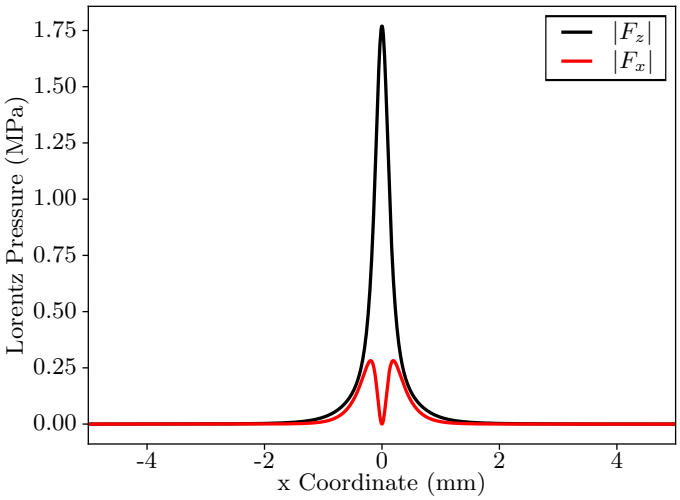

Figure 5.4: The magnitude of the z and x components of the Lorentz pressure (F_z and F_x respectively) due to an infinite wire source located 0.2 mm above a conducting medium with electromagnetic skin depth 0.47 mm.

Since the Lorentz pressure is proportional to the square of the flux density, the complex Lorentz force pressure is proportional to:

$$F_L \propto B_r^2 - B_i^2 + 2iB_rB_i, \tag{5.25}$$

hence the phase of the Lorentz force is given by the arctangent of the ratio of the imaginary and real parts of the force:

$$\phi = \arctan\left(\frac{2iB_rB_i}{B_r^2 - B_i^2}\right). \tag{5.26}$$

A plot of the phase variation, ϕ, as a function of x with the magnitude of the z component of the Lorentz force is shown in figure 5.5. Inspection of the plot demonstrates that the spatial extent of the Lorentz force induced by the wire is highly localised to within a lateral distance of 0.5 mm either side of the wire's position, and that the maximum phase variation within this space never exceeds 10°. Significant phase differences between regions of the Lorentz surface pressure profile do exist when comparing sections of the surface much further outside of the region directly adjacent to the wire, but the corresponding Lorentz pressure magnitude in these regions is small enough that it can be justifiably neglected (the integrated Lorentz force magnitude in these regions is approximately 10 % of the integral of the

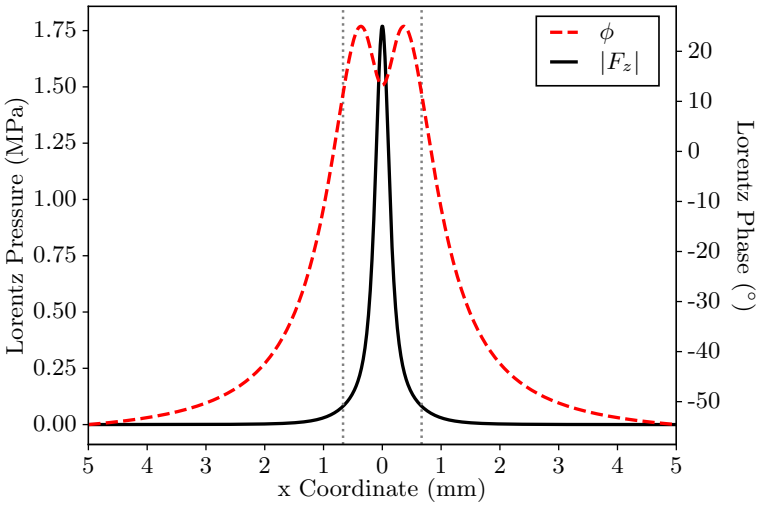

Figure 5.5: The magnitude of the out-of-plane equivalent surface Lorentz pressure (F_z) and the phase (ϕ) of the pressure profile with respect to the driving current as a function of distance along the material surface, x, for a single wire source located 0.2 mm above a half-plane with an electromagnetic skin depth of 0.47 mm. The grey dotted lines are located 0.5 mm from the wire source and show that the majority of the Lorentz pressure is localised within this region.

whole force profile). Due to the highly-localised nature of the Lorentz pressure and the relatively small phase lag differences in the region immediately surrounding the wire, it is reasonable to approximate that the pressures exerted at different points along the material surface vary in phase with each other. The Lorentz pressure due to a single infinite wire source is therefore approximated by the expression:

$$F_{Lorentz} \approx \frac{\mu_0 I^2}{8\pi^2} \left| \frac{h}{h^2 + x^2} - \frac{h + 2p}{(h + 2p)^2 + x^2} \right|^2 \tag{5.27}$$

This analysis of the Lorentz force generation mechanism agrees qualitatively with modeling outlined by Rueter [110], however there are two important exceptions. In the analysis presented by Rueter, the use of the method of images without consideration for the effects of finite conductivity indicated that the Lorentz pressure magnitude is invariant with respect to the target material. Intuitively this is not the case, since the Lorentz generation mechanism only applies to electrically conducting media and hence the material conductivity would be expected to influence the magnitude of the Lorentz pressure for a given excitation current. This effect is fully accounted for in complex image theory through the appearance of δ

in the surface magnetic field expression. A secondary consequence of the choice to apply the high frequency limit (i.e. to assume that there is no magnetic field penetration in the material) is that the model outlined by Rueter over-predicts the Lorentz force magnitude; analysis using the complex image method returns lower Lorentz force magnitudes than reported by Rueter for a given excitation current and target material.

5.2.2 Calculation of the Self-Field Lorentz Force From Finite Width Coils

Equation 5.27 gives a simple functional expression for the Lorentz force due to an infinite line current source on a conducting surface as a function of distance along the surface, x, and as a function of liftoff, h. A plot of the Lorentz force distribution generated by a single infinitesimal current source is shown for a range of liftoff values in figure 5.6. The data generated using equation 5.27 demonstrate that there is a significant reduction in the generated force amplitude with increasing liftoff, as well as a less-significant spreading of the pressure profile beyond the extent of the current source.

Two-dimensional coils with arbitrary geometry can easily be modelled semi-analytically by summing over many such infinitesimal current sources arranged to represent a coil, albeit with the complication that the Lorentz force cannot be directly evaluated by simply summing over wire sources represented by equation 5.27, since the total field from the coil must first be calculated. For example, a linear coil of width 4 mm can be modelled by summation of equation 5.22 over an appropriate number of infinitesimal line sources to determine the surface magnetic flux density due to a finite-width coil. Evaluation of the Lorentz force is then possible by computing the square of the result and dividing by $2\mu_0$. The wire diameter used in the experiments in later chapters is 0.14 mm, and so the approximate turn density of the experimental coils used is 5 mm^{-1}. A 4 mm wide coil can therefore be modelled using the above expression for 20 individual current line sources spaced 0.2 mm apart. The results of this model for liftoff values, h, ranging from 0.1 to 0.5 mm are shown in figure 5.7. For $h = 0.1$ mm, a significant local spatial variation in the pressure magnitude is observed; this occurs because the liftoff is now smaller than the spacing between adjacent constituent current sources in the modelled coil (0.2 mm), and hence the surface pressure between two adjacent sources is much lower than the pressure directly beneath a source.

Likewise, more complex coil geometries containing current elements with opposing polarity can be represented. The racetrack coil designs described in chapter

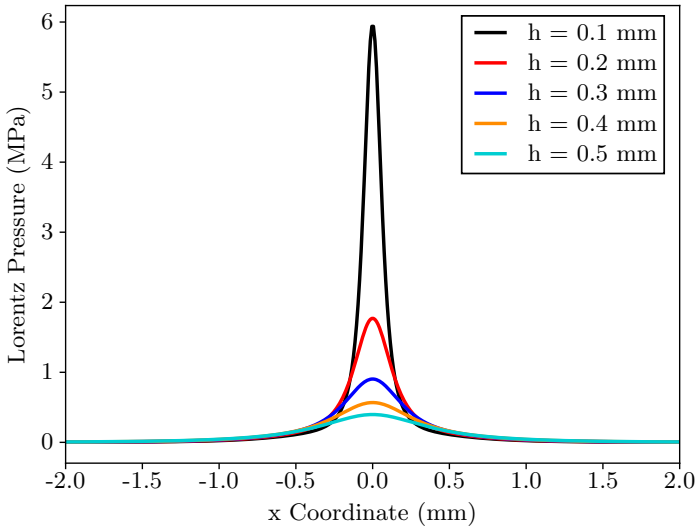

Figure 5.6: The equivalent surface Lorentz pressure from a single wire source for a range of liftoff values, h, as calculated using equation 5.27. The current amplitude used to calculate these pressure profiles is 1.75 kA, following from the measurements presented in section 5.3.

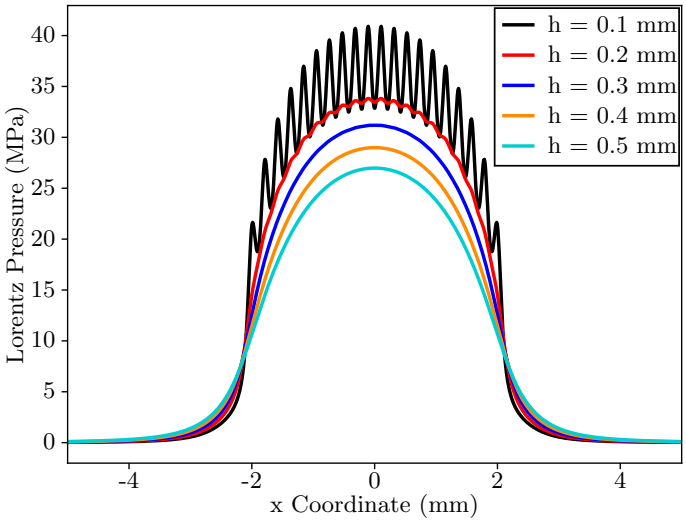

Figure 5.7: The equivalent surface Lorentz pressure from a 4 mm wide coil composed of 20 individual single wire sources (as shown in figure 5.27) spaced uniformly. The current amplitude used to calculate these pressure profiles is 1.75 kA, following from the measurements presented in section 5.3.

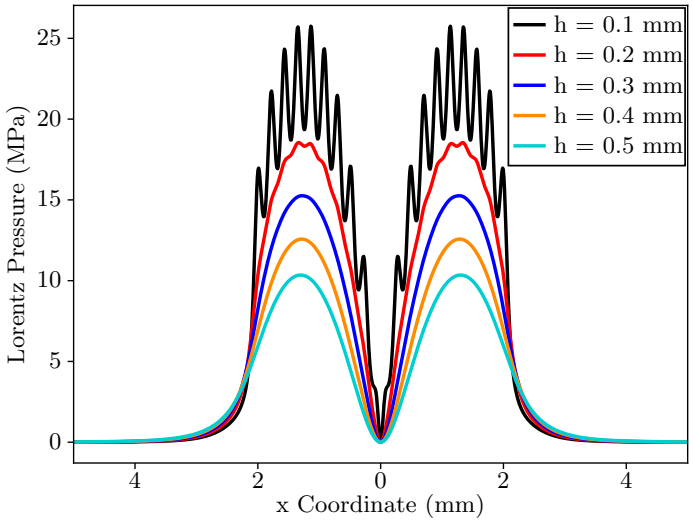

Figure 5.8: The equivalent surface Lorentz pressure from a 4 mm wide racetrack coil composed of 20 individual single wire sources (as shown in figure 5.27). The current amplitude used to calculate these pressure profiles is 1.75 kA, following from the measurements presented in section 5.3.

6 consist of two coil sections with opposite polarity, each of width 2 mm, placed adjacent to each other. The total field produced by this coil can be determined by summing the magnetic field over 10 wire turns spaced 0.2 mm apart between -2.0 and 0.0 mm, and then summing the fields produced by 10 opposing wire turns spaced 0.2 mm apart between 0.0 and 2.0 mm. The equivalent surface pressure profile due to the Lorentz force can then be determined by calculating the square of the resulting profile and dividing by $2\mu_0$. The result of modelling a coil with this geometry for a range of liftoff values between 0.1 and 0.5 mm is shown in figure 5.8.

In each case, regardless of the choice of coil geometry, the Lorentz force is always directed normal to the sample surface, is highly localised beneath the extent of the coil and decreases rapidly with liftoff. As liftoff is increased in any configuration, the spatial extent of the Lorentz pressure profile does increase, but this effect is small enough that it can be ignored. Using these models of Lorentz pressure, it is possible to evaluate the generated acoustic wavefields numerically using the finite element method and optimise the coil configuration for an intended application.

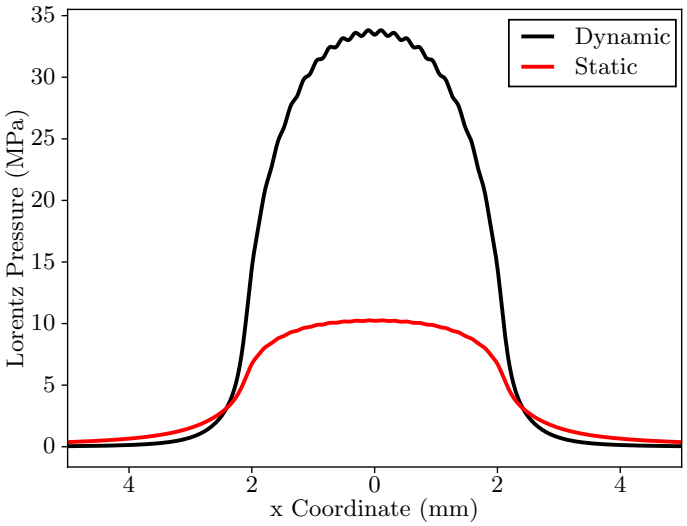

Figure 5.9: A comparison between the static and dynamic Lorentz force profiles for a 4 mm linear EMAT coil at a liftoff of 0.2 mm, with a static horizontal bias field of 1.4 T and an excitation current of 1.75 kA.

5.2.3 Comparison with Static Field EMAT Generation

In the analysis discussed in section 5.2.2, the method of images used to calculate the surface flux density is general, and hence this method can also be easily extended to describe static bias field devices, which are more commonplace than the self-field generators described in this thesis, by replacing the dynamic magnetic field term in equation 5.17 with a function describing the field from a permanent magnet. For example, assuming that the static field varies with depth into the sample over a length scale much larger than δ and can therefore be represented as a constant vector, $\mathbf{B}_{static}$, the equivalent surface pressure due to the static field can be calculated as:

$$\begin{aligned}
\mathbf{F}_{Lorentz} &= \int_0^\infty \mathbf{J} \times \mathbf{B}_{static}\, dz, \\
&= \int_0^\infty J_y^0(t) \exp\left(-z\left(\frac{1+i}{\delta}\right)\right) \hat{\mathbf{j}} \times \mathbf{B}_{static}\, dz, \\
&= \int_0^\infty \omega\delta\sigma \frac{i}{1+i} B_x^0(t) \exp\left(-z\left(\frac{1+i}{\delta}\right)\right) \hat{\mathbf{i}} \times \mathbf{B}_{static}\, dz, \\
&= \left[-\frac{i}{(1+i)^2}\omega\sigma\delta^2 B_x^0(t) \exp\left(-z\left(\frac{1+i}{\delta}\right)\right) \hat{\mathbf{i}} \times \mathbf{B}_{static}\right]_0^\infty, \\
&= \frac{1}{\mu} B_x^0(t) \hat{\mathbf{i}} \times \mathbf{B}_{static}.
\end{aligned} \tag{5.28}$$

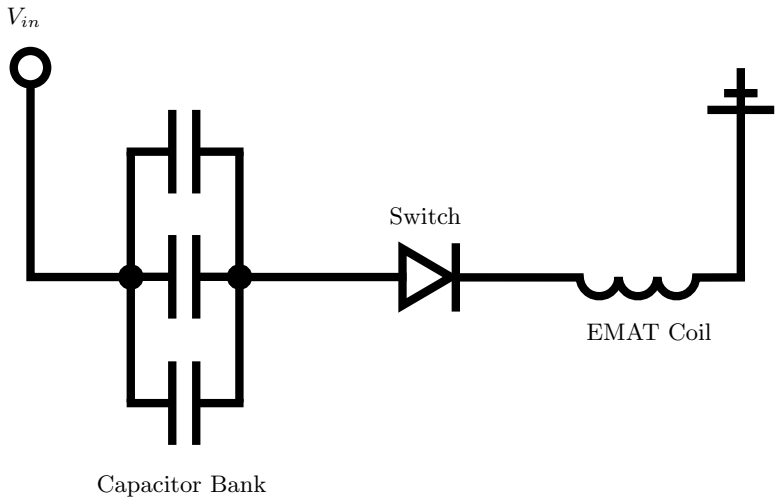

Figure 5.10: Schematic diagram of the high power EMAT pulse generation circuit. Charge is stored on a 470 nF capacitor bank at an input voltage, $V_{in} = 850V$. The EMAT coil has a resistance of 0.1 Ω and an inductance of 1.5 μH. Once the charge is stored, a solid state switching device is used to discharge the capacitor bank through the EMAT coil, which generates a transient current pulse with amplitudes up to 1.75 kA (see figure 5.11).

Using the method of complex images, $B_x^0(t)$ can be evaluated for an arbitrary coil configuration (as described in section 5.2.2) and hence the Lorentz pressure due to the static field can be calculated.

Figure 5.9 shows the calculated equivalent surface pressure due to the static field of EMAT with a tangential $\mathbf{B}_{static} = 1.4$ T and a 4 mm linear coil with a turn density of 5 mm^{-1} at a liftoff value of 0.2 mm and an excitation current of 1.75 kA. For comparison, the equivalent surface pressure due to the dynamic field for a linear coil with the same configuration is shown. The contribution from the dynamic field is over three times greater than that from the static field, demonstrating that at high current amplitudes, the quadratic dependence of the dynamic Lorentz force on excitation current leads to significantly larger induced pressure values than the static field contribution, which scales linearly with the current.

5.3 High Power EMAT Driving Circuit

Section 5.2 details a method for determining the magnitude of the self-field Lorentz force, but the time-variation of the Lorentz pressure must still be accounted for; the only time-varying component of equation 5.27 is the driving current, I, and hence knowledge of the driving current profile is required to determine the time-variation of the Lorentz pressure. As shown by equation 5.19, the magnitude of

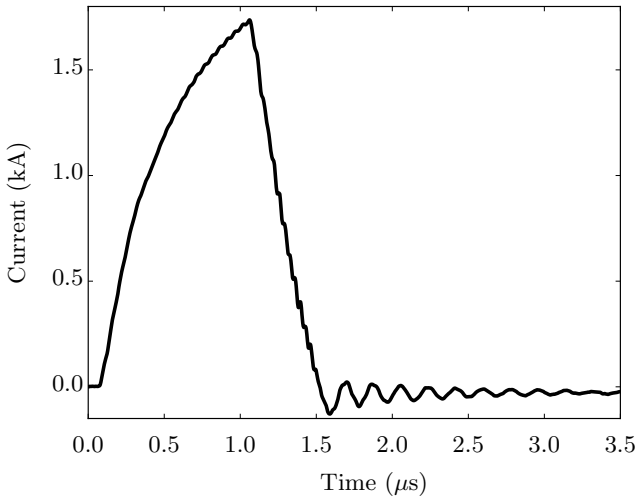

Figure 5.11: Excitation current pulse with a rise time of 1.0 μs and a peak value of approximately 1.75 kA. The resulting Lorentz pressure is proportional to the square of this current profile and is well-approximated by the square of a half-cycle of a sine wave (see figure 5.12).

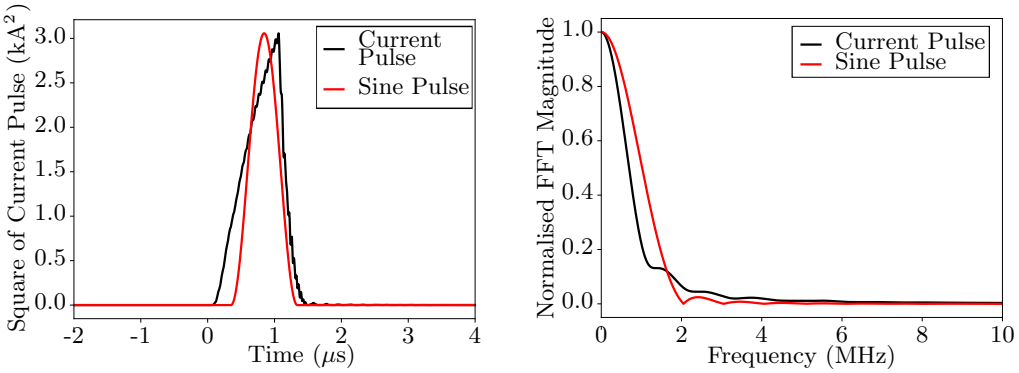

(a) Square of temporal current profile.

(b) Frequency spectrum of figure 5.12a

Figure 5.12: The square of the current profile depicted in figure 5.11 in the time (left) and frequency (right) domains. Shown in red is an approximation for the square of the current profile given by $\sin^2(2\pi t/T)$, where t is time, $T = 2.0$ μs and the function is windowed over one half-cycle.

the self-field Lorentz force scales with the square of the coil excitation current, and hence increases in driving currents can rapidly lead to relatively intense ultrasound generation. In practice, high current amplitudes are achieved using high-powered pulse generators, which consist of capacitor banks discharged via some switching device through a grounded EMAT coil. The pulse generator circuit used to drive the self-field generation EMATs in the experimental chapters of this thesis consists of a bank of capacitors, with total capacitance 470 nF, charged to an output voltage of 850 V (see figure 5.10).

To determine the temporal current profile generated by this circuit in a typical EMAT generator, an EMAT coil with a racetrack design was wound using 0.14 mm diameter copper wire and a current pulse from the excitation circuit was driven through it. The driving current in the coil was measured by placing a small resistance of 0.1 Ω in series with the EMAT coil, between the coil and ground, and measuring the potential drop across the resistance. The current was then calculated by dividing the measured voltage by the value of the resistance. The resulting current profile is shown in figure 5.11, which depicts a broadband pulse with a rise time of approximately 1.0 μs and a peak amplitude of 1.75 kA.

Since the Lorentz force acting on the sample is proportional to the square of the driving current, the induced mechanical forces arising from this current excitation has a higher frequency content than the temporal current profile itself. The Fourier transform of the square of the driving current profile was calculated and is plotted in figure 5.12a, alongside a Fourier transform of the square of a half-cycle of a sine wave with a period of 2.0 μs (an approximation for the current profile with rise time 1.0 μs). As seen in figure 5.12b, the highest frequency content in the temporal Lorentz profile is around 2 MHz, and the square of the half cycle sine wave provides a reasonable approximation to the generation function.

This approximate functional form for the temporal profile of the Lorentz force, alongside the functions describing the spatial distribution of the Lorentz pressure resulting from typical EMAT coil geometries, allows for evaluation of the resulting acoustic wavefields using the finite element method.

5.4 Calculation of Wave Fields Produced by High Power EMATs

In section 5.2, a semi-analytic method for evaluation of the equivalent surface loading stress produced by a high power coil-only EMAT was derived. Computation of the wavefield generated by these equivalent surface pressure distributions is useful to understand how the transducer coil geometry affects the directivity of the radi-

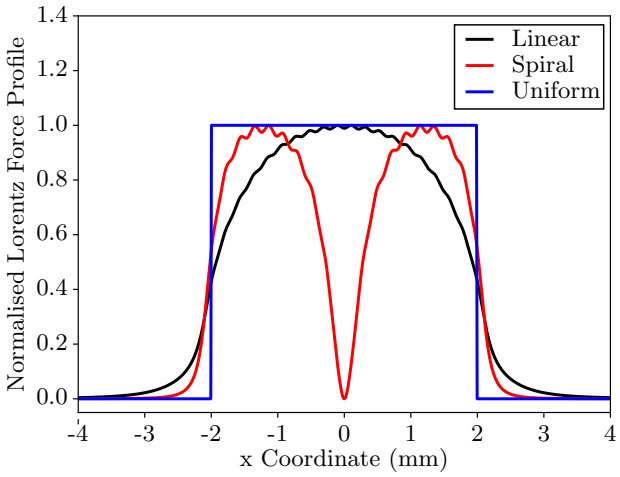

Figure 5.13: Comparison of the normalised Lorentz force loading profiles corresponding to linear, racetrack and uniform coil designs, used in the directivity analysis.

ated acoustic wave fields for the purposes of designing EMAT-based measurement systems.

Evaluation of the radiated acoustic wave field generated by a surface pressure load can be calculated analytically in some simple cases [151, 152, 153]. For the case of an arbitrary pressure distribution, numerical integration of the wave equation using the finite element method offers an approach that is generally applicable and accurate. In the analysis that follows, the finite element method is used to calculate and compare the radiated acoustic fields from different surface pressure distributions to establish qualitative differences in their directivity profiles. It is then possible to determine whether they are sufficiently different to warrant a full model of the electromagnetic field geometry, or whether they can be reasonably approximated by a uniform pressure source.

Linear and spiral or racetrack geometry coils are typically the most-appropriate choice for generation of normally-incident bulk ultrasound modes [106], and hence these coil geometries are investigated in the following analysis. Using the methods described in section 5.2, pressure loading profiles for 4 mm width linear and racetrack coils, each composed of 20 uniformly-spaced line sources, were calculated for a liftoff value of 0.2 mm. A coil width of 4 mm was chosen since, as described in more detail in section 6.4.1, this element width was empirically found to lead to good transmitted beam characteristics, and so analysis of this design is pertinent to the remainder of this thesis. A liftoff value of 0.2 mm was chosen, since this is approximately the liftoff value achieved in experiments in this thesis. A uniform

pressure loading profile with a width of 4 mm was also defined; a comparison of these pressure profiles is shown in figure 5.13.

A finite element model was defined using commercial software package PZFlex, which uses an explicit time domain integration algorithm for solving dynamic and elastic acoustic fields. Further details relating specifically to the finite element solver can be found in reference [154]. The model was defined as a uniform region of steel with dimensions of 110 × 220 mm, with the pressure load profile being applied at the centre of the upper surface. These model dimensions were chosen to ensure that the longitudinal and shear bulk modes would have sufficient propagation time to fully separate so that the waves for each mode could be analysed independently. The mesh was defined using simple linear two-dimensional quadrilateral elements with a density of 16 elements per wavelength, where the smallest wavelength of interest $\lambda_{min} = c_s/f_{max}$, where c_s is the shear wave speed (3150 ms^{-1}) and $f_{max} = 2.0$ MHz, giving an element size of 0.1 mm. The maximum timestep of 17 ns was determined as half of the propagation time of the quickest wavemode (a longitudinal wave traveling at 5950 ms^{-1}) across one element.

Following definition of the finite element grid, computation of the appropriate Lorentz force profile values to load the surface nodes with was achieved through spline interpolation of the calculated Lorentz force profiles shown in figure 5.13. The interpolated data was then used to determine the surface pressure load amplitudes at each of the relevant nodes on the model's surface. The temporal profile of the Lorentz force is identical at each node, since the model describes a single coil and not a series of independent point sources, and is simply the square of the temporal current profile the coil is excited with (see figure 5.12). Following the approximation presented in section 5.3, a half-cycle of the square of a 2 MHz sine wave was used as the temporal pressure load function. The amplitude of the profiles applied to the finite element nodes was 40 MPa in each case, as an order-of-magnitude estimation of the Lorentz force pressure (see e.g. figure 5.7). Since this model does not fully account for effects such as coil impedance, which would reduce the driving current amplitude between different coil designs of the same width and hence affect the Lorentz force amplitude, exact calculation of the Lorentz force pressure amplitude is not necessary. The aim of this section is to determine the differences in directivity, not amplitude, and since the governing equations for wave propagation are linear, identical results should be obtained regardless of the input pressure magnitude and an order of magnitude estimate is appropriate.

The output of the finite element model was the x and y velocity component history for each node in the finite element grid. The velocity vector magnitude was

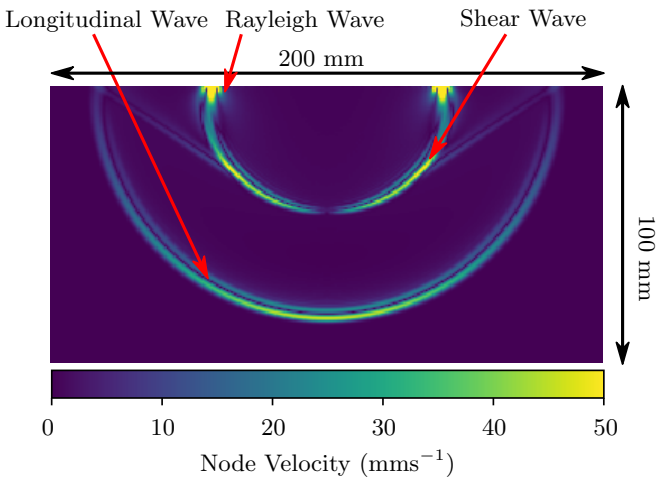

Figure 5.14: Acoustic wavefield, represented by the particle velocity, as calculated using the finite element method for the uniform pressure loading profile plotted in figure 5.13.

then determined to obtain the node velocity history. An example plot of the node velocity profile 15.8 μs after the start of the generation pulse for a uniform pressure distribution is shown in figure 5.14. For each choice of surface pressure distribution, the resulting acoustic wave field consists of several wavemodes. Compressional and shear ultrasound waves propagate in the bulk with greatly-varying directivity, and Rayleigh waves propagate along the surface. Comparison of the pressure load distributions was acheived through qualitative comparison of their directivity profiles, as computed from the finite element data.

Directivity profiles were determined for the longitudinal and shear bulk modes by defining a semi-circle about the centre of the generation source of radius 55 mm and computing the maximum velocity magnitude value in the time history data for each node lying on that semi-circle. Node velocity history data corresponding to times between 8.3 and 15.8 μs were accounted as longitudinal bulk wave signals, while the shear wave data were taken from velocity history data corresponding to times after 15.8 μs after the start of the generation pulse. To avoid inclusion of data corresponding to Rayleigh wave propagation, this data are only shown over an angular range from 10° to 170°. The directivity profiles for shear and longitudinal wavemodes are shown for the three surface pressure distributions in figure 5.15.

Although these pressure profiles act exclusively normally on the model surface and might naively be therefore assumed to be simple longitudinal wave sources, there is substantial generation of bulk shear modes at angles of 20 - 50 degrees from

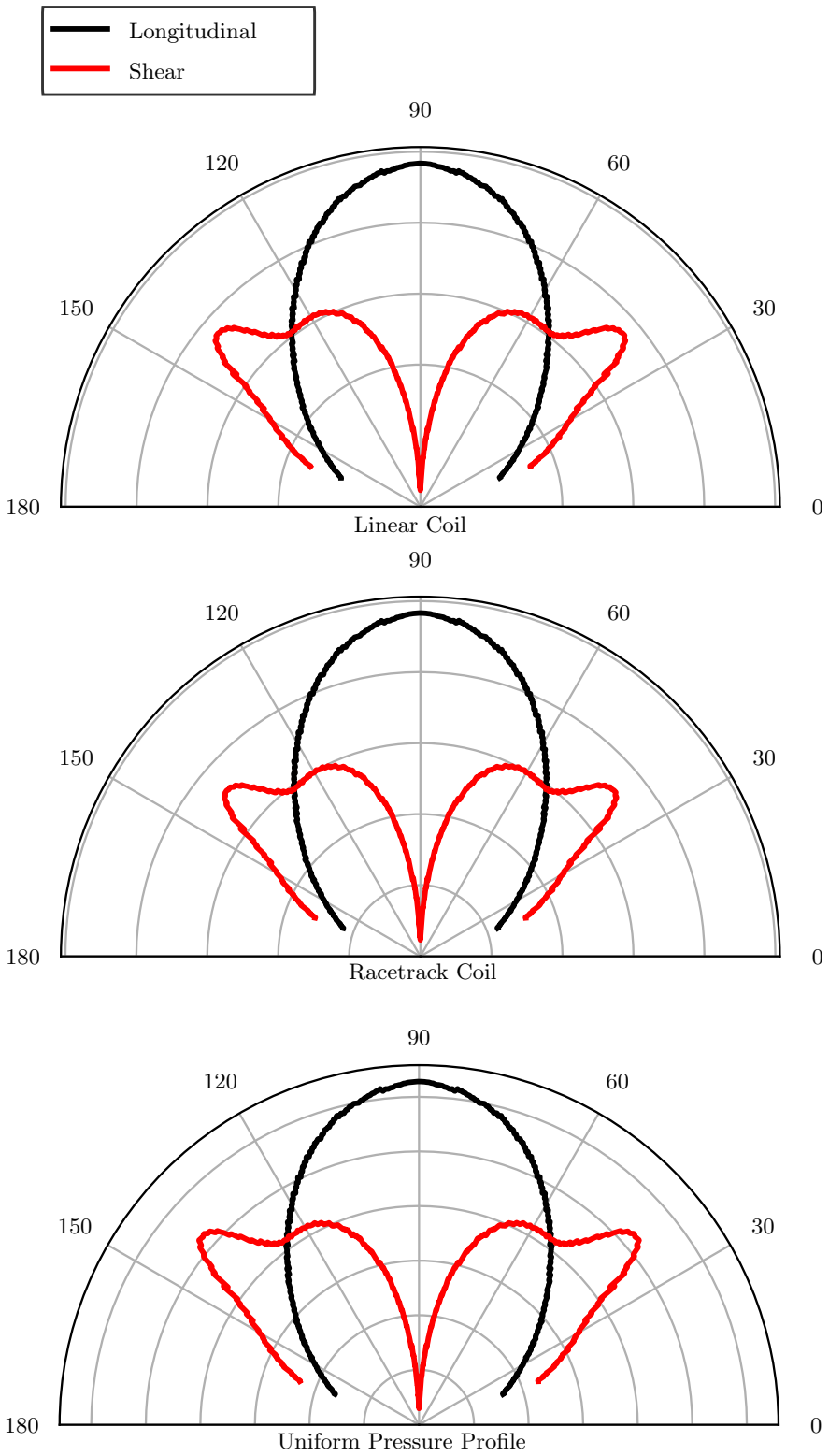

Figure 5.15: Longitudinal (black) and shear (red) mode directivity profiles resulting from pressure distributions corresponding to the linear, racetrack and uniform coil designs as depicted in figure 5.13.

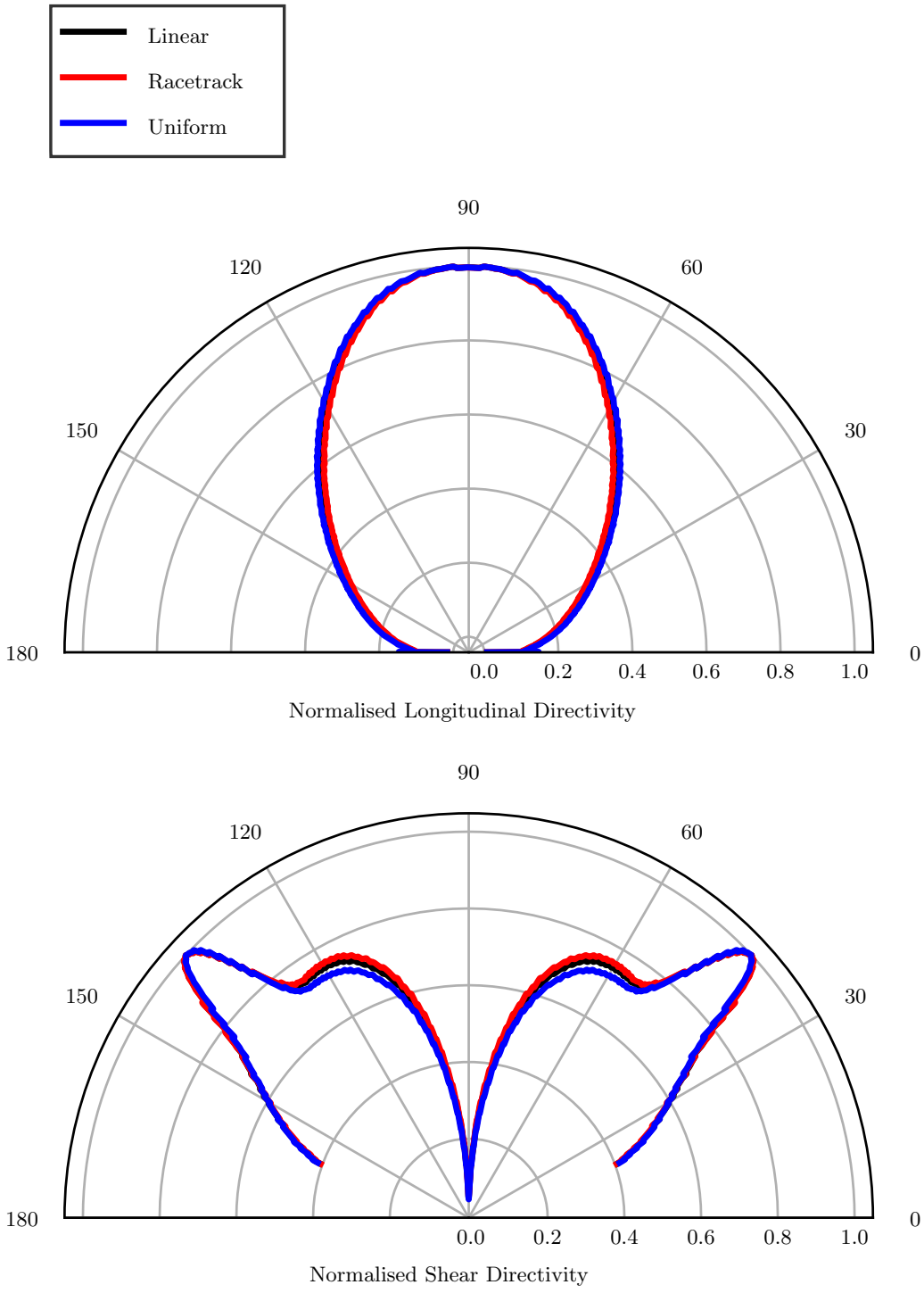

Figure 5.16: Normalised directivity plots of longitudinal and shear wave pulses generated by surface pressure profiles described by linear and racetrack EMAT coil designs, and a uniform pressure distribution.

Coil Design	Longitudinal - Shear Wave Amplitude Ratio
Linear	1.151
Racetrack	1.144
Uniform	1.135

Table 5.1: Ratios of the integrated longitudinal and shear wave directivity profiles for the linear, racetrack and uniform piston source pressure loading profiles plotted in figure 5.13. These values are in agreement to within 3%, suggesting that they are well-approximated by each other and that there is little benefit to a complete model of the Lorentz force pressure profile.

normal incidence at a higher amplitude than longitudinal wave modes over the same angular range. This is in good agreement with theoretical analysis of the radiation patterns of circular piston sources [151]. The directivity data plotted in figure 5.15 suggest that the choice of loading profile has little effect on the radiated acoustic wave field; in each case, the longitudinal wave is predominantly directed normal to the surface, and the shear wave directivity peaks at 50 degrees from normal incidence. Both the linear and racetrack pressure loading profiles can seemingly be well-approximated by a normally-acting uniform piston force. This is in agreement with theoretical models of transducer directivity [151, 152]; the value of ka, where k is the wavenumber and a is the transducer width, is low for these pressure load profiles (in each case, approximately 4 and 8 for the longitudinal and shear modes respectively). The radiation patterns therefore fall in the regime where the directivity is relatively low. If the value of ka was significantly larger, the directivity would be higher and the radiation patterns would be more distinguishable; for example, the two sides of the racetrack coil would behave as individual sources (empirically known to lead to beam artefacts when source separation approaches λ [124]). The implication of this result is that precise evaluation of the Lorentz surface pressure distribution induced by an EMAT coil is unnecessary, provided the model applies to the low ka regime, and that the correct amplitude value is selected.

Figure 5.16 shows a direct comparison of normalised directivity data for each source geometry for the individual bulk modes. A measure of the relative efficiency of shear wave generation for each pressure distribution can be calculated by numerically integrating the directivity profile over the full angular range and computing the ratio of the integrated longitudinal profile to the integrated shear profile. This also serves as a quantitative comparison of the directivity functions of each pressure source. The calculated shear to longitudinal directivity ratios are presented in table 5.1, and fall in a range from 1.13 - 1.15, demonstrating that

shear wave generation from these sources, although less than the longitudinal mode generation, is still significant and accounts for approximately 47% of the resulting bulk acoustic wavefield, as calculated from integration over the velocity directivity profile. These ratios are in agreement to within 3% for the different coil designs, suggesting that there is little quantitative difference between the radiated acoustic wave fields.

The results of the acoustic wavefield modelling suggest that a full model of the EMAT's dynamic field for determining the surface pressure load is an unnecessary complication, provided the value of ka for the transducer is low, and that uniform pressure loads give an approximate result that is sufficient for modelling self-field EMATs for bulk wave applications, as shown in section 6.4.1.

5.5 Conclusions

In this chapter, solution of Maxwell's equations for the electrodynamic fields produced by an induction coil above an infinite conducting half space were shown to lead to an equivalent surface pressure with magnitude $B^2/2\mu$. This surface pressure was shown to be exclusively repulsive, and lead to the generation of mechanical forces at the second harmonic of the driving current due to the force magnitude's proportionality to the square of the applied dynamic field. The method of complex images was then used in conjunction with this result to derive the magnetic field and Lorentz pressure produced by an infinitesimal wire source, with the analysis extended to coils of arbitrary geometry through summation over several individual wire sources. Evaluation of the resulting wave fields demonstrated that these sources are well-approximated by uniform pressure profiles, which suggests that rigorous models of EMAT surface pressure loading are not necessary, provided the value of ka is sufficiently small.

Chapter 6

Bulk Focusing EMATs

This chapter builds on the theoretical framework outlined in chapter 5 and concerns the development of a novel, phased EMAT generation array capable of focusing and transmitting longitudinal ultrasound pulses in thick and attenuative industrial as-cast steel samples.

6.1 Motivation for the Development of a Bulk Focusing EMAT

As outlined in chapter 1, there is a requirement from industry to perform product quality tests non-destructively and continuously during the casting process to allow feedback to the casting operators. This could, in principle, mitigate the development of internal defects, which both reduce the steel's sale value and in some cases present safety concerns [2, 155, 24]. Online detection of internal defects during the casting process presents a number of difficulties for conventional NDE techniques; as discussed in section 2.8 the large sample thickness of 120 - 300 mm, high operating temperatures, surface roughness and continuous movement of the sample preclude the consideration of established bulk measurement techniques such as radiography, and hence the case was argued for the development of an EMAT-based ultrasonic measurement system for detection of internal defects.

Ultrasound measurements have previously been identified as a realistic prospect of probing the surface and bulk of a cast slab and are the subject of previous studies on cast steel diagnostics [156, 157, 11, 158], but there still exist a number of challenges when attempting to use acoustics. Namely, the slab itself is relatively thick (up to 300 mm) and contains inhomogeneous and relatively large grain structures when compared to the expected dimensions of a casting defect (see section 1.2.3). Hence attenuation of ultrasound signals, in particular the higher-frequency

signals that have scattered from defects, will reduce detected signal amplitudes significantly. Additionally, previous studies have demonstrated that ultrasonic attenuation in metallic samples increases at high temperatures [157, 159, 160]. Although EMATs can overcome some limitations associated with conventional ultrasonic testing using piezoelectric transducers that limit their suitability for this application, problems associated with the large sample dimensions and coarse grain structures must still be overcome.

The anticipated attenuation of ultrasound signals in cast steel samples necessitates the use of relatively powerful EMAT devices; for this reason, chapter 5 concerns the development of a theoretical framework for describing the operation of an EMAT driven with high currents, such that the dynamic field Lorentz generation mechanism is dominant. EMAT generation relies on the scattering of conduction band electrons from metal atoms to impart momentum into the metallic lattice; this is an inefficient process, due to the small electron-atom mass ratio. This inherent inefficiency of electromagnetic ultrasound generation means that EMAT measurements typically suffer from poor signal-to-noise ratios, and this issue is compounded by the expected low signal amplitudes arising from the cast steel sample grain coarseness and high temperatures. This chapter concerns the development of a high powered phased array EMAT system to overcome this inherent drawback by developing an array of high-powered EMAT generators that can be excited with appropriate phase delays for the purposes of focusing the incident ultrasound beam and improving the transmitted signal amplitudes.

6.2 Phased Array Generation and Beamforming

One approach that can be taken to improve the signal-to-noise ratio of a measurement is to utilise a phased array to increase the signal amplitude through linear superposition; if the ultrasound signals are summed coherently, the resulting total signal amplitude increases, whilst any stochastic noise in the measurement sums incoherently. Enhancement of EMAT sensitivity by the geometric focusing of shear waves has been reported previously, however the approach taken relied on toneburst current excitations, which are more limited in power than the pulsed currents described in this work, and the dependence on geometric focusing prevented dynamic beamforming [161, 134, 162]. The novelty of the work described here is the development of a high power EMAT phased array, designed specifically for the inspection of thick, attenuative industrial samples.

Phased array generation and detection of ultrasound is a well-established technique for focusing and steering acoustic waves in both medical diagnostics and

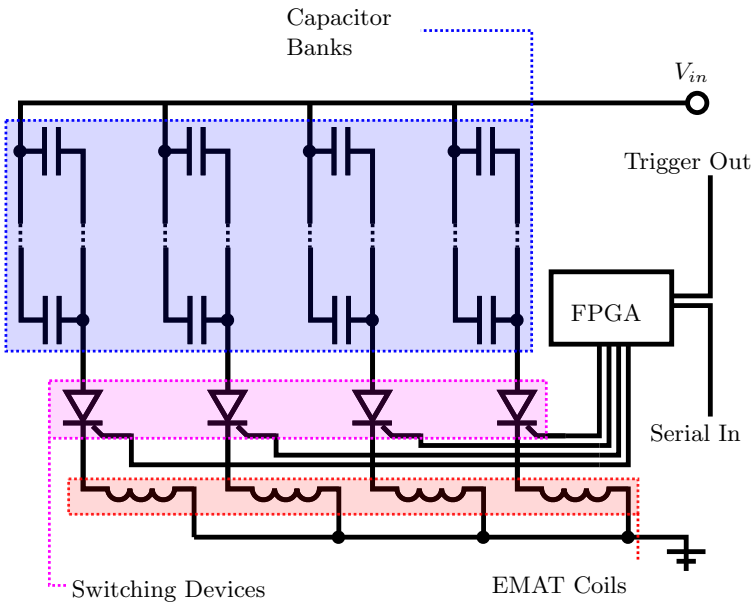

Figure 6.1: Schematic diagram of the phased array driving circuit. Each channel consists of a bank of capacitors that are charged to an input voltage, $V_{in} = 850$ V. For each channel, a solid state switching device is used to discharge the capacitor bank's current through the EMAT coils. A field-programmable gate array (FPGA) unit is used to apply phase delays on each channel.

NDE [115]. By applying appropriate phase delays to each element, a point in space can be chosen such that the wavefront from each element will arrive simultaneously, so that the acoustic beam is locally intense. In order to perform beam focusing, the phase delays are calculated by first calculating the propagation time from each element to the chosen focus, then subtracting the maximum propagation time from each element. The applied time delay, ϕ, can be expressed as:

$$\phi_i = \frac{\sqrt{x_{max}^2 + y_{max}^2}}{c_L} - \frac{\sqrt{x_i^2 + y_i^2}}{c_L}, \tag{6.1}$$

where the subscript i refers to the i^{th} element in the array, c_L is the longitudinal wave propagation speed, x is the displacement in x of the element from the focus, y is the displacement in y from the focus and the subscript max refers to the element that lies at the greatest distance from the focus.

The work presented here describes the development of a phased EMAT array generation system to enhance signals transmitted through the full thickness of as-cast steel slab samples.

6.3 EMAT Phased Array Driving Electronics

As discussed in section 5.2, coil-only EMAT designs require large dynamic currents for efficient ultrasound generation, and hence a bespoke excitation circuit. The driving electronics for the experimental tests of the EMAT generation array consist of a capacitor bank discharged through a solid state switching device for each channel (see figure 6.1). The phase delays are applied by a field-programmable gate array (FPGA) unit and have a temporal resolution of 2.5 ns. The temporal current profile of the excitation pulse was measured by placing a small resistance of 0.1 Ω in series with the EMAT coil being driven, as described in section 5.3. For a supplied pulse with a rise time of 1 μs, the peak current amplitude is 1.75 kA per channel (see figure 5.11).

The driving circuit of the individual channels is as described in section 5.3, and is similar to the driving electronics described by previous studies describing the development of a coil-only send-receive EMAT [163], but is capable of achieving much higher current amplitudes, and hence higher amplitude ultrasound waves, since the magnitude of the self-field Lorentz force scales with the square of the excitation current, as shown by equation 5.27. Even higher current amplitudes have been reported for a single coil using a spark-gap discharge driving circuit, although this is not as practical as a solid state switching method [145, 110, 163]. The solid state switching for each channel allows for accurate and reliable application of phase delays, which is essential for control of the phased array beam characteristics.

6.4 Finite Element Analysis

6.4.1 Pulsed EMAT Array Optimisation

A high power EMAT pulser system consisting of four independent channels with programmable time delays was developed for EMAT array measurements on cast steel samples. Prior to the development of an experimental EMAT phased array transducer, finite element models were used to determine optimal array parameters. Compared to typical commercially available piezoelectric phased array systems, which are capable of driving up to 256 independent channels [115], the number of output channels available on the phased EMAT pulser's driving electronics is low. Typically when designing a phased array of any kind, it is beneficial to adhere to the diffraction limit and maintain an element separation equal to, or less than, a half-wavelength. With such a limited number of elements, however, the aperture would be small when adhering to the diffraction limit and hence the expected beam characteristics would be poor. Moreover, the inherent inefficiency of EMATs necessitates

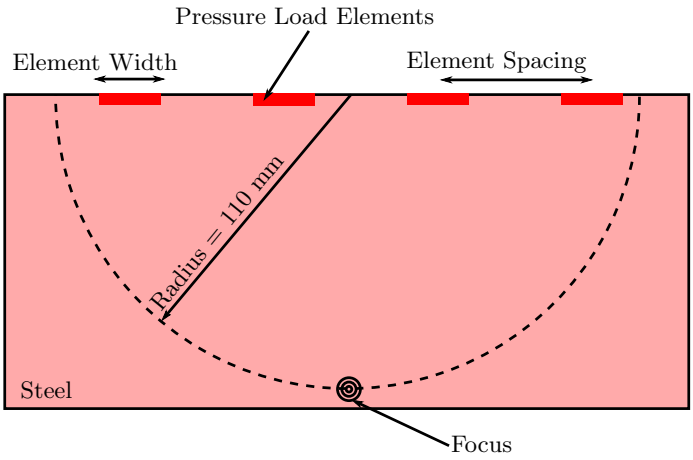

Figure 6.2: Schematic diagram of the finite element model geometry used for the optimisation study. EMAT elements were modeled by applying a spatially-uniform, temporally-varying pressure load on appropriate elements on the sample surface.

relatively large transducer footprints for practicable signal-to-noise ratios, making adherence to the diffraction limit difficult. A finite element study was therefore conducted to ascertain the best array parameters (element separation and element width) to achieve both a narrow beamwidth and sufficient sidelobe suppression.

Analysis of the self-field Lorentz generation mechanism indicates that the coil-only design can be approximated as a rectangular piston source (see section 5.4). Each EMAT element was therefore modeled by applying a uniform, time-varying, pressure profile across the relevant surface nodes in the model. Analytical modeling of the self-field mechanism indicates that the Lorentz force is proportional to the square of the driving current, leading to a doubling of the frequency content in the case of harmonic time dependence. The square of a half-cycle of a sine wave with a period of 2.0 μs was therefore chosen as the driving function for the pressure load in the model, to approximate the temporal pressure variation supplied by a coil-only EMAT driven by the current profile shown in figure 5.11. A pressure amplitude of 40 MPa was selected as an order-of-magnitude approximation as determined from semi-analytical modeling.

The slowest expected bulk wave velocity in steel, the shear velocity, c_S, is approximately 3150 ms^{-1}, depending on the elastic constants of the sample being considered. The Fourier spectrum of the driving function indicates there is significant frequency content in the acoustic wave up to a frequency value, $f = 2.0$ MHz. In this model, the smallest expected wavelength of an ultrasound wave propagating in the bulk of the sample, λ_{min}, is therefore approximately $\lambda_{min} = c_S f^{-1} = 1.6$ mm. A finite element grid was meshed with an element density of 16 elements per wave-

length in order to avoid numerical artefacts arising from coarse meshing relative to the wavelength [154]. Simple linear two-dimensional quadrilateral elements with a size of 0.1 mm were therefore used to construct the finite element model, and the timestep was chosen to be 17 ns, since this corresponds to half of the propagation time of a longitudinal acoustic wave across one element.

Internal defects of interest in cast steel, such as segregation defects and associated cracking, are likely to lie along the centreline, which in a 225 mm thick slab is at a depth of approximately 110 mm below the sample surface [164, 165]. Phase delays were therefore applied in accordance with equation 6.1 to model the focusing of an incident longitudinal ultrasound pulse at a depth of 110 mm (see figure 6.2). The EMAT pulsing system available for experimental use has four channels, and so for meaningful comparison of the model with experimental results, a four-element EMAT generator was modeled in this way.

The EMAT generation array can be characterised in terms of two defining parameters; the element separation (the distance between the centre nodes of adjacent elements) and the element width (the width of the active element region). The aim of the study was to obtain the optimal values for these parameters to achieve a narrow beam width and high directivity in the generated beam.

A series of simulations were run in which the element width was kept constant at 1 mm and the element separation was varied between 1 and 20 mm. The model output was a two-dimensional grid of pressure history data for each node in the simulation. The beam profile was obtained by defining a semi-circle with radius 110 mm about the centre of the array and plotting the maximum absolute values from the pressure histories of the corresponding nodes as a function of angle from normal incidence. Associated uncertainties are estimated using the difference between values at the intended propagation angle and the values recorded at the nearest nodes on the grid. The beam profile was then parameterised in terms of the 3 dB beam width (the angular range in which the beam amplitude is greater than, or equal to, half of the maximum amplitude, see figure 6.3a) and in terms of the logarithmic ratio of integrated beam amplitude within the 3 dB beam width to integrated amplitude outside of the 3 dB beam width. The first parameter serves as a metric for comparing the directivity of the main beam lobe; a narrower beam width gives a more localised high pressure region, which is beneficial when aiming to separate defect indications that lie laterally close to each other. The second parameter serves as an indication of the relative amplitude of the main lobe; if the ratio is low, then more of the beam energy is directed outside of the main beam width and away from the intended target region, leading to regions of high localised amplitudes other than the intended focus,

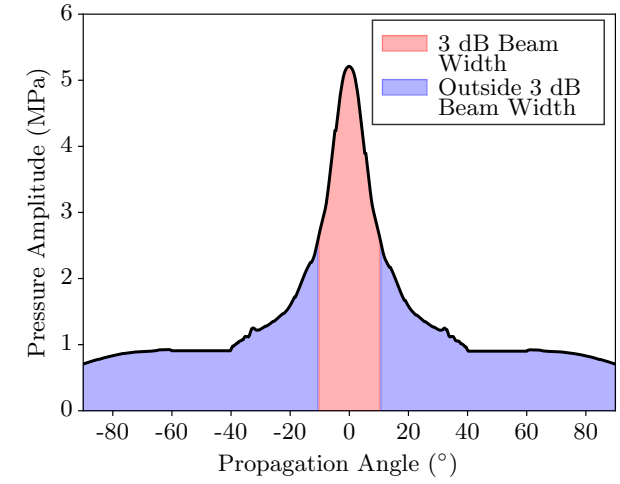

(a)

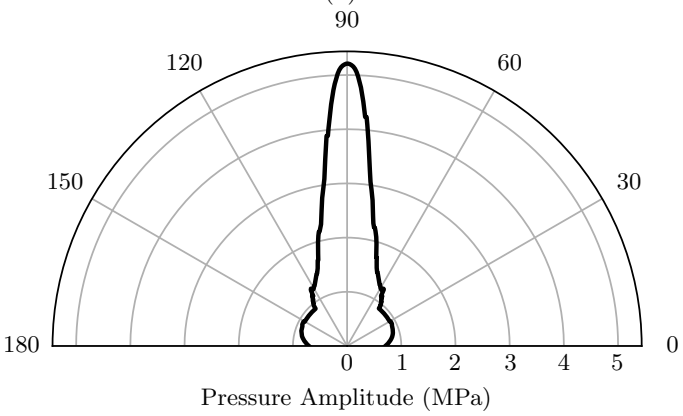

(b)

Figure 6.3: Example simulated beam profile data for a four-element array with element spacing 6 mm and element width 4 mm for a chosen focal point at a depth of 110 mm.

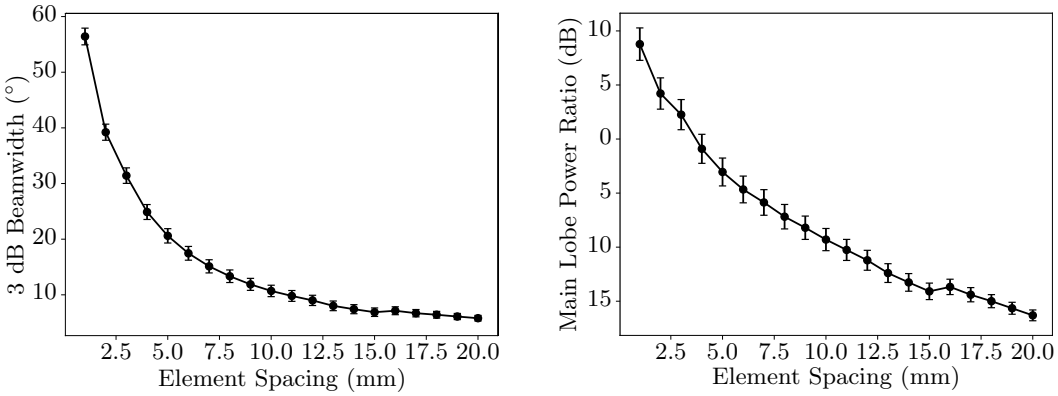

Figure 6.4: Modeled variation of the 3 db beamwidth (left) and main lobe power ratio (right) with element spacing for a four-element phased array with 1 mm wide elements.

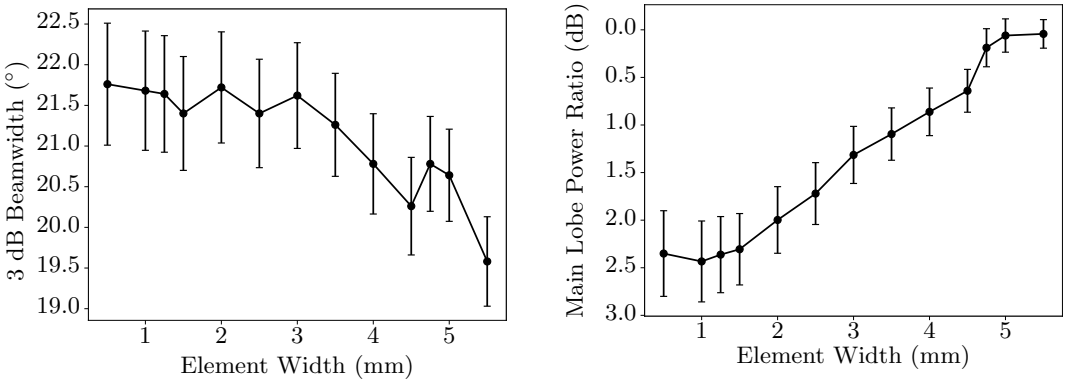

Figure 6.5: Modeled variation of the 3 db beamwidth (left) and main lobe power ratio (right) with element width for a four-element phased array with an element spacing of 6 mm.

and therefore potentially confusing attempts at defect localisation using a focused beam.

The results from this series of simulations are displayed in figure 6.4. The overall observed trend is that an increased element separation reduces the 3 dB beam width, which is desirable, though at the expense of increasing power distributed outside of the 3 dB beam width. This is to be expected; the larger array aperture leads to a more well-defined focus, however since the number of elements in the array remains constant, each increase in aperture size moves the element separation further away from the diffraction limit and hence more energy is distributed outside of the main lobe.

This can be to an extent mitigated by choosing a suitable element width. Figure 6.5 displays the beam characteristics modeled by choosing an array separation of 6 mm and varying the element width between 0.5 and 5.5 mm. It is observed that wider elements reduce the proportion of energy outside of the 3 dB beam width for a marginal decrease in beam width; the total variation over the range of element widths is small and within the estimated uncertainty range resulting from truncation errors associated with grid discretisation. Intuitively, this can be explained through the consideration of each element as a normally-acting piston source. As the element width increases, proportionally more of the energy is directed downwards compared to a smaller element, for which contributions from the piston edge are proportionally greater and lead to non-normally-incident wave generation.

A full optimisation would require modeling array parameters throughout the two-dimensional parameter space, however it is clear from modeling with the fixed width and separation values that the choice of a large aperture with large elements leads to smaller beam widths with a higher proportion of energy within the 3 dB beam width. The data in figure 6.4 show that large increases in element separation beyond 10 mm produce diminishing returns in terms of beam width, with the minimum achievable beamwidth being approximately 10°. It was therefore decided that an EMAT array with element separation of 6 mm and with element widths of 4 mm provided a suitable compromise between narrow beam widths and suppressed distribution outside of the beam width. This choice of design gives a 3 dB beam width of 20°, which corresponds to a lateral size of 80 mm in the centreline region (110 mm away from the transducer).

6.4.2 Phased Array Signal Enhancement

Using the optimised array parameters obtained in section 6.4.1, it is possible to determine the expected improvement in signal amplitude that results from phased

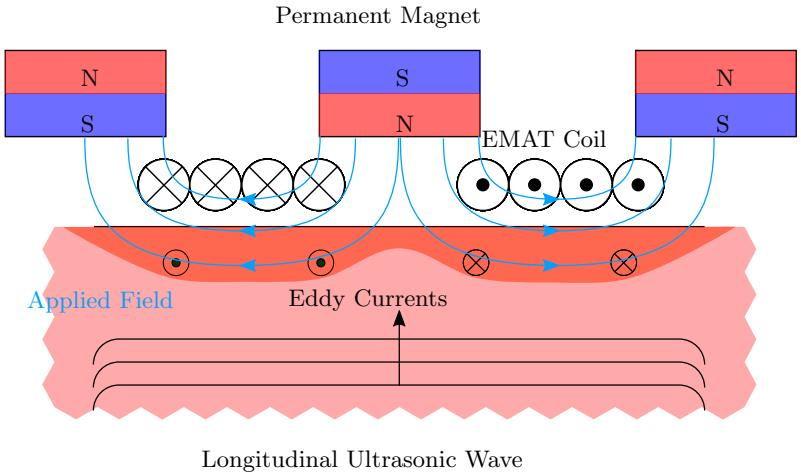

Figure 6.6: When an EMAT is used as a detection device, the oscillatory motion of the conducting sample's surface in the presence of a bias magnetic field generates eddy currents in the sample, which can be detected using an induction coil near the sample's surface. A bias magnetic field is always required when operating an EMAT as a detector, hence most designs utilise permanent magnets.

array generation. A finite element model was constructed in which a four-element EMAT array on the upper surface of a 225 mm thick steel block focused an incident longitudinal ultrasound pulse on the opposing surface directly underneath it. The driving function and mesh density were as described in section 6.4.1. All of the model's boundaries were this time modeled as free surfaces, to accurately account for the physics of the ultrasonic signals incident on the sample's lower surface (instead of modeling the lower surface as an absorbing boundary, as done in section 6.4.1).

An EMAT detector is sensitive to surface particle velocity, and hence in order to model the signal as detected using an EMAT, the velocity vector history was recorded for each node in the simulation grid. Nodes on the lower surface were chosen which corresponded to an EMAT detector, with a footprint described by figure 6.9 (the geometry of the EMAT detectors used for experimental validation in this study), placed directly opposite the generation array. Out-of-plane velocity components in the bias field shown in figure 6.6 generate opposing eddy currents under each half of the detection coil (since the in-plane field has opposing polarities beneath each half of the coil), and hence out-of-plane particle velocities at surface nodes corresponding to the detection coil can be directly summed to obtain a proxy of the voltage signal as measured by the inductor coil. The out-of-plane bias field components do not have opposite polarities under each half of the coil, however, and so for a velocity vector that lies in the plane of the surface, unidirectional eddy currents are generated, leading to the induced currents in the detection coil

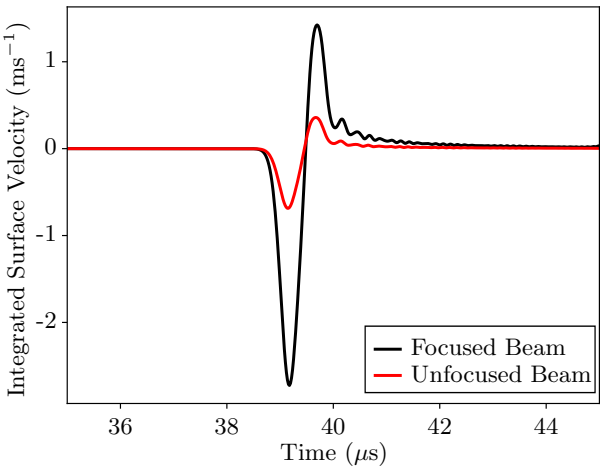

Figure 6.7: Finite element analysis demonstrates a factor of 3.7 improvement in the peak to peak amplitude of the transmitted longitudinal ultrasound signal from a four-element phased array when compared to a single element.

canceling each other. In-plane particle velocities at the coil surface nodes were therefore summed over each half of the coil and then subtracted to account for this cancellation effect.

The resulting values give a measure of the calculated relative amplitude of the expected EMAT signal, however the numbers are not directly comparable to experimental measurements without a full model of the EMAT detection device. This is an unnecessary complication due to the non-trivial field geometries arising from the permanent bias field and its interaction with the steel sample, the dependence of eddy current densities on sample properties and the degree of mutual inductance between the detection coil and the sample. Instead, it is sufficient to compare the difference in amplitude between similar models of a single EMAT element and a phased array to determine the expected signal enhancement from using the phased array approach.

The resulting velocity histories, summed over the appropriate nodes, are shown for the cases of a single EMAT generation element and generation by a phased array in figure 6.7. The difference in the peak-to-peak amplitude of the incident longitudinal pulse is a factor of 3.7. This result is to be expected, since it is approximately equal to the number of extra elements applied (though it is expected to be lower than 4, since attenuation losses at the focal point from the outer elements will be greater than for an element positioned directly above the focus, due to the increased path length).

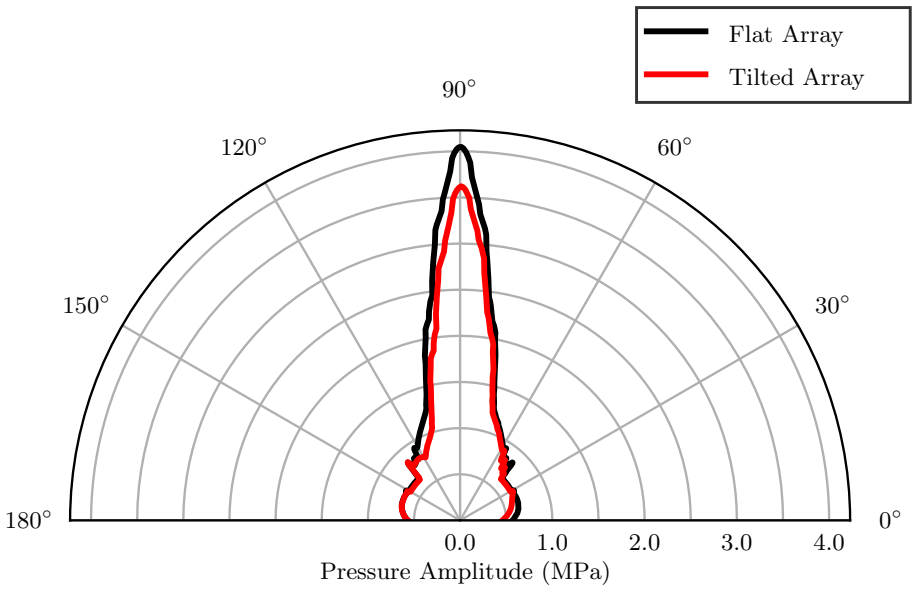

Figure 6.8: A comparison of beam directivity for an array with no inter-elemental liftoff variation, and an array with a liftoff difference of 0.1 mm between successive elements.

6.5 Inter-Elemental Liftoff Variation

The preceding sections consider the focused beam shape and signal enhancement of an array of generation elements on an idealised flat surface. The intended application for this array is on an industrial as-cast surface, which has surface roughness due to oxide scale and oscillation marks. It is therefore necessary to investigate the effects of inter-elemental liftoff variation to ascertain whether the ultrasonic beam generated by the phased array device is robust to industrial conditions.

Previous studies concerning ultrasonic measurements using EMATs during continuous casting do not suggest that sensor liftoff variation is a significant problem [108, 76]. An assumption that liftoff variations between adjacent elements would be small is therefore justifiable. Here two scenarios are compared: one in which all elements are held flush to the sample with a liftoff value of 0.2 mm, and one in which the generation array is tilted such that each successive element has a liftoff value of 0.1 mm greater than the preceding element (so that the element liftoff values are 0.2, 0.3, 0.4 and 0.5 mm respectively). The corresponding pressure amplitude values, as determined using the same methods used to calculate the equivalent surface pressure profiles shown in figure 5.7, are 3.4, 3.1, 2.9 and 2.7 MPa respectively.

The geometry of each modelled array was chosen to match the optimal parameters found in section 6.4.1, with an element width of 4 mm and an inter-

elemental separation of 6 mm. The beam directivity profile for each array configuration was calculated in the same way described in section 5.2.2. A comparison of the beam directivity is shown in figure 6.8. The directivity of the tilted array is asymmetric, which is an expected result considering that the arrangement of generation sources in the array is now also asymmetric. Correspondingly, there is a slight decrease in the 3 dB beamwidth from 20.0° to 19.5°, although this result is not significant and falls within the numerical error range associated with the grid discretisation. Qualitatively, figure 6.8 demonstrates that there is no significant variation in the beam directivity due to array tilting.

The amplitude of the pressure waves generated by the tilted array is lower than for the flat array, which is expected, because higher liftoff values correspond to lower surface pressure values, and hence less total energy input into the sample. The difference in the beam amplitude for these configurations is approximately 10%, demonstrating that although there is a loss in generated wave amplitudes due to array tilting, the method of phased array generation for the purpose of enhancing incident acoustic waves should be robust to inter-elemental liftoff variation; the expected enhancement factor, determined in figure 6.4.2, would reduce from 3.7 to 3.3, which is still a significant enhancement.

6.6 EMAT detector design

A coil-only EMAT generator predominantly excites mechanical forces that lie out of the sample's surface plane, and hence lead primarily to longitudinal wave generation (see section 5.2). Efficient detection of these transmitted longitudinal signals therefore requires an EMAT design that is sensitive to out-of-plane particle motion, and hence requires a static bias field with significant in-plane components. This is relatively difficult to achieve, since the permanent magnet supplying the bias field must lie above the sample surface and because the in-plane magnetic flux density falls rapidly with distance from the magnet's edge. Most longitudinal EMAT designs therefore involve winding an inductor coil around the edge of a permanent magnet, where there are significant parallel and perpendicular components to the field. Such a design leads to a large parasitic inductance in the coil, however, and the small area over which there are parallel field components leads to relatively weak received signals. For the application of bulk wave measurements in thick steel casts, it is important to optimise the detection EMATs, since the sample's thickness and high attenuation leads to small detectable signals.

Newer EMAT designs have considered the positioning of a flat spiral detection coil between magnets of alternating polarity [166] (see figure 6.6). The chief

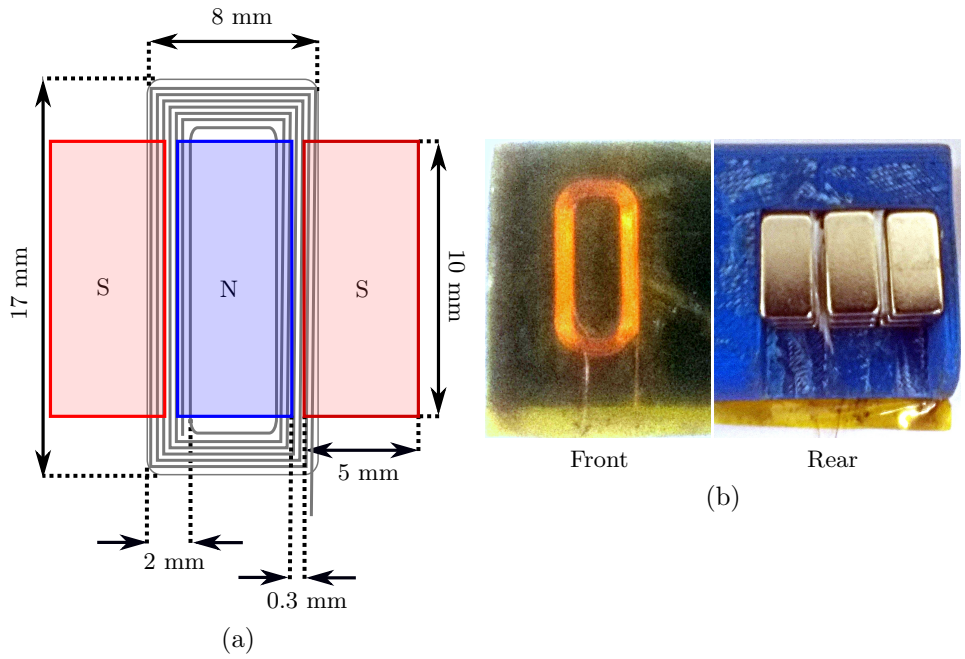

Figure 6.9: Schematic diagram depicting the coil dimensions of the detection sensor, and photographs depicting the coil and permanent magnet arrangement.

advantage of these designs is that they reduce the parasitic inductance in the coil and expose more of the coil's length to the sample, and so lead to more efficient detection of longitudinal ultrasound waves. Since the coils are still placed at the magnet edges, there is still in-plane particle motion sensitivity, and hence these designs are also suitable for detection of shear wave modes.

A longitudinal EMAT detector was constructed using $5 \times 10 \times 2.5$ mm NdFeB magnets. A 3D printed housing was used to hold three stacks of three such magnets with alternating polarities at a separation of 0.3 mm, and to align the inductor coil correctly in the resulting gaps between the magnets. Copper wire with a 0.14 mm diameter was used to wind a racetrack coil, with track width 3 mm, into the plastic template grooves beneath the magnets such that its edges lay under the magnet's edges. The coil was encased in kapton tape (see figure 6.9).

6.7 Experimental Validation of Signal Enhancement

Experimental validation of the amplitude enhancement observed in the finite element modeling was achieved using a four-element high power EMAT pulser and a series of EMAT generation coils wound into a 3D printed plastic template to ensure tight control over element width and spacing. The EMAT array's generation coils were wound into a 3D printed template using 0.14 mm diameter copper wire enclosed in

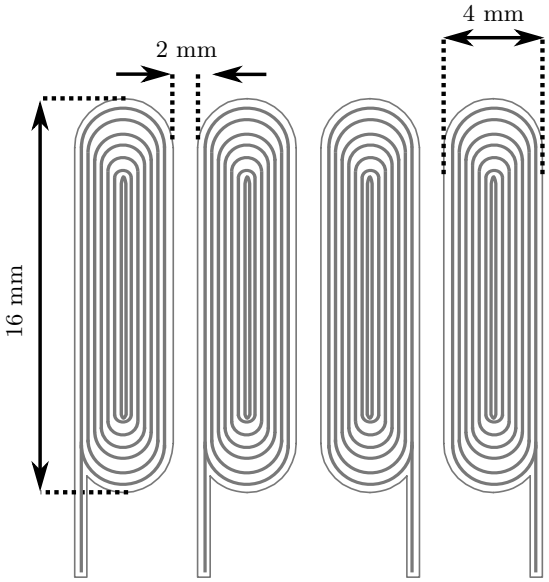

Figure 6.10: Schematic diagram depicting the coil dimensions of the generation array.

kapton tape. The parameters of the array (element spacing and width) were chosen on the basis of the finite element study presented in section 6.4.1, and so the width of each individual racetrack coil element was 4 mm, with the distance between the centres of adjacent elements being 6 mm (see figure 6.10).

Phase delays of 0.0 μs on the outer two elements and 27 ns on the inner two elements were applied in accordance with equation 6.1 to the four-element generation array to focus an incident pulse of longitudinal waves on the opposing face of a 225 mm thick as-cast steel slab sample. A single edge-field detection EMAT (constructed as described in section 6.6) was placed directly opposite; this was connected to an amplifier, which was then connected to an oscilloscope to measure the time-dependent voltage across the detection coil (see figure 6.11). An A-scan recording of the voltage history resulting from phased array generation was compared to the signal recorded when a single generation element, placed directly opposite the detection coil, was fired (see figure 6.12). These measurements were taken with no coherent averaging, but were digitally filtered using a Butterworth bandpass filter with low and high pass bands of 0.1 and 5.0 MHz respectively. Coherent noise is present in this data, and is likely a result of scattering of acoustic waves from grain structures in the material, and reflections and mode-conversions of acoustic waves at the sample boundaries.

The received signals demonstrate a clear improvement in transmitted signal

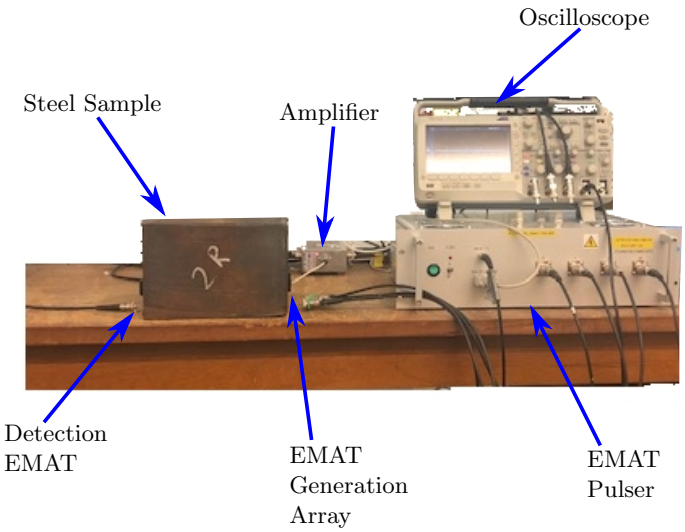

Figure 6.11: Schematic diagram of the experimental setup. The EMAT pulser (described in figure 6.1 drives the EMAT generation array (described in figure 6.10), which generates a focused longitudinal ultrasound wave. This is detected on the opposing side of the as-cast steel slab sample by the detection EMAT (described in figure 6.9). The signal is passed through an amplifier before being recorded on an oscilloscope.

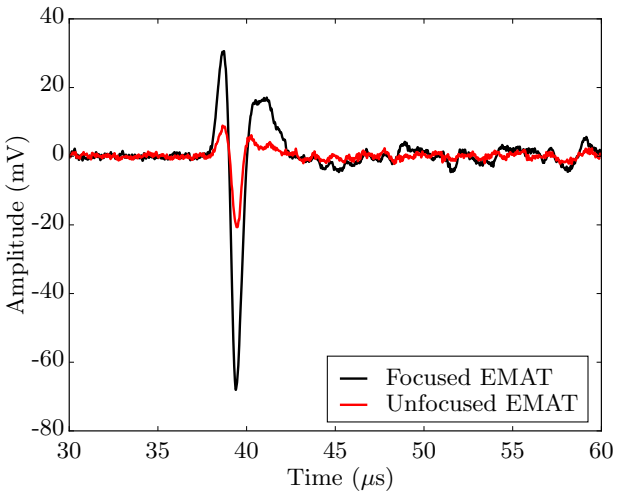

Figure 6.12: Experimental data demonstrating the enhancement of a longitudinal ultrasound signal transmitted through a 225 mm thick as-cast steel sample when using a four-element phased EMAT generation array. The signal amplitude is improved by a factor of 3.5 when compared to a single element, which is in good agreement with the factor of 3.7 improvement predicted by finite element analysis (see figure 6.7)

amplitude by a factor of approximately 3.5 when using a four-element phased array generator instead of a single EMAT. This figure is in good agreement with the expected enhancement by a factor of 3.7 determined from finite element analysis, as discussed in section 6.4.2.

6.8 Enhancement Using a Detection Array

The amplitude enhancement demonstrated by the use of a four-channel generation array can be further improved through the coherent addition of the transmitted signal as detected using an array of detection EMATs. Using the design outlined in section 6.6, an array of three detection EMATs was constructed with spacings of 30 mm between adjacent elements. The transmitted signal from the coil-only array generating at the opposite end of the sample and focusing at a depth of 110 mm was recorded independently on each detection channel. The transmitted longitudinal pulse signal was identified in the A-scan trace recorded by the central element in the detection array and cross-correlated with the data from each channel to determine the phase separation of the signal as recorded by each element. Relative phase lags of 2.10 μs (between channels 1 and 2) and 1.53 μs (between channels 2 and 3) were determined from the cross correlation. These phase delays were then applied to A-scan data from channels 1 and 3, before summing all three channels produce a single A-scan data set with enhanced amplitude in the longitudinal signal.

The principle of noise reduction through this delay-and-sum method is that any genuine ultrasonic signals arriving in the expected time intervals should be coherent and add constructively, whereas any noise due to stochastic processes should sum to zero if enough independent measurements are considered. This method therefore enhances ultrasound signals in the chosen time window and suppresses information which is not coherent between the independent measurements and is therefore likely composed of random noise. Assuming there are no physical differences between the signals detected by adjacent elements (additional signals from defects or differences in the signal of interest, which arise due to the different spatial positions of the elements), the method is identical to the concept of coherent averaging, and thus is expected to improve the signal to noise ratio by a factor of $\sqrt{N}$, where N is the total number of elements used for detection and the signal and noise are parameterised in terms of their root mean square values [167].

The signal-to-noise ratio of an acoustic signal is here defined as 20 times the base 10 logarithm of the ratio of the root mean square of the sections of the A-scan trace that correspond to the signal of interest and which correspond to regions

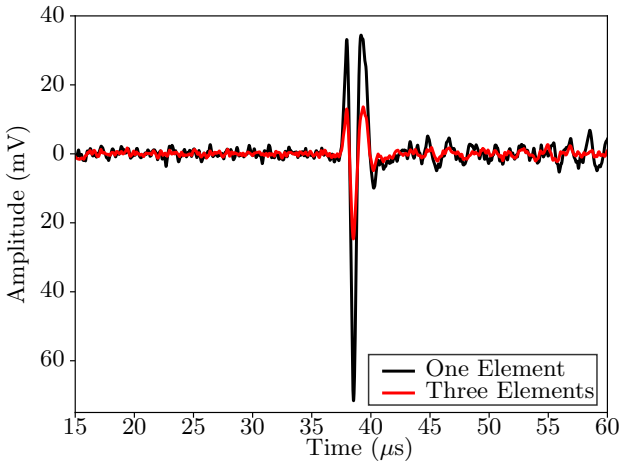

Figure 6.13: Comparison of the transmitted signals as received by a single EMAT detector and as received by three separate detectors after coherent summation. The improvement in the signal-to-noise ratio is 5.75 dB, which is comparable to the 4.77 dB improvement expected from the application of three coherent averages

containing only noise, where no signals are expected:

$$SNR = 20\log_{10}\left(\frac{\sqrt{\frac{1}{n_{sig}}\sum_i S_i^2}}{\sqrt{\frac{1}{n_{noise}}\sum_i N_i^2}}\right), \tag{6.2}$$

where SNR is the value of the signal-to-noise ratio in decibels, n_{sig} and n_{noise} are the number of discrete values in the time series corresponding to the signal and noise sections of the data respectively and S_i and N_i are the i^{th} respective amplitude values of the signal and noise time series. In the A-scan data presented in figure 6.13, the signal was defined as the transmitted longitudinal pulse recorded between 37.0 and 41.0 μs. The section of the A-scan trace beyond 41.0 μs was not considered for the signal-to-noise ratio comparison, since it is not strictly composed only of stochastic noise; spurious scattered and mode-converted signals from grain structures in the sample would be expected to arrive after the main longitudinal pulse, and so the data in this region contain genuine acoustic signals that contain some information relating to the sample's grain structures. The noise was instead defined as the region between 15.0 and 35.0 μs, since it is physically impossible for acoustic signals from the generation source to be detected in this time window, and hence the data here represent genuine stochastic noise. The signal-to-noise ratios of the A-scans corresponding to the single detection element and to the coherent summation of

signals from three detection elements (shown in figure 6.13) were calculated to be 25.67 dB and 31.42 dB respectively. The difference between these two values is 5.75 dB, which is comparable to the expected improvement due to coherent summation of 3 measurements ($20\log_{10}\left(\sqrt{3}\right) = 4.77$ dB), indicating both that the delay and summation method does improve the signal-to-noise ratio, and that it is identical to the coherent averaging method in the absence of spurious signals between elements.

6.9 Side-Drilled Hole Detection

With sufficient signal-to-noise ratio on detected ultrasound pulses propagated through the full thickness of a cast slab sample, it is possible to begin looking at detection experiments for internal defects. A four-element phased generation array was placed on the upper surface of a 320 mm thick steel sample with a 6 mm diameter side-drilled hole centred at a depth of 160 mm (see figure 6.14). Phase delays were applied in accordance with equation 6.1 to focus the incident longitudinal beam on the defect. A detection EMAT was placed adjacent to the generation array to record any backscattered ultrasound signals.

Close proximity of the detector coil to the high current generation devices can saturate the amplifier and make detection of reflected ultrasound signals difficult. To an extent, this can be overcome through careful consideration of the relative positioning of the detection and generation coils. The generation elements used here are elongated, rounded rectangles or 'racetrack' shapes, and so the largest magnetic flux density during excitation occurs perpendicular to the long axis of the coil. Detection coils in close proximity exposed to this long axis become saturated during the excitation pulse. This effect can be mitigated by providing a suitable separation (30 mm) between parallel generation and detection coils, but this comes with the complication that the detection coils are aligned to efficiently detect Rayleigh waves, which mask signals arriving from the sample's interior. Instead, the coils can be aligned perpendicular to the generation array elements as shown in figure 6.14, which both exposes much less of the coil to the largest flux densities and so allows for smaller coil separations, and is a configuration that is less favourable for efficient detection of Rayleigh waves.

Using the coil arrangement described in figure 6.14, a pulse-echo ultrasound A-scan was recorded on the 320 mm thick steel sample (shown in figure 6.15). Although the chosen coil orientation prevents amplifier saturation, the close proximity of the detection coil to the generation coils gives a dead time of 20 μs. The data were therefore processed, firstly by windowing away the generation noise before 20 μs, before fitting the A-scan trace with a 7^{th} order polynomial and subtracting the

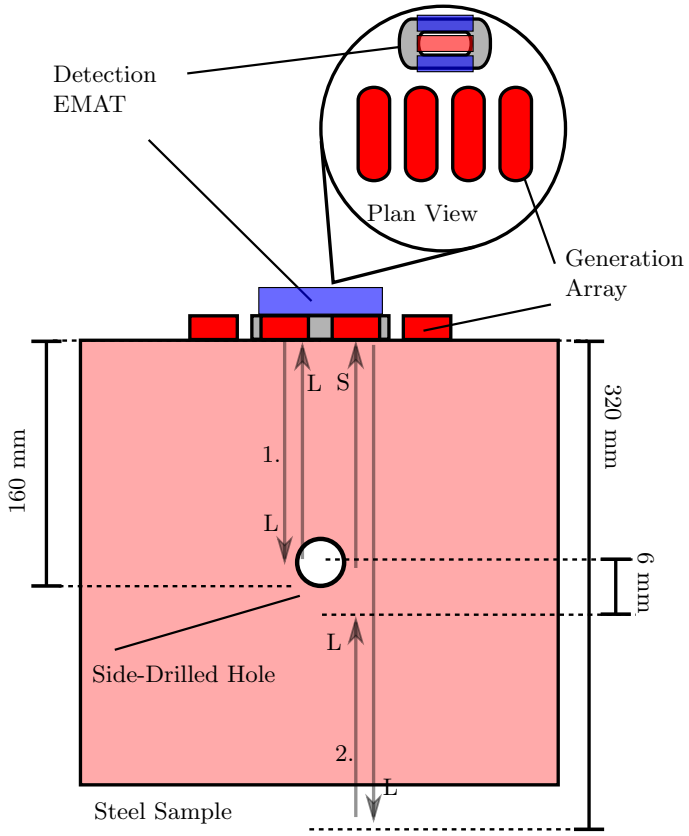

Figure 6.14: Schematic diagram of the pulse-echo experiment setup. Path 1 corresponds to an incident longitudinal pulse (L) that is back-scattered at the defect, and path 2 corresponds to a longitudinal pulse that is reflected off the sample's backwall as a longitudinal wave before mode-converting to a shear wave (S).

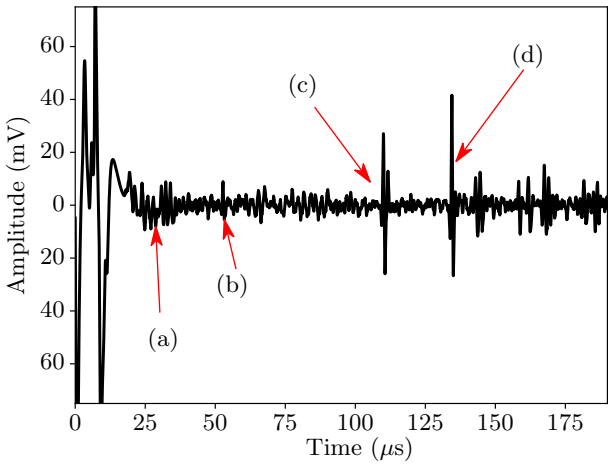

Figure 6.15: Pulse-echo A-scan data recorded on a 320 mm thick steel sample with a 6 mm diameter side-drilled hole at a depth of 160 mm (see figure 6.14). The received signals are interpreted as: (a), Rayleigh wave signals reflected from the sample edges at the surface, (b), back-scattered longitudinal wave from the defect, (c), reflected longitudinal wave from the sample's backwall, (d), reflected longitudinal wave from the back wall that has mode-converted at the defect and forward-scattered as a shear wave.

fit function to de-trend the low frequency generation noise from the signal. High frequency noise was then removed using a Butterworth bandpass filter between 0.1 and 3.5 MHz.

The total path length for path 1 in figure 6.14 is 314 mm and the longitudinal propagation speed is approximately 5950 ms^{-1}, which leads to a signal arrival time of 52.8 μs; signal b). in figure 6.15 therefore corresponds to a longitudinal wave that has back-scattered at the defect. Path 2 corresponds to a longitudinal pulse that is reflected off the sample's backwall as a longitudinal wave before mode-converting to a shear wave (S) (due to tangential components to the displacement vectors at the defect's interface) and scattering forwards from the defect. The total propagation distance of the longitudinal mode in path 2 is 477 mm, and the shear mode travels 163 mm at a propagation speed of approximately 3150 ms^{-1}. The sum of the propagation times for these two path components leads to a signal arrival time of 132 μs. Signal d) in figure 6.15 therefore corresponds to a forward-scattered, mode-converted shear wave.

The results of this experiment suggest that for detection of small defects, the largest indications are provided by forward-scattered mode-converted signals. Although the sample used in this experiment is not as-cast, the signals in figure

6.15 that constitute the defect indication have traveled through 640 mm of steel, and so the prospect of detecting internal defects in a 225 mm thick as-cast slab sample remains promising.

6.10 Conclusions

This chapter has discussed the development of a compact, low cost, high current four-channel phased array EMAT pulsing system that can drive coil-only generation devices at currents in the range of 1.75 kA. The channels of this pulser system have programmable phase delays with a temporal resolution of 2.5 ns, which allows for focusing and steering of the generated ultrasound beam. Experiments performed on large (225 mm thick), coarse grained, as-cast steel slab samples with rough surfaces demonstrate an enhancement of the transmitted signal by a factor of 3.5, and appropriate application of phase delays on three receiving elements can further improve the signal to noise ratio of a transmitted longitudinal signal by an additional factor of 1.9.

The EMAT phased array system presented in this chapter can deliver significant improvements in signal-to-noise ratio over the use of a single EMAT transducer. The ability to achieve high signal-to-noise ratio measurements in attenuative industrial cast steel samples using non-contacting sensors suitable for high-temperature application is a promising first step in the development of a measurement system that can be employed online during the continuous casting of steel for bulk and surface inspection of the slab. The experimental data presented here are supported by finite element calculations, indicating that such numerical simulation is appropriate for further development of the system.

Preliminary defect detection experiments have demonstrated that the high-power phased array system can be used to detect artificial void defects that are of similar size to the wavelength, although the highest-amplitude signals observed actually correspond to forward-scattered mode-converted shear waves instead of back-scattered longitudinal waves as is typical in a conventional pulse-echo arrangement. For measurement on as-cast samples, where signal amplitudes are expected to be lower due to poor surface condition and coarse grain structures, a transmission setup for detection of these mode-converted signals should be investigated. Although defect detection using the phased EMAT array has been demonstrated, further studies are required to demonstrate defect detection in as-cast samples, and in particular to demonstrate detection of real casting defects in industrial samples.

Chapter 7

Bulk Defect Detection

Chapter 6 detailed the development of an experimental high power phased EMAT array system capable of transmitting longitudinal ultrasound pulses through 225 mm thick as-cast industrial steel samples with a practicable signal-to-noise ratio, establishing a promising first step in developing a means of assessing internal cast product quality during the casting process. Section 6.9 demonstrated that the EMAT phased array system could be used in conjunction with a detection EMAT element for detecting a 6 mm diameter side-drilled hole defect in a 320 mm thick steel sample, but thus far, no demonstration of defect detection in thick, as-cast steel samples has been presented.

This chapter follows from the preliminary defect detection investigations presented in chapter 6 by outlining methods of bulk defect detection in as-cast steel samples that are potentially applicable during the casting process.

7.1 Image Reconstruction Using Mode Converted Shear Waves

As discussed in section 6.9, the largest observed signal amplitudes in a pseudo pulse-echo experiment, performed using a high powered EMAT array generation source and an adjacent EMAT detection sensor, correspond to shear waves that have mode-converted and forward-scattered at the defect, rather than back-reflected longitudinal waves, as is typical in conventional pulse-echo tests. It is therefore advantageous to mitigate attenuation losses in this mode-converted signal by reducing the path length and detecting the forward-scattered shear waves on the side of the test piece directly opposite the generation array.

Also discussed in chapter 6, in section 6.8, was the concept of an array of detection sensors to improve the signal to noise ratio of ultrasound pulses transmit-

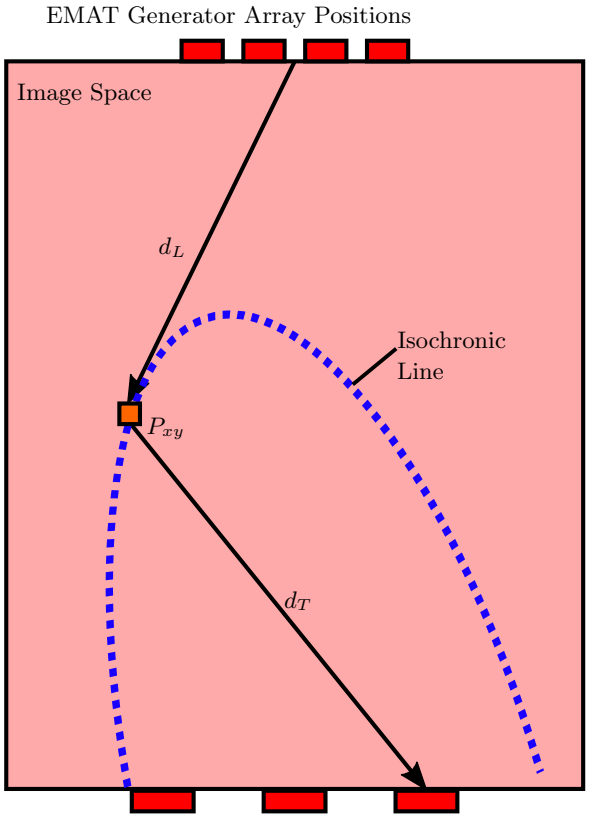

Figure 7.1: Schematic diagram describing the mode conversion image reconstruction method. The brightness of a pixel in the image space, P_{xy}, is found by computing the time of flight of a signal that propagates through a distance d_L as a longitudinal wave and d_T as a shear wave. The image reconstruction algorithm produces isochronic lines for A-scan signals, which are summed over to produce an image.

ted through the cast. Coherent addition of the transmitted pulses was shown to be equivalent to the concept of coherent averaging, with the signal-to-noise ratio of the signal, as measured by the ratio of the root mean square amplitude of signal and noise bins in the A-scan data, improving by a factor of $\sqrt{N}$, where N is the number of detection elements used. In section 6.8, phase matching was achieved by the cross-correlation of signals from three detection elements to determine the relative phase lags between signals of interest. The calculated phase lags were then applied to the data before summation, improving the SNR by a factor of 1.9. This approach was appropriate for the case in section 6.8, since the sample used was free from defects, and hence the only signal in the A-scan data corresponds to direct transmission of a longitudinal wave pulse. For the purposes of defect detection, *a-priori* knowledge of the defect distribution cannot be presumed, and hence neither can the arrival time interval for defect indication signals. A general approach to defect indication enhancement must therefore be considered.

The proposed method is to perform an image reconstruction, so that the enhanced defect indications in a two-dimensional image space remain distinct. This method has the advantage of providing spatial information about the defect's location and extent. Instead of cross-correlating signals to determine the phase separation between the defect indication signals in isolation, the sum of the signals can be calculated for all values of phase separation, and those phase lag values can be associated with a physical location in an image space. By summing the signals measured by an array of detection elements in this way, it is possible to reconstruct an ultrasound image of the sample's bulk using a variation of the synthetic aperture focusing technique (SAFT) [119, 118, 120, 168]. A SAFT algorithm is chosen here instead of a more-conventional total focusing method approach because the sample is large and attenuative, and the limited acoustic power of a TFM approach results in a low SNR [169].

The steps in the proposed image reconstruction algorithm are as follows; firstly, the analytic envelope profile for each detected signal is obtained by calculating the absolute value of the signal's Hilbert transform [118]. An image space is then defined by selecting appropriate dimensions to describe the sample cross section and defining a uniform square grid with the desired pixel density. The pixels in the image space are then iterated over to calculate the propagation time of a longitudinal wave from the centre of the generation array to the pixel's location, and summed with the propagation time of a mode-converted shear wave from the pixel's location to the appropriate detection position (see figure 7.1). The total propagation time gives the phase lag corresponding to a given combination of pixel and detection element

position. The analytic signal amplitude for the corresponding array element at the corresponding time interval is added to the pixel brightness value, P_{xy}, at this image space position (denoted by subscript xy, corresponding to the x and y coordinates in the image space). Once the entire image space has been iterated over for a given detection element position, the process is repeated for each other detection element positions.

Mathematically, the pixel brightness value for a given position in the image space, P_{xy}, can be expressed as the sum:

$$P_{xy} = \sum_i \left| \hat{A}\left(t^i_{xy}\right) \right|, \tag{7.1}$$

where $\hat{A}$ denotes the Hilbert transform of the signal A, the superscript i refers to the ith element in the detection array and t^i_{xy} is the propagation time of a signal (that has undergone a mode conversion at image space position x, y) from the generation array to the ith detection element. t^i_{xy} can therefore be calculated as:

$$t^i_{xy} = \frac{\sqrt{(x_g - x_p)^2 + \left(y^i_g - y_p\right)^2}}{c_L} + \frac{\sqrt{\left(x^i_P - x_d\right)^2 + \left(y^i_p - y_d\right)^2}}{c_T}, \tag{7.2}$$

where x_g and y_g are the x and y coordinates of the centre of the generation array respectively, x_p and y_p are the x and y coordinates of the pixel corresponding to the subscripts xy, x_d and y_d are the x and y coordinates of the i^{th} element of the detection array respectively.

This method is conceptually similar to the cross correlation method outlined in section 6.8, in that the signals are delayed relative to each other and summed to enhance signal amplitudes, but the maximised signal response is projected into an image space, and the maximal response therefore corresponds to the defect's location. This method therefore enables detection of a defect and provides information about the extent and position of the defect within the image space.

7.1.1 Finite Element Analysis for Mode Conversion Image Reconstruction

To verify the proposed mode-converted shear wave image reconstruction method, time domain finite element analysis was used to calculate the expected signals recorded by the elements of the detection array in a transmission experiment (see figure 7.2). Each generation element was modeled as a uniform piston source as described in section 6.4.1. The pressure load function was the square of a half-cycle of a sine wave with a period of 2.0 μs and an amplitude of 40 MPa, since this was

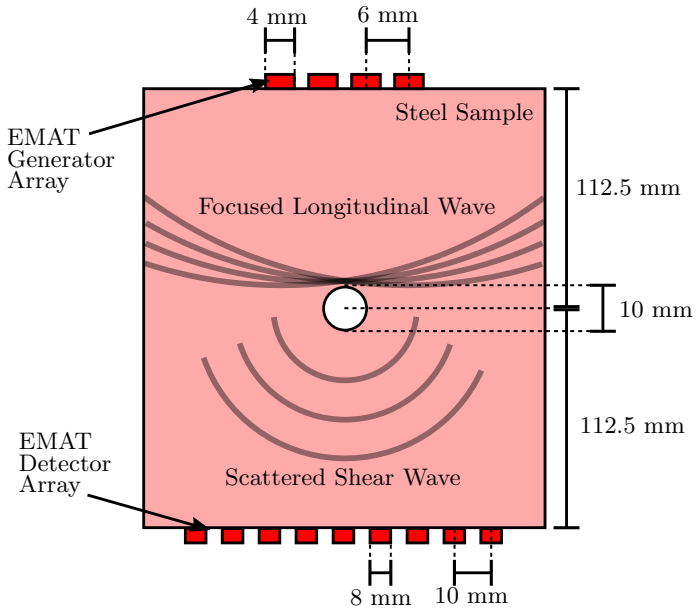

Figure 7.2: Schematic diagram of the finite element model used for verification of the mode conversion image reconstruction algorithm. The elements of the generation and detection arrays were modeled as described in chapter 6.

shown in section 5.4 to approximate the temporal pressure profile applied by the pulsing circuit. A finite element grid was meshed with a density of 16 elements per wavelength, where the wavelength corresponds to the wavelength of a bulk shear wave with a frequency of 2.0 MHz. The bulk shear speed in steel is 3150 ms^{-1}, giving an element size of 0.1 mm. The model was meshed uniformly with simple linear quadrilateral elements, and a maximum time step of 17 ns was chosen, since this corresponds to half of the propagation time of a longitudinal acoustic wave across an element of width 0.1 mm.

The model was constructed such that a 10 mm diameter circular hole was modelled as a region of void in at a depth of 112.5 mm in a 225 mm thick steel sample (see figure 7.2). Phase delays were calculated in accordance with equation 6.1 and applied to nodes representing the elements of an EMAT generation array to focus an incident longitudinal ultrasound pulse at a depth of 160 mm, such that the maximum sound intensity would be in the region of the defect.

A detection array was modeled by summing the appropriate surface node velocity histories corresponding to the footprint of a nine-element detection EMAT array, where each individual EMAT element has a footprint described by figure 6.9. The modeled detection array consisted of 9 detection elements arranged linearly, and centred beneath the generation array and the defect, with a lateral separation

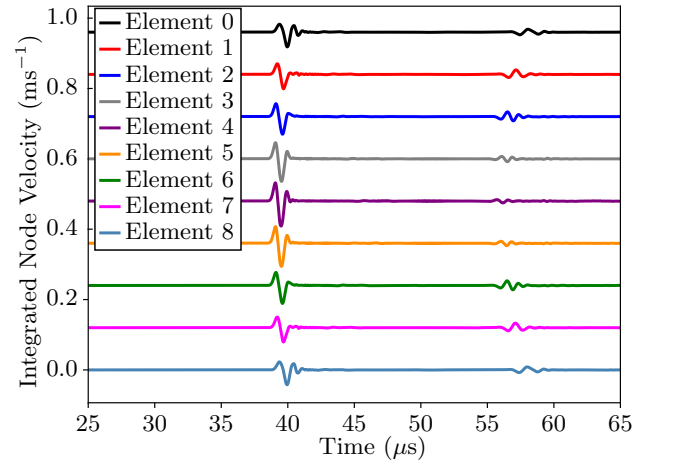

(a)

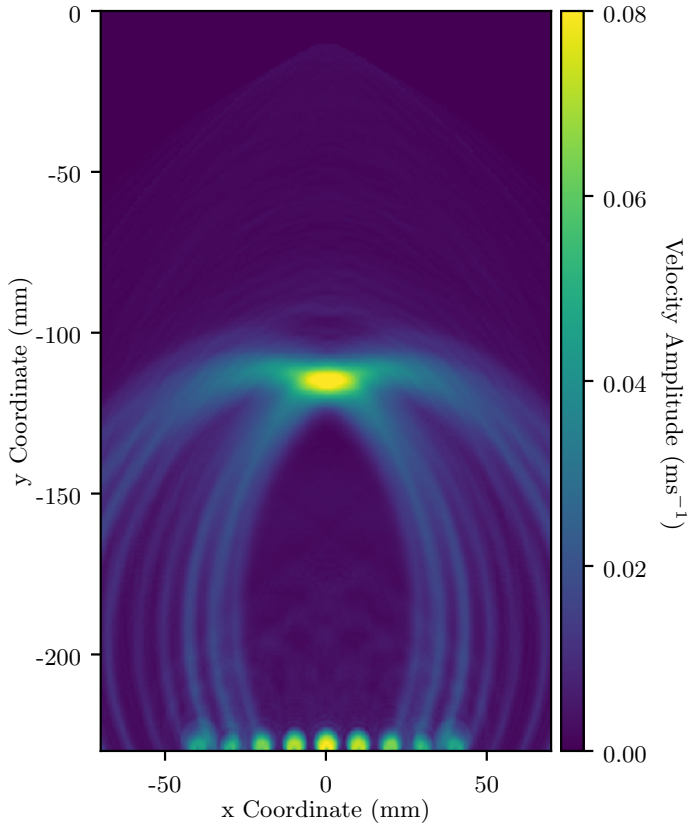

(b)

Figure 7.3: Figure 7.3a shows the A-scan data calculated using the finite element model outlined in figure 7.2, figure 7.3b shows an image reconstructed using this data using equation 7.1.

between elements of 10 mm (as described in figure 7.2). The calculated A-scan data from this model are shown in figure 7.3a. In each case, the incident focused longitudinal wave pulse arrives at each detection element in a time interval from 38.5 - 38.8 μs, and a mode-converted shear wave arrival is seen between 55 and 56.5 μs, corresponding to a shear wave that has forward-scattered from the defect.

Equation 7.1 was applied to the A-scan data in figure 7.3a to reconstruct an image of the sample's interior. The effect of the reconstruction algorithm is to project into the image space a series of loci for each detection element, which correspond to the isochronic lines associated with the arrival of signals in the A-scan data depicted in figure 7.3a. Coincidence of these loci leads to coherent summation of the defect indication signal at the associated region in the image space, and hence the defect's position is associated with the position of the brightest parts of the image. In figure 7.3b, the bright region is located on the central axis at a vertical position of approximately 115 mm, which corresponds to the position of the void defect in the finite element model (shown in figure 7.2), hence validating the proposed image reconstruction algorithm for both detecting and locating internal void defects.

A nine element detection array was modelled above to demonstrate the principle of the image reconstruction using mode-converted shear waves, but construction of a nine-element array for experimental verification of the method is difficult, due to the requirement for multiplexing to record simultaneous A-scan data from nine independent detection elements. The experimental verification presented in the following section is therefore performed using a three-element detection array, and hence for comparison, it is necessary to compute a reconstructed image using only three detection elements.

Experimental demonstration of the reconstruction algorithm also requires the use of a processed steel sample, with smooth surfaces and without the coarse, anisotropic grain structures present in as-cast samples. The sample available for study has a depth of 320 mm and a side-drilled hole with a 6 mm diameter at a depth of 160 mm. The image reconstruction process was repeated for a model with these dimensions, with A-scan data obtained from this model for detection elements at - 30, 0 and 30 mm offsets from the centre of the model (the model geometry matched the schematic diagram of the experimental setup shown in figure 7.6). The calculated A-scan data from this model is shown in figure 7.4a, and the reconstructed image is shown in figure 7.4b.

It is interesting to note that there appear to be independent scattered signals in figure 7.4a, which are scattered from both the upper and lower surfaces of the

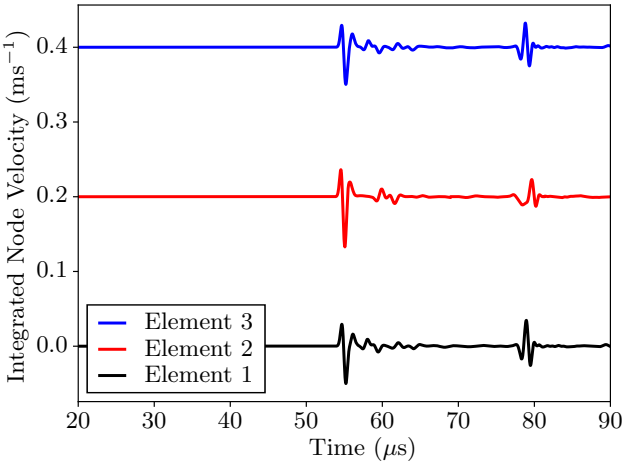

(a)

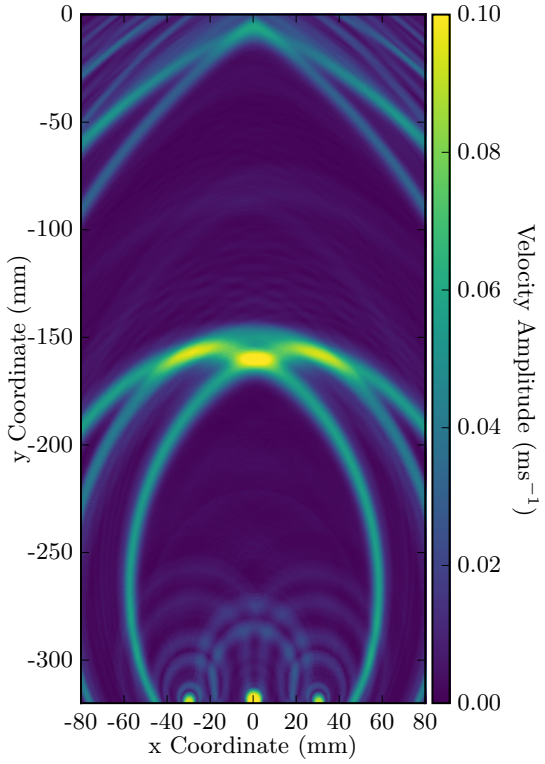

(b)

Figure 7.4: Figure 7.4a shows the A-scan data recorded for a finite element model similar to that shown in figure 7.2, but with a central hole defect of diameter 6 mm, and detection array elements placed at -30, 0 and 30 mm lateral offsets from the centre of the generation array. Figure 7.4b shows an image reconstructed with this A-scan data, using equation 7.1.

defect. The signals arriving at the outer detection elements from the central void arrive 1 μs earlier than the signal arriving at the central element, which can be accounted for when considering an additional 6 mm of path length for a signal scattered at the upper surface of the defect and detected on the central element, compared to signals scattered from the lower surface being detected at the outer elements. This leads to coincidence of the isochronic lines from the outer elements at the position of the defect's lower surface and further coincidence of these lines with the isochronic line from the central element occurring either side of this central position, producing the characteristic shape illustrated in figure 7.4b. Hence, the region in the centre of this shape (above the central bright spot and between the two lobes either side of it) corresponds to the region between the upper and lower scattering surfaces and therefore the defect's position. This feature is present in figure 7.3b also, but not immediately apparent, because the use of nine detection elements, most of which are laterally displaced from the defect, leads to most signal coincidence corresponding to the bottom of the defect and making the signal from the upper surface of the defect less well-defined.

Although the intensity distribution shown in figure 7.4b is harder to interpret than the reconstruction performed with a greater number of elements in the detection array, the size and position of the defect is indicated by the coincidence of the loci in the image, and there is a clear indication that can be directly and quantitatively compared to experimental data.

7.1.2 Experimental Validation

Experimental Array Centering

The delay-and-sum method described by equation 7.1 relies on good knowledge of the relative positions of the generation and detection elements in the respective arrays. In practice it is difficult to know the lateral displacement of the detection array relative to the generation array precisely, since each array is on the opposing side of a large steel sample with rough surfaces. Through careful measurement of the arrival times of transmitted longitudinal signals at the generation array elements, it is possible to know this lateral displacement independently of the material properties of the transmission medium (assuming that the wave propagation speed is constant).

The lateral displacement of an array element x_i from the centre of the generation array can be expressed as a function of the longitudinal propagation speed c, the depth of the sample y and the arrival time of the transmitted longitudinal

pulse at that array element, t_i;

$$x_i = \sqrt{c^2 t_i^2 - y^2}. \tag{7.3}$$

The distances between the elements of the detection array are well known; this is a parameter that can be controlled to a high precision in experiments, since the array elements are wound into a 3D-printed plastic template. The lateral displacement of each element can therefore be expressed in terms of the lateral displacement of the first array element;

$$x_{i+n} = x_i + np, \tag{7.4}$$

where n is an integer denoting the n^{th} consecutive element away from the element of interest, i, at position x_i, and p is the inter-elemental distance. Using equations 7.3 and 7.4, a series of simultaneous equations can be written for the lateral displacements of all detection elements in terms of the lateral displacement of the first array element, x_1. In the case of the experiments described here, there are three detection elements, and hence three simultaneous equations and two unknown quantities (the lateral displacement x_1 and the longitudinal wavespeed). Solving this set of equations for x_1, and eliminating the wave speed, c, yields the following result:

$$x_1 = p\frac{4\left(t_1^2 - t_2^2\right) - \left(t_1^2 - t_3^2\right)}{2\left(t_1^2 - t_3^2\right) - 4\left(t_1^2 - t_2^2\right)}. \tag{7.5}$$

Equation 7.5 can be used to find the lateral displacement of the first element in the detection array (and therefore all other elements, through the use of equation 7.4) independently of the wavespeed, so no careful calibration measurements need to be taken. Furthermore, it is a function only of the detection element separation (which is a well-known and controllable quantity) and of the difference in arrival times of the transmitted pulse at the array elements, which can be found accurately by cross-correlating the appropriate section of the recorded A-scans to determine the signal phase delays between each element.

To verify this method of determining the lateral offset between the generation and detection array, data were generated by finite element calculations, as described in section 7.1, for a range of detection array lateral displacement values. For each displacement value, the A-scan data calculated from the array's central element were windowed between 37 and 45 μs to isolate the directly-transmitted longitudinal wave signal, for use as a reference function for cross-correlating with A-scan data from other detection element positions. A-scans were then recorded for a three-element detection array, with a 30 mm lateral separation between adjacent elements, over

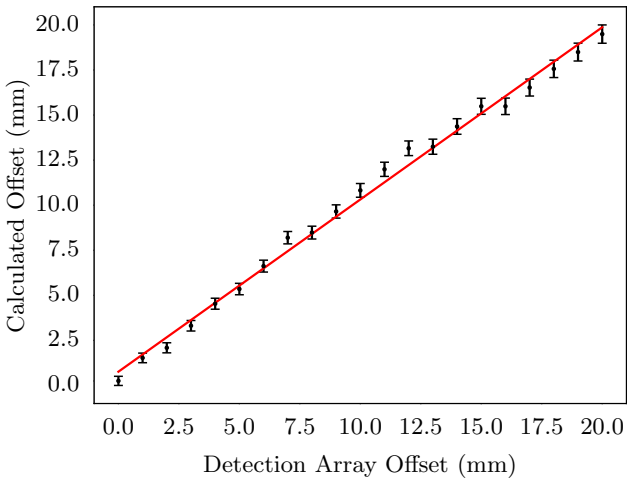

Figure 7.5: A plot of the detection array offset calculated using equation 7.5 against the offset used in the finite element models. The gradient of the linear fit is (0.94 ± 0.02).

a range of offsets from -20 to 20 mm, and the pulse arrival times, t_1, t_2 and t_3 were determined by cross correlation of the reference signal with the A-scan data. Uncertainties in the pulse arrival time were estimated from the mean fractional change in the distance between successive maxima in the pulse, caused by distortion of the pulse due to non-normal incidence angles for detection elements away from normal incidence. The lateral offset was calculated in each case using equation 7.5, and plotted against the real offset (see figure 7.5). The linear fit suggests that this method can reproduce the relative lateral displacement of the detection array to an accuracy of approximately 5%, relative to the known displacement of the detection array; the deviation from the linear fit is likely due to the distortion of the longitudinal pulse shape as the detection elements are moved from the centre, which introduces errors when using cross-correlation to determine the difference in arrival time of the longitudinal pulse at the array's detection elements. Over a range of lateral displacement values from 0 to 20 mm, however, the maximum deviation of the calculated lateral offset is approximately 1 mm, which is approximately the precision limit for manual manipulation of an experimental detection array, and hence this method was deemed suitable for aligning the generation and detection array elements in the following experimental section.

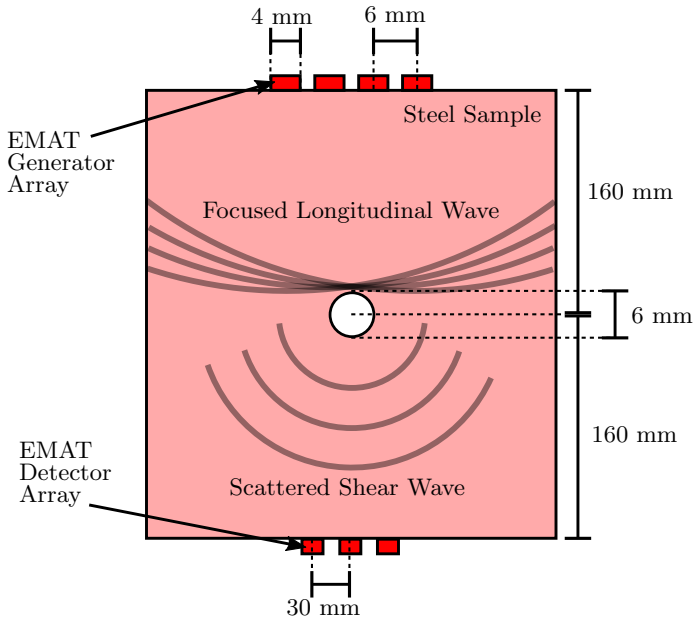

Figure 7.6: Schematic diagram of the experiment used to verify the mode-conversion imaging technique presented in section 7.1.

Experimental Mode Conversion Image Reconstruction

Experimental validation of the image reconstruction, demonstrated using the finite element data presented in section 7.1.1, was attempted using a four-element EMAT phased generation array (as described in figure 6.10) and a three-element detection array (the individual elements comprising this array were constructed as depicted in figure 6.9), with a lateral spacing of 30 mm between the centre points of each element. The array centering method from section 7.1.2 was used to ensure there was no lateral offset between the centre of the generation and detection arrays. The test piece was a 320 mm thick steel sample with a 6 mm diameter side-drilled hole through the centre (see figure 7.6). As was demonstrated in the simulated A-scan data (see figure 7.4a), the appearance of a mode-converted shear wave signal in the A-scan provides the defect indication, with the arrival time of this signal related to the defect's position in the sample. The recorded A-scan data were used to reconstruct an image of the sample's cross section using equation 7.1. The shape and position of the resulting image pattern matches the simulated image reconstruction for the case of three detection elements (see figure 7.4b), with a central indication corresponding to shear waves that have scattered from the lower surface of the defect, and the two bright regions either side of the defect's location resulting from the coincidence of signals from the upper and lower defect surfaces.

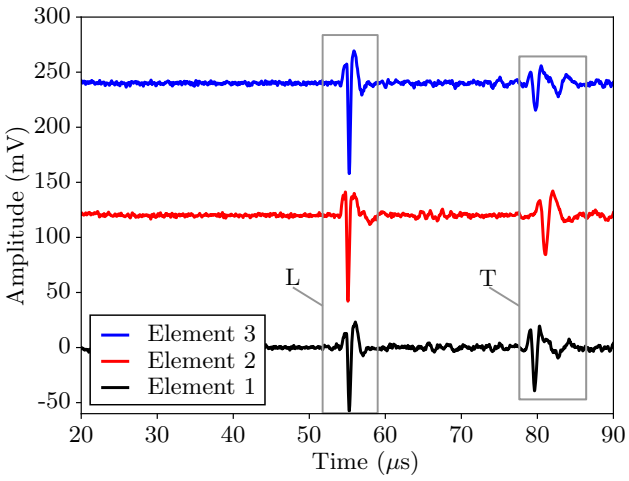

(a)

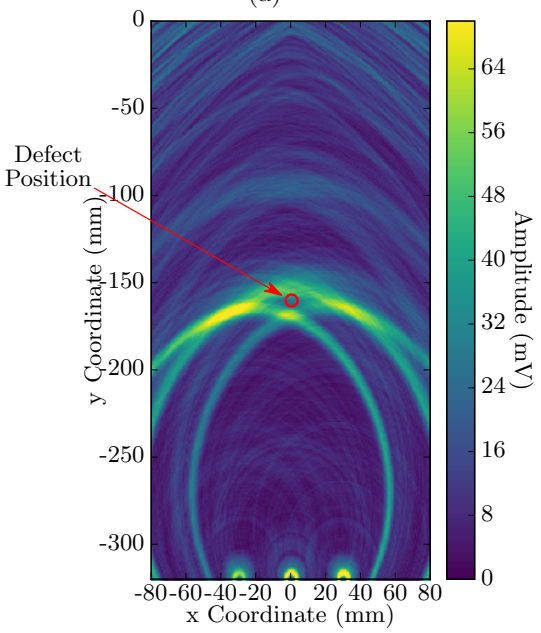

(b)

Figure 7.7: Figure 7.7a shows the experiment A-scan data recorded on the 320 mm thick steel sample with a 6 mm side-drilled hole at a depth of 160 mm. The signals L and T correspond to directly-transmitted longitudinal waves and mode-converted shear wave defect indications respectively. Figure 7.7b shows the image reconstructed using this A-scan data and equation 7.1.

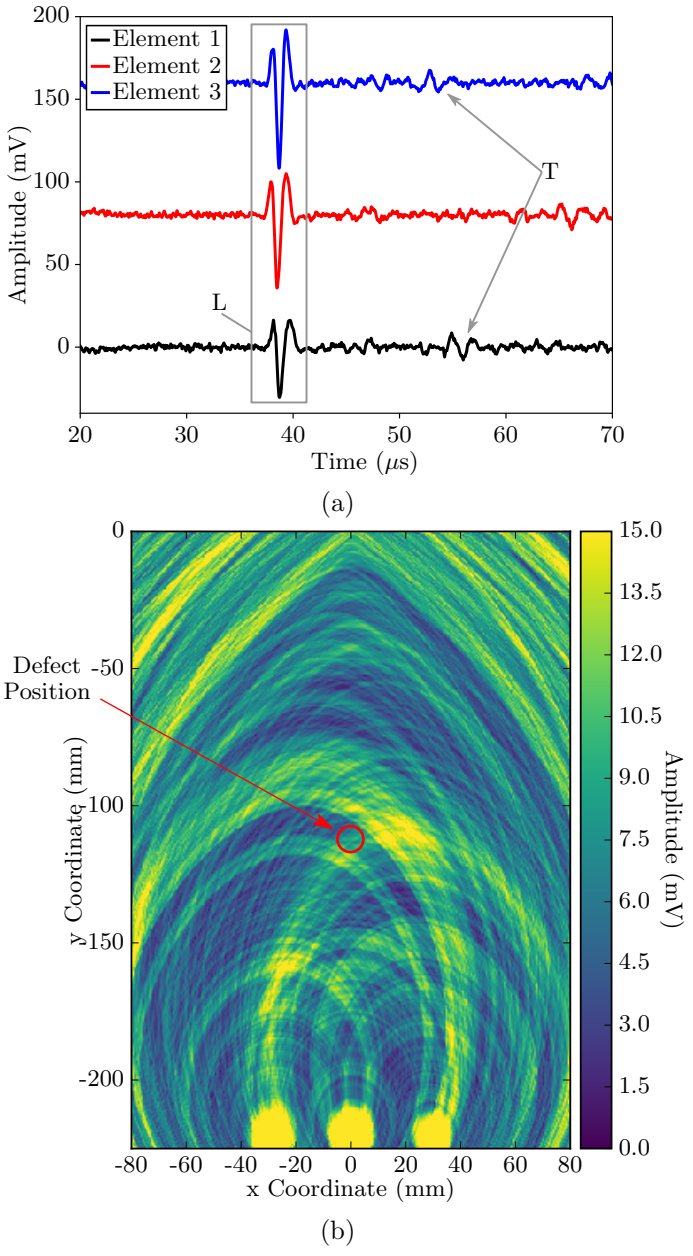

Figure 7.8: Figure 7.8a shows the experiment A-scan data recorded on the 225 mm thick as-cast industrial steel slab sample with a 10 mm side-drilled hole at a depth of 112 mm. L and T correspond to directly-transmitted longitudinal waves and mode-converted shear wave defect indications respectively. Figure 7.8b shows the image reconstructed using this A-scan data and equation 7.1.

The presence of shear waves scattered from both the upper and lower surfaces of the defect allow the approximate determination of the defect's extent from the region of low amplitude located between the areas of constructive signal interference. This is in excellent agreement with the finite element simulation results shown in figure 7.4b, and demonstrates that the phased array system described in section 6.7 can be used to detect and locate defects in thick steel samples with a practicable signal-to-noise ratio. The simulated image reconstruction performed with A-scans corresponding to a nine-element detection array demonstrates that the reconstructed image quality can be improved through the use of more detection elements, although, since this is a demonstration of the concept, this is not shown here due to the complexity of constructing a nine-element detection array.

The sample used to reconstruct the image in figure 7.7b is not a cast sample, so although it is much thicker than a cast slab (320 mm, compared to a 225 mm thick cast slab), its smooth surfaces and finer grain structures are not representative of industrial as-cast samples. An as-cast industrial steel sample of thickness 225 mm with a 10 mm diameter hole at a depth of 110 mm was also available for experimental study (the sample geometry matched that shown in the schematic diagram of the finite element model shown in figure 7.2). Figure 7.8a shows the data obtained when performing the same experimental procedure as outlined above on the cast steel sample; a defect indication is observable at approximately 55 μs in the A-scan data for elements 1 and 3, but the signal-to-noise ratio is too low to allow for reliable defect identification and location. As discussed in section 1.2.3, grain structures in cast steel slabs can be of order 10 mm in size. The relative size of the grain structures in the material to the size of the defects of interest places a physical limit on the defect sizes that can be reliably detected, and the resulting image reconstruction (see figure 7.8b) therefore contains several artefacts corresponding to grain boundary reflections that are of similar intensity to the defect indication. Reliable detection and defect sizing from this image is therefore not possible. Nonetheless, a signal associated with a 10 mm defect in the centre of the case slab is present at 55 μs in the A-scan data, which itself is a significant result considering these measurements were performed on an industrial sample using non-contacting sensors. That the 10 mm defect in the sample used to generate the data in figure 7.8b is not easily distinguishable above the background noise due to grain scattering suggests that the system is incapable of reliably detecting defects of this size.

(a) (b)

Figure 7.9: Photographs of defective steel slab samples. Figure 7.9a shows a slab sample where severe internal cracks have propagated to the casting surface, and exist through the full thickness of the cast (outlined in yellow). Figure 7.9b is a sample cut from the same slab as the sample in figure 7.9a, but no defects are apparent on the sample's surface.

7.2 Vertical Crack Detection

The artificial side-drilled hole defects described in section 7.1.2 are not representative of genuine casting defects, because they are smooth-sided and cylindrical, which means acoustic waves scattered from these defects will be easily-detectable over a range of angles and have relatively high amplitudes compared to waves that have scattered from a rough-surfaced defect. Real defects are likely to be more irregular in shape, and hence there is merit in attempting to measure real casting defects to establish the usefulness of the transmission system.

As discussed in section 1.2.2, internal casting defects can range in size from pores and inclusions of several mm to large cracks of several cm in length. The results of section 7.1 suggest that smaller casting defects of order 10 mm in size are not readily measurable using the EMAT transmission system. Large cracking defects, however, may be more reliably detectable if the ratio of the defect's characteristic size to the ultrasound wavelength is larger [19]. Internal cracks consist of planar voids that align with their long dimension in the vertical direction in a cast slab; they may be up to several cm in length, are typically only 1-2 mm in width and may either lie completely within the cast or may break the surface. Methods have been previously reported concerning the detection and measurement of surface-breaking cracking defects during the continuous casting process [74, 11, 108], but to date, no methods have been reported for the detection of internal cracking defects.

For this study, steel slab samples containing genuine, severe internal cracking defects were procured from Tata Steel's IJmuiden steel casting site. As with previous non-defective samples, these samples are 225 mm thick, and are as-cast, so their surfaces are rough and feature oscillation marks and oxide scale. The slab from which these samples were cut is the result of a casting run in which incorrect parameters lead to the development of transverse crack defects during the cooling stage; a photograph of two samples cut from this slab is shown in figure 7.9. In one sample, the internal cracks break the surface, and are readily visible. The second sample is cut from the same defective slab, but contains no visible signs of cracking at the surface, although, given the severity of the cracking exhibited by the slab, it is likely to contain vertical cracking defects contained entirely within the sample's bulk. This section concerns the development of a potential detection method for these defects using the EMAT phased array system described in chapter 6.

7.2.1 Phased Array Imaging of Cracking Defects

To design an EMAT-based test of internal slab quality sensitive to the kind of internal cracking seen in the samples shown in figure 7.9, it is helpful to characterise the defects to establish approximate values for the size and depth of the internal cracks. In the sample with the full-thickness crack shown in figure 7.9a, it is clear that the defect extends through the full thickness of the cast, has a width of approximately 2 mm, is transverse to the casting direction and is vertical (with the crack's long axis normal to the casting surface). In this case, the defect is readily detected on the slab's surface, and could easily be identified using a visual detection method, or using previously-reported ultrasonic measurement systems for detecting surface-breaking cracks during steel casting. The second sample (in figure 7.9b) contains no defects that break the slab surface, and so it is not immediately apparent that the slab is in fact defective. This sample is nevertheless likely to contain severe internal cracking defects, since it was cut from the same slab as the sample containing surface-breaking cracks. There is therefore motivation to develop a means to detect these defects (if they exist) using a system suitable for online measurement.

To establish whether these defects are present, and to determine more about their size and distribution, ultrasonic phased array imaging was performed, since this is sensitive to void-type defects in the bulk and also yields spatial information from the image reconstruction. The total focusing method, as described in section 3.7.1, has been described as the 'gold standard' of ultrasonic phased array imaging and defect characterisation [170], and so was the chosen method for imaging the bulk of these samples.

The full matrix capture data used for the image reconstruction was recorded using a 256 channel Peak NDT Micropulse 5 phased array controller with a 64 element, 5 MHz piezoelectric transducer array with element widths of 0.6 mm. An excitation voltage of 200 V, with pulse width 200 ns was applied to each element to generate large amplitude, broadband acoustic wave pulses to ensure sufficient penetration through the attenuative sample. The recorded data were filtered using a Butterworth digital bandpass filter with cutoff frequencies of 0.2 and 7 MHz, before a total focusing method (TFM) image reconstruction was performed according to the algorithm described in section 3.7.1.

In the first attempt to image internal defects in the cast slab sample shown in figure 7.9b, the phased array transducer was placed on the upper casting surface, such that the image plane was transverse to the casting direction and hence parallel to the plane in which the internal cracks are likely to lie, as shown in figure 7.10a. The reconstructed image from this data acquisition is shown in figure 7.10b. There are no features in the reconstructed image that are suggestive of large, internal void defects; the variations in pixel brightness are likely due to coherent noise resulting from scattering from grain structures in the cast slab. There is also no visible feature corresponding to reflections from the sample's lower surface at 225 mm, suggesting that attenuation due to grain structures (and the possible presence of internal crack defects) is severely reducing the amplitude of the reflected signal, making it hard to distinguish above noise due to scattering from grain structures.

In the geometry described by figure 7.10a, the long axis of the crack is not exposed to the incident ultrasound beam, and hence sensitivity is relatively low. Because these samples have been cut from the slab, the cast's cross-section is exposed and hence there is access to a surface that lies parallel to the plane in which the defects are likely to lie. Imaging performed from this surface therefore presents a greater possibility of detecting those defects, although this setup could not be transferred to an online test. A second FMC data acquisition was therefore performed with the TFM image plane perpendicular to the defect plane, with the phased array transducer positioned on the sample as shown in figure 7.11a. The image region was chosen such that it overlapped the image region displayed in figure 7.10a. The reconstructed TFM image is shown in figure 7.11b, and displays a defect indication at a depth of 90 mm, with an approximate lateral dimension of 40-50 mm. Other internal defects may exist beneath the one shown, but these would be shadowed by the upper defect, and more difficult to detect due to grain noise.

The reconstructed image in figure 7.11b does not give a clear overview of the size, position and distribution of vertical cracking defects in the sample, but it does

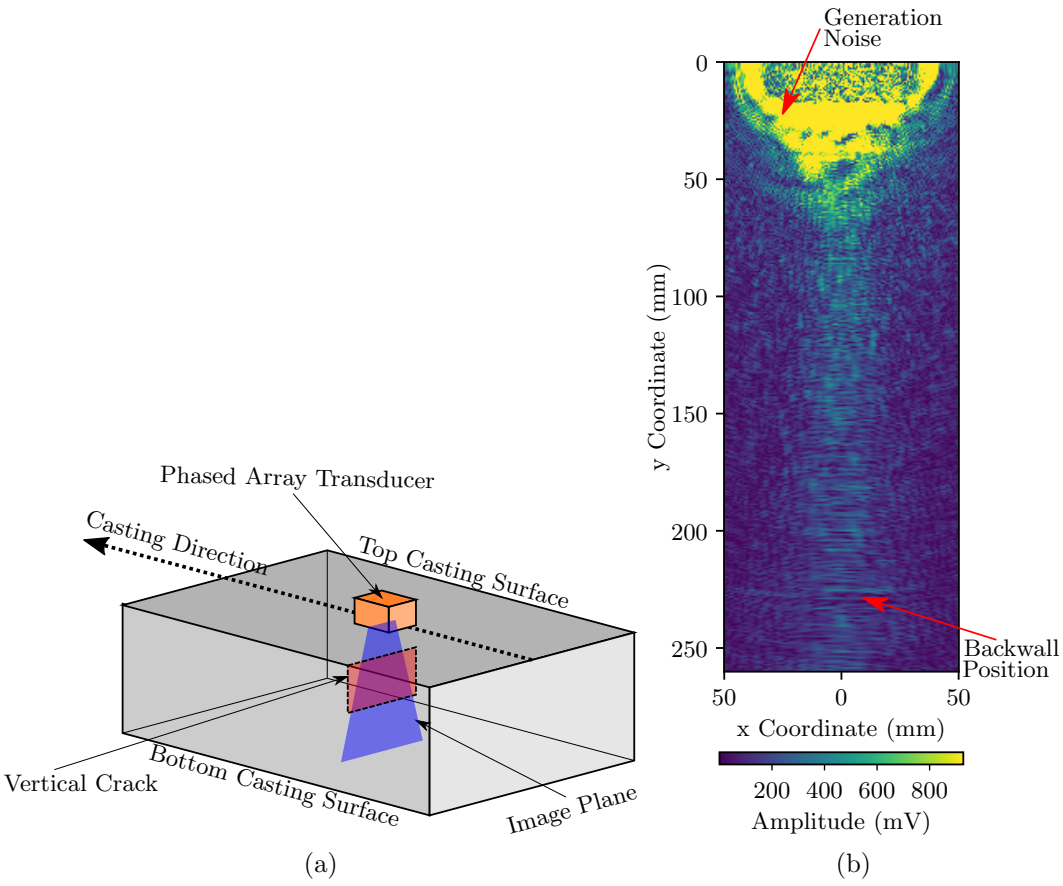

Figure 7.10: Figure 7.10a shows the relative orientation of the sample from figure 7.9b and the image plane used to generate the TFM image shown in figure 7.10b.

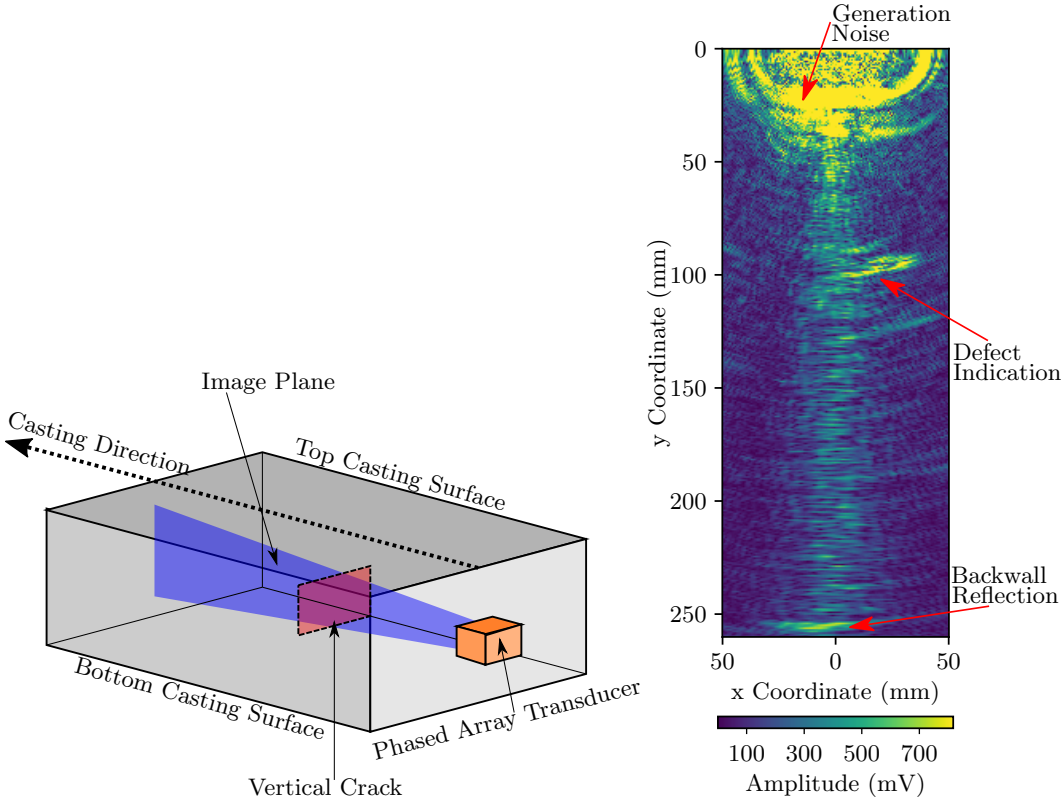

Figure 7.11: Figure 7.11a shows the relative orientation of the cracked sample and the image plane used to generate the TFM image shown in figure 7.11b.

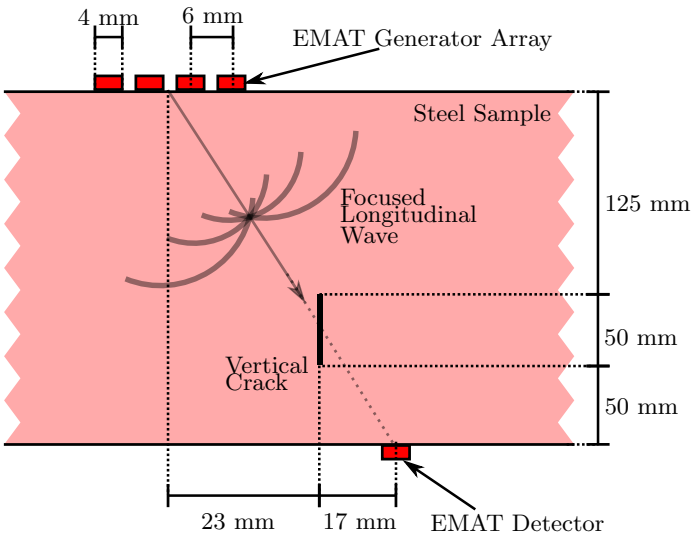

Figure 7.12: Schematic diagram of the finite element model used to investigate the proposed angle transmission experiment for vertical crack detection.

show that the defects are indeed present, that they can be several cm long, that they are aligned transverse to the casting surface, as suspected, and that they are buried several cm beneath the casting surface.

7.2.2 Finite Element Analysis for Vertical Crack Detection

The images in section 7.2.1 suggest that vertical cracking defects are present in the sample shown in figure 7.9b, and that they are more easily-detected when the long axis of the crack is exposed to the incident ultrasound beam. To help improve the sensitivity of an EMAT-based transmission detection experiment, a testing mode is therefore proposed in which the beam steering properties of the EMAT phased array are used to direct incident acoustic wave pulses into the test piece at an angle away from normal. With angled incidence, the long axis of the crack would be exposed to the incident pulse to improve defect sensitivity, with the transmitted pulse, modified by interaction with the crack, detected by an EMAT detection sensor placed offset on the opposing side of the slab (see figure 7.12).

A finite element model was constructed to determine the expected signal response of this arrangement. A four-element EMAT generation array was modeled (as described in chapter 6) on the surface of a 225 mm thick region of steel, a detection EMAT was modeled on the opposing side, with a lateral offset of 40 mm. A crack of length 50 mm and width of 0.5 mm was modeled as a region of void, with the centre of the crack located at a depth of 150 mm and a lateral offset from the centre of the generation array of 230 mm (see figure 7.12). Phase delays of 0.53, 0.38,

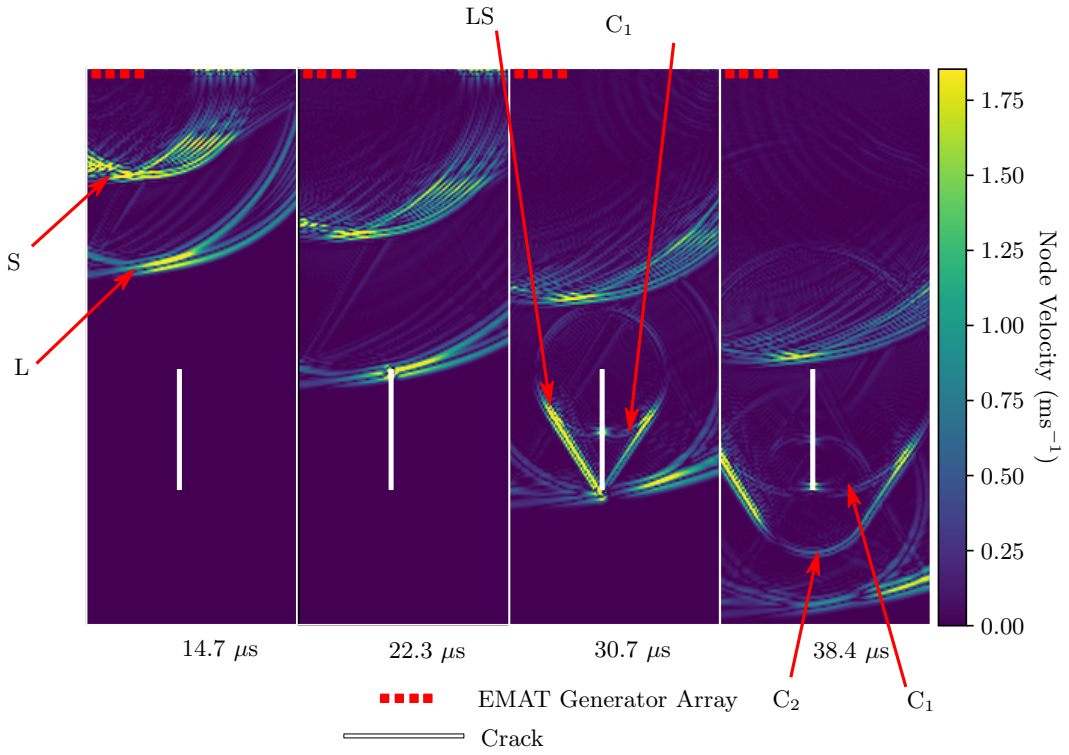

Figure 7.13: A series of node velocity plots for the finite element model outlined in figure 7.12, with the simulation run time in each case shown below the corresponding image. L and S denote incident longitudinal and shear waves respectively, LS shows a mode-converted wave reflected from the crack defect, and C_1 and C_2 denote mode-converted waves scattered from the lower and upper crack surfaces respectively.

0.20 and 0.0 μs were applied to the respective generation elements from left to right, in order to focus the ultrasound beam at detector, and so send incident ultrasound wave in at an angle to expose long axis of the crack to the beam. The elements were meshed with a density of 16 elements per wavelength, where the wavelength corresponds to the wavelength of a bulk shear wave with a frequency of 2.0 MHz, giving an element size of 0.1 mm. The model was meshed uniformly with simple linear quadrilateral elements, and a maximum time step of 17 ns was chosen, since this corresponds to half of the propagation time of a longitudinal acoustic wave across an element of width 0.1 mm.

A series of images showing the node velocity magnitude of the model at different times since the beginning of the excitation pulse are shown in figure 7.13. The image progression shows the incident focused wave pulse steered at an angle of 80° interacting with the vertical crack defect. A mode-converted shear wave is excited as the incident pulse encounters the upper crack tip, and again as the pulse

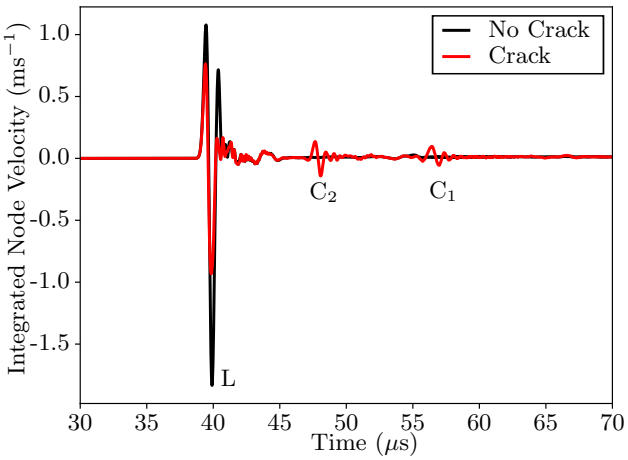

Figure 7.14: A-scan data obtained from the finite element model outlined in figure 7.12 for the case where a crack is and is not present. l, c_1 and C_2 correspond to the wave modes shown in figure 7.13

encounters the lower crack tip. On the opposing surface, the order of signal arrival corresponds to the incident longitudinal wave pulse, followed by the mode-converted wave from the lower crack tip, and then later by the mode-converted wave from the upper crack tip. The calculated A-scan corresponding to the node velocity history integrated over the profile of a detection coil is shown in figure 7.14, alongside an A-scan calculated for a model in which the crack is absent.

There are three features that correspond to a defect indication in the calculated A-scan data. The two mode-converted shear wave indications, shown in the image progression in figure 7.13, appear with arrival times of 47 and 55 μs, corresponding to mode conversions at the lower and upper crack tips respectively. These are not present in the A-scan calculated in the case where the crack is absent, and so the appearance of these spurious signals that arrive after the main pulse are indicative of a scattering object in the bulk material. The third indication is a reduction in the amplitude of the transmitted signal. As seen in figure 7.13, a fraction of the incident longitudinal pulse is reflected from the crack away from the detector, thus reducing the amplitude of the signal that is transmitted towards the detector.

The model outlined in figures 7.12 and 7.13 is relatively simple, in that there is a single, straight crack with smooth edges between the generation array and the detector. The TFM image of the real defect shown in figure 7.11b suggests that real casting defects are likely to have rough surfaces and may be shaped irregularly. The scattering of the focused ultrasonic wave off the real casting defect is therefore likely

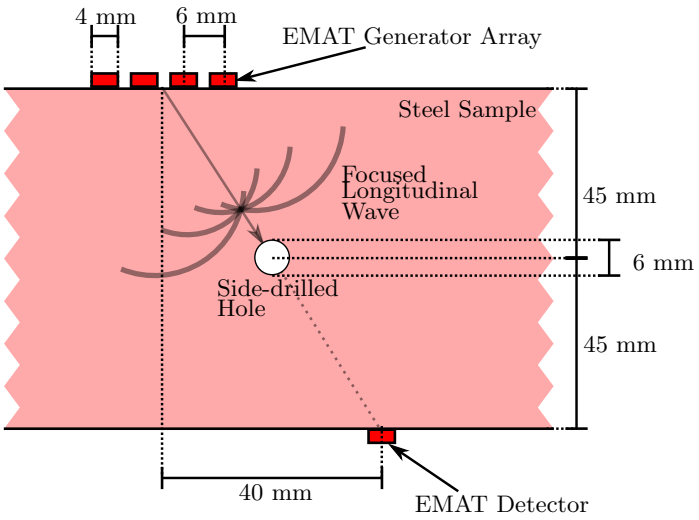

Figure 7.15: Schematic diagram of the angled-incidence transmission experiment used to experimentally verify the model outlined in section 7.2.2. The steel sample used for this experiment was not as-cast, and so had smooth surfaces and did not contain the coarse, inhomogeneous grain structures expected in a cast sample.

to be more complicated, and the measured A-scan data harder to interpret. The finite element data in figure 7.14 suggest that the arrival times of mode-converted signals may be used to infer the size of the defect, but for the reasons outlined above, this may be difficult in real samples. The presence of the defect can nevertheless be inferred from the variation of the transmitted signal amplitude and the appearance of spurious signals arriving after the incident longitudinal wave pulse, which correspond to mode-converted shear waves that have scattered from the defect.

7.2.3 Experimental Demonstration of the Angle Transmission Setup

To first demonstrate the operation of the angle transmission detection experiment in a sample with a known defect geometry, a scan was first performed on a flat-sided 90 mm thick steel block with a 6 mm circular side-drilled hole at a depth of 45 mm (see figure 7.15). The coils were wound into 3D-printed plastic templates that were attached to a rigid aluminium frame to maintain a constant lateral separation of 40 mm between the generation array and detection coil. The sensors were held flush to the sample surface using a spring-loaded mechanism to ensure minimal liftoff variation. The transmitted signal was recorded at 2 mm intervals along the block's length, the magnitude of the signal's Hilbert transform was calculated for each position and plotted in a B-scan image (see figure 7.16a). The transmitted longitudinal signal is visible here at an arrival time of 16 μs. The side-drilled hole is located at a lateral position of 110 mm from the start of the B-scan. As the generation array

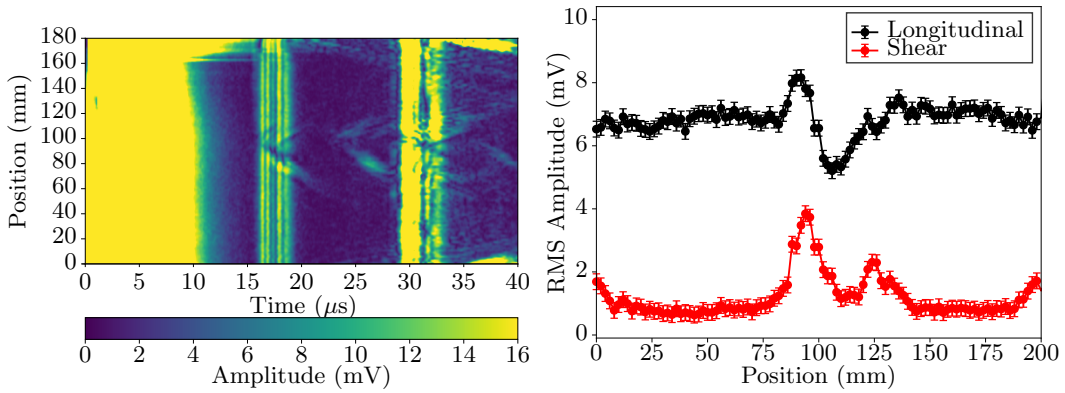

Figure 7.16: Figure 7.16a shows the angle transmission experiment B-scan data recorded on a smooth-surfaced, 90 mm thick processed steel sample with a 6 mm diameter side-drilled hole defect. Figure 7.16b shows the RMS values of the longitudinal and mode-converted wave pulses from time bins of 15 - 19 μs and 22 - 28 μs respectively.

is scanned over the defect, such that it lies between the ultrasound source and detection EMAT, the RMS value of the transmitted pulse varies, demonstrating that defects can be detected from anomalies in the transmitted amplitude (see figure 7.16b). It is observed that as the assembly moves towards the defect, there in an increase in the received signal amplitude as some incident waves at the edge of the incident beam, propagating away from the detection transducer, are reflected back towards the detector. This is followed by a decrease in the transmitted signal as the defect blocks the incident beam, before a return to the baseline measurement.

Mode-converted shear waves are also detected as the assembly passes over the side-drilled hole, at a time interval of approximately 22 - 28 μs (although the arrival time changes as the assembly comes closer to, and then further away from, the defect). The variation of the RMS amplitude of the mode-converted signal is also shown in figure 7.16b, and shows a clear increase in signal amplitude as the assembly approaches the defect.

These experiments experimentally verify the indications suggested by the finite element analysis results in figure 7.14; namely, that internal defect indications are given by a variation in the transmitted amplitude of the longitudinal wave pulse and the appearance of mode converted signals.

7.2.4 Measurements of Real Casting Defects

Following from the experimental demonstration of the angle-transmission setup on a processed steel sample with an artificial, side-drilled hole defect, attempts were made

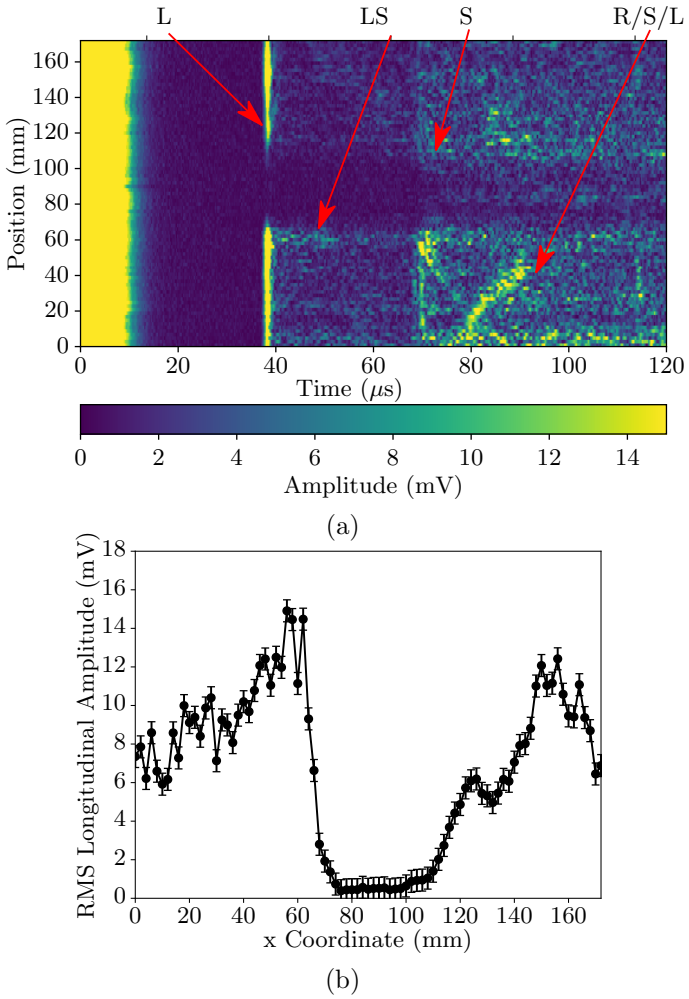

Figure 7.17: B-scan data recorded for the fully cracked sample shown in figure 7.9a. The gap in the transmitted longitudinal signal, L, between 70 and 110 mm, corresponds to the EMAT transmission assembly passing over the vertical crack in the sample. An increase in mode-converted signal content, LS, is observed at the crack edges. S corresponds to a directly-transmitted shear wave, and R/S/L corresponds to spurious reflected and mode-converted signals.

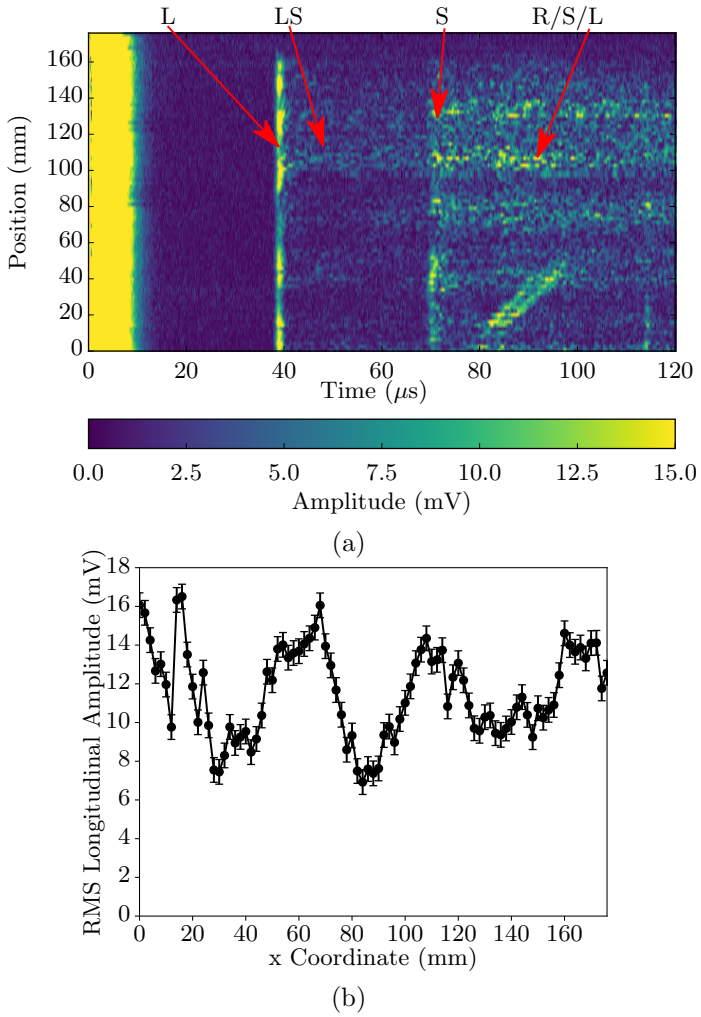

Figure 7.18: B scan image of the sample shown in figure 7.9b, which shows no outward signs of cracking. Variation in the amplitude of the transmitted longitudinal wave, L, is indicative of internal crack defects, as explained in section 7.2.2. Spurious signal content corresponding to scattered and mode-converted waves, LS, is also visible, between L and the directly-transmitted shear wave, S. As was the case for figure 7.17, signal content arriving after S (R/S/L) is hard to attribute to bulk scattering processes.

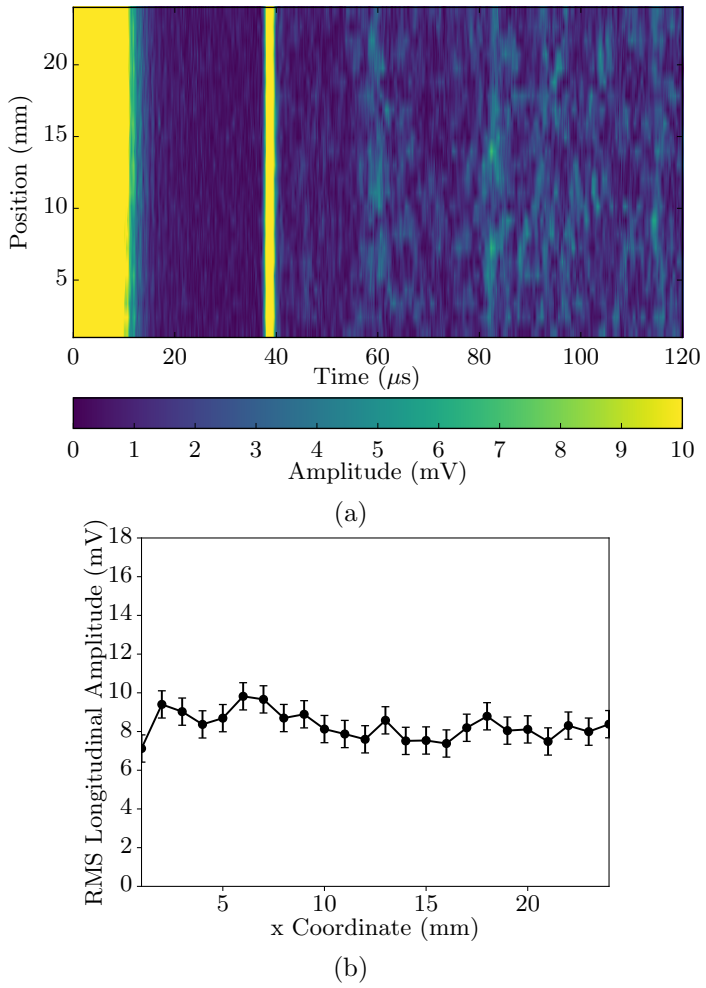

Figure 7.19: B scan image of an as-cast steel sample cut from a non-defective slab. The transmitted longitudinal signal is visible at 37 μs.

to detect real vertical cracking defects in the industrial cast steel samples shown in figure 7.9. A-scan data were recorded at 2 mm intervals using the same setup as described above to measure a B-scan image of the test pieces. The first data set was recorded for the sample containing a full-thickness vertical crack defect that breaks the casting surfaces, shown in figure 7.9a; the B-scan image for this sample is shown in figure 7.17a. There is a clear drop in the transmitted longitudinal wave signal amplitude between 67 and 112 mm, corresponding to the large, visible vertical crack lying between the generation array and detection EMAT, and hence preventing the incident wave pulse from reaching the detector. There is also a small increase in the signal content between 41 and 67 μs, at a spatial position of 64 mm, corresponding to mode-converted shear waves that have scattered from structures in the sample's bulk and arrive between the incident longitudinal and shear wave pulses generated by the array. The relative amplitudes of these shear wave indications are small compared to the variation of the longitudinal signal, suggesting that the variation of the longitudinal pulse amplitude may provide a better indication of internal defects. The variation of the RMS longitudinal wave amplitude, arriving at approximately 39 μs, is shown in figure 7.17b. There is a clear and substantial decrease in the longitudinal wave amplitude to near zero when the crack lies between the generation array and the detector, followed by a gradual return to the baseline measurement. The baseline itself is noisy, both due to stochastic noise and due to a variable oxide scale thickness on the sample's surface.

The data shown in figure 7.17 are encouraging, because they clearly demonstrate the coincidence of the expected defect indications with the position of the known defect in the sample, but the experiment itself is not particularly interesting due to the extreme nature of the defect. B-scan data were therefore also recorded for the sample (shown in figure 7.9b) without cracking defects that are apparent from inspection of the casting surface (though the presence of internal defects was confirmed by TFM imaging, see figure 7.11b). The data recorded from this B-scan are displayed in figure 7.18a, and show both a variation in the transmitted longitudinal wave amplitude and the appearance of spurious, mode-converted signals that have scattered from within the bulk of the material. The longitudinal wave amplitude variations shown in figure 7.18b are not as extreme as those shown in figure 7.17b, as the longitudinal wave is still able to propagate around the cracks, since they do not span the full depth of the sample. Some sections of the data show relatively little point-wise prolonged variation (for example, the regions between 50 and 70 mm, or 160 to 170 mm), and there are marked, consistent decreases in the transmitted amplitude in other regions (for example, between 70 and 105 mm and

15 and 50 mm). These localised and large variations are consistent with structures blocking the transmitted signal (see figure 7.19 for a comparison with a non-defective sample), although a more thorough benchmark measurement would be required to verify the presence of these defects in these locations in this sample.

The variations in longitudinal wave amplitude are difficult to attribute solely to scattering structures within the bulk blocking the incident beam; the surfaces of these samples are rough and oxide scale is present, so even though a spring-loaded mechanism is used to keep the coils pressed flush against the sample, there are still likely to be liftoff variations, which will affect the transmitted amplitudes significantly. The indications that can be solely attributed to scattering processes in the bulk are the spurious, mode-converted signal that appear in the time interval from 41 and 67 μs, such as those observed at scan positions of 36, 115 and 148 mm in figure 7.17a. These shear wave indications have a much lower amplitude than the variation in longitudinal wave amplitude, suggesting that the longitudinal pulse amplitude variation may provide the more reliable indication of internal defects, provided the variations can be attributed with confidence to internal sample variations and not coupling efficiency variations related to surface quality or sensor liftoff. In figures 7.17b and 7.18b, the point-wise uncertainty in RMS amplitude has been estimated from the standard deviation of the measured amplitude variation between multiple measurements on a cast sample without internal defects, but still with a comparable surface quality in terms of roughness and oxide scale (see figure 7.19). That the variations observed in figures 7.17b and 7.18b are significantly larger than the observed amplitude variation in a comparable, non-defective sample suggests that these longitudinal pulse amplitude variations can be attributed to the presence of internal defects with confidence. Confidence in these indications is further justified through the coincidence of these longitudinal amplitude variations with the aforementioned mode-converted shear wave indications.

The significance of these indications is made more apparent when compared to data recorded using a sample that contains no internal crack defects; the B-scan data recorded from a non-defective as-cast slab sample are shown in figure 7.19a, and show little variation in transmitted longitudinal wave pulse amplitude as the assembly is scanned across the sample, nor is there significant spurious signal content. A more clear comparison of individual scan points can be made by plotting A-scan data from each scan on the same axes. A-scan data from the cracked sample from a suspected defective region, recognised by the appearance of significant signal content between 41 and 67 μs, is plotted against A-scan data from the centre of the non-defective sample in figure 7.20. Comparison of signal amplitudes between

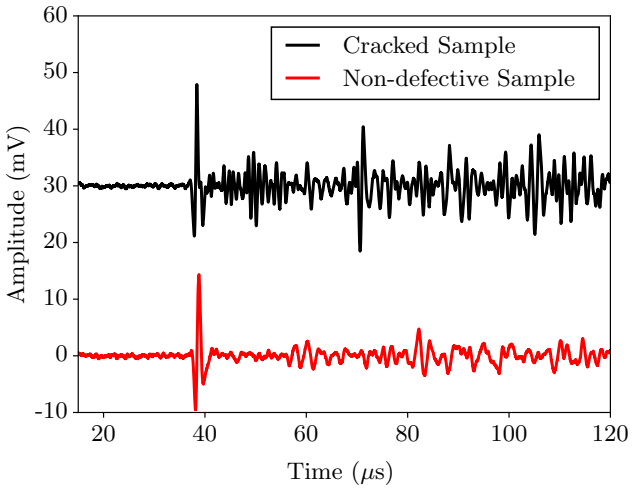

Figure 7.20: A direct comparison of amplitude data recorded in the defective slab sample (at position 108 mm) and in the non-defective sample (at position 15 mm).

different samples is not necessarily reliable due to expected variation in parameters such as conductivity and acoustic attenuation and sensor liftoff, which accounts for the relatively small difference in transmitted longitudinal pulse amplitude between the two samples. However, the longitudinal wave amplitude data shown in figures 7.18b, 7.17b and 7.19b demonstrate that variation in the transmitted longitudinal signal observed in a scan of a single test piece can provide a reliable indication of the presence of internal defects. Between different samples, variations in material properties such as acoustic attenuation and electrical conductivity can not, for example, account for the significant difference in signal content observed between 43 and 65 μs, which can only be attributed to scattering processes in the bulk of the cracked sample. This conclusion is verified by the observed indications in figure 7.11b, which demonstrates that internal defects are indeed present in this sample.

7.3 Conclusions

This chapter has outlined methods of bulk defect detection, following from the development of a phased array EMAT measurement system outlined in chapter 6. Section 7.1 discussed the application of an image reconstruction algorithm using forward-scattered mode-converted shear wave signals for the purposes of improving signal-to-noise ratios for detection and allowing for location and sizing of internal void defects. The proposed method was explored using finite element analysis and verified experimentally using side-drilled hole defects. However the method was unable to reliably image a 10 mm diameter side-drilled hole defect in a sample of

as-cast steel due to coherent noise arising from acoustic wave scattering from grain structures in the test piece. These results suggest that, using this instrument, in these samples, defects with a length scale of 10 mm cannot be reliably detected, and that the reliable detection limit is larger than this.

Section 7.2 outlined attempts to demonstrate the detection of genuine casting defects in samples obtained from a failed casting run at Tata Steel's IJmuiden plant. Ultrasonic imaging using a piezoelectric phased array was used to verify the presence of internal vertical cracking defects and estimate their approximate size for the purposes of informing the design of a finite element model. These experiments also demonstrated a lack of sensitivity to vertically-orientated defects, and so motivated the development of an angled-transmission setup. Finite element analysis of the angle-transmission concept demonstrated that the indications corresponding to vertical cracking defects are a reduction in longitudinal pulse amplitude and the appearance of spurious, mode-converted signals. These were verified experimentally on an artificial defect before being used on defective as-cast samples. The results indicate that these defects can be detected.

The experimental data presented in this chapter demonstrate that the phased EMAT array system can be used for detection of relatively large defects in industrial as-cast steel samples. This result is significant, because the EMAT system was designed with eventual adaptation to high temperature operation in mind, and suggests that online detection of these defects is a possibility.

Chapter 8

EMAT Optimisation for Surface Wave Applications

The results of this thesis thus far have concerned the development of a high-powered phased EMAT array system for probing the internal quality of as-cast steel products. There is, however, interest in the detection and quantification of surface-breaking defects on the cast slab.

This chapter outlines a novel analysis of Rayleigh wave generation from finite width sources and applies the results of this analysis to linear surface wave EMAT designs for the purpose of optimising the transmitted amplitudes. The analytical model is validated experimentally, and the use of phased array surface wave generation is proposed as a way of returning still-higher signal amplitudes.

8.1 Motivation

Rayleigh waves are of particular interest in the field of non-destructive evaluation (NDE), because their propagation characteristics localise them to the surface of a material. This makes them specifically sensitive to surface, or near-surface, defects, and restricts their propagation to two dimensions [70, 132], mitigating geometric attenuation and enabling comparatively large signal to noise ratios and long ranges of operation. Rayleigh waves have therefore been used for detection and measurement of rolling contact fatigue cracks in rail heads [132, 171, 172], detection of stress corrosion cracking defects [173] and for detection of surface-breaking defects in continuously cast steel slabs [108, 11], among other examples of industrial application. Particularly in industrial applications, optimisation of Rayleigh wave sources is important because Rayleigh waves can be heavily attenuated by surface roughness [80].

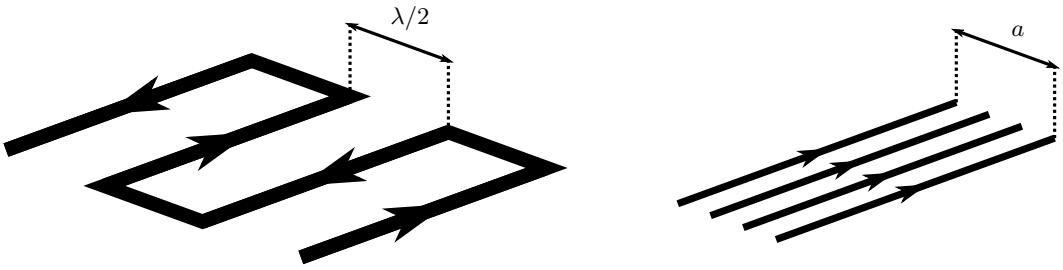

Figure 8.1: Schematic representation of the coil geometries for meander line and linear coil EMAT designs. The Rayleigh waves generated by the individual line sources in the meander line design are phase-matched when their separation is $\lambda/2$, where λ is the wavelength. This study concerns broadband pulsed excitation of linear coils of finite width a.

Rayleigh waves are most-often generated using piezoelectric angle beam transducers, due to their high efficiency. Angle beam transducers can be problematic in industrial applications, however, since they require good contact with the sample, cannot easily be used through coatings and the sensors are not robust to high temperatures [67, 9]. EMATs offer an alternative to piezoelectric transduction, but their poor transduction efficiency of EMATs can reduce their suitability for some industrial applications.

Optimised surface wave EMAT generator designs, most often termed 'meander line' EMATs, have been described previously in the literature, and make use of the phase matching that occurs between wave fronts separated by a half-wavelength to constructively add to the signal [174, 175] (see figure 8.1). These designs generate ultrasound most efficiently when excited with narrowband, toneburst current excitations, which can complicate and design of the driving circuit and interpretation of detected signals due to the reduced resolution afforded by temporally longer signals. The use of pulsed ultrasound that generates broadband temporally sharp signals, rather than narrowband continuously-excited, or toneburst, signals, can facilitate accurate analysis of reflected wave arrival times, which enables a defect's location to be accurately calculated [114, 10]. Moreover, broadband pulses contain a spectrum of wavelengths, and hence are sensitive to a range of characteristic defect sizes and depths, allowing the frequency response of transmitted signals to be used to measure the depth of surface-breaking defects [81]. For these applications, broadband, finite width linear EMAT coil designs are most appropriate [81, 176].

This study concerns the optimisation of linear Rayleigh wave EMATs by outlining a formalism for calculation of the generated waveform based on a convolution

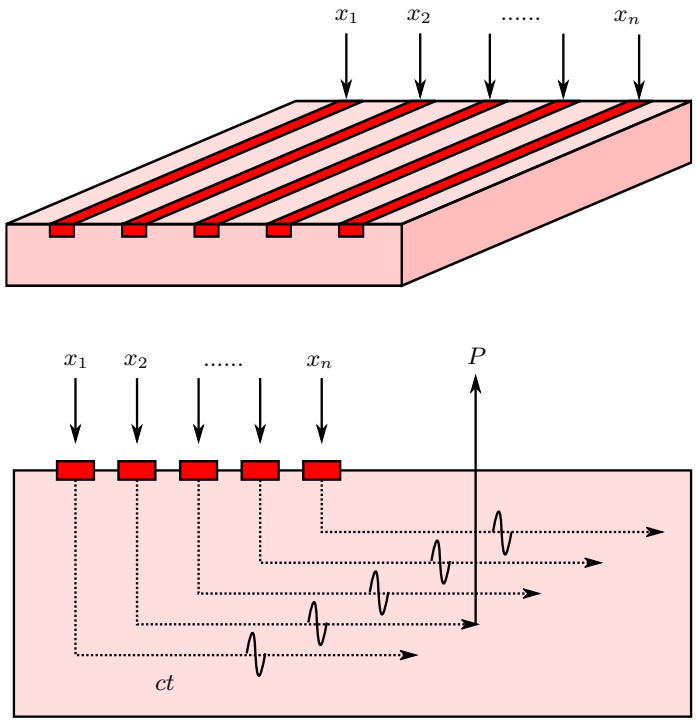

Figure 8.2: Schematic representation of the convolution model. Each individual source has an amplitude weighting described by a spatial profile function, $u_x(x)$. A detection point P, some distance from the edge of the coil, records contributions generated by each point source. There is a phase lag in the recorded time history from each source of x/c, where c is the Rayleigh wave speed.

integral. It has previously been acknowledged that the width of an EMAT coil is an important consideration when designing surface wave EMATs, and the optimum coil width is often cited to be equal to half of the wavelength of the propagating signal [176]. This result is presented without derivation or explanation, and importantly, is only true when considering continuous sinusoidal excitation signals. This work aims firstly to formalise the familiar result analytically, and extend the analysis to the operation of broadband pulsed transducers, which are of greater interest in the field of NDE.

8.2 Harmonic Excitation Finite Width Rayleigh Source

In previous studies concerning transducer modelling, generated bulk acoustic wavefields have been calculated by convolving the transducer's spatial impulse response with the velocity of the transducer surface. The spatial impulse response is determined by computing the Rayleigh integral of the source, by summing over spherical waves emitted at the transducer's surface [177, 178, 179, 180]. The concept of con-

volving a temporal excitation with a function describing the source geometry is used here to model surface waves generated by sources of finite width, for the purposes of EMAT optimisation.

Before developing a model for pulsed excitation, it is first helpful to derive the simplified case of a continuous sinusoidal excitation across a finite width rectangular pressure profile. Consider a finite width line of single point pressure sources on a half-plane, each acting as a harmonic wave source with equal amplitude (see figure 8.2). Consider also a detection point, P, at some distance, x, from the edge of the line of sources. The contribution of each individual point to the displacement, s, measured at point P is equal to some function of time, $u_t(t)$, multiplied by a weighting that is a function of distance from P, $u_x(x)$, and describes the form of the pressure profile due to the source geometry. The total signal, as measured at P, is the summation of all of these contributions. Inspection of figure 8.2 suggests that the signal from each individual source arrives with a phase delay of x/c, where c is the surface wave propagation speed. Hence, in the case where the wave sources are infinitesimally small and exist continuously along the spatial profile, the total signal is given by the integral:

$$\begin{aligned} s(t) &= \int_{-\infty}^{\infty} u_t\left(t - \frac{x}{c}\right) u_x(x)\, dx, \\ &= u_t(t) * u_x(x). \end{aligned} \tag{8.1}$$

The displacement is therefore described by the convolution of the temporal driving function with the spatial profile of the coil (denoted by the operator $*$). The convolution theorem states that the time series recorded at P can be expressed as the inverse Fourier transform of the product of the spatial and temporal bandwidths:

$$s(t) = \mathcal{F}^{-1}\tilde{u}_t(\omega)\,\tilde{u}_x(k), \tag{8.2}$$

where $\mathcal{F}^{-1}$ denotes an inverse Fourier transform, ω is the angular frequency, k is the spatial frequency and $\tilde{u}_t(\omega)$ and $\tilde{u}_x(k)$ are the signal's temporal and spatial frequency spectra respectively. This allows the total displacement to be more easily calculated by individually determining the Fourier transforms of the spatial and temporal profiles. In the case of a uniform rectangular source with finite width a, the spatial profile is described by the boxcar function:

$$u_x(x) = \begin{cases} 0 & -\infty \leq x \leq -\frac{a}{2} \\ 1 & -\frac{a}{2} \leq x \leq \frac{a}{2} \\ 0 & \frac{a}{2} \leq x \leq \infty, \end{cases} \tag{8.3}$$

The spatial bandwidth of this profile in terms of the spatial frequency, k, given by its Fourier transform, is a sinc function:

$$\tilde{u}_x(k) = \frac{a}{\sqrt{2\pi}} sinc\left(\frac{ak}{2}\right). \tag{8.4}$$

Similarly, the Fourier transform of the temporal driving profile can be determined to obtain the temporal bandwidth. Assuming harmonic excitation, the driving function can be represented as a complex exponential:

$$u_t(t) = Ae^{i\omega_0 t}, \tag{8.5}$$

where A is the amplitude of the driving signal and ω_0 is the angular frequency of the excitation signal. The Fourier transform of a complex exponential is given by the Dirac delta function:

$$\tilde{u}_t(\omega) = \delta_D(\omega - \omega_0). \tag{8.6}$$

The above expressions give the temporal bandwidth in terms of angular frequency and spatial frequency, and allow for evaluation of the measured signal $s(t)$ in accordance with equation 8.2. It is now necessary to make the substitution $k = \omega/c$, so that the expression for the total displacement is given only in terms of angular frequency, ω:

$$s(t) = \mathcal{F}^{-1}\left(\frac{aA}{\sqrt{2\pi}} sinc\left(\frac{a\omega}{2c}\right)\delta_D(\omega - \omega_0)\right), \tag{8.7}$$

This equation provides an expression for the displacement time history as measured at point P, but since this study concerns EMAT detection, which is sensitive to the surface particle velocity [106], it is appropriate to take the derivative with respect to time to determine the velocity profile, $v(t)$. Differentiation under the integral is permitted here according to Leibniz's integral rule:

$$
\begin{aligned}
v(t) &= \mathcal{F}^{-1}\left(i\omega\frac{aA}{\sqrt{2\pi}}sinc\left(\frac{a\omega}{2c}\right)\delta_D(\omega-\omega_0)\right), \\
&= i\omega_0\frac{aA}{\sqrt{2\pi}}sinc\left(\frac{a\omega_0}{2c}\right)e^{i\omega_0 t}, \\
&= \sqrt{2}iAc\sin\left(\frac{a\omega_0}{2c}\right)e^{i\omega_0 t}.
\end{aligned} \tag{8.8}
$$

The measured signal, $v(t)$, is therefore just a sinusoid with an amplitude dependent on the choice of driving frequency. In order to determine the maximum amplitude generated by the coil, this term should be extremised with respect to a. Hence, the derivative is computed and set to zero:

$$
\begin{aligned}
\frac{d}{da}v(t) &= i\sqrt{2}Ac\frac{\omega_0}{2c}\cos\left(\frac{a\omega_0}{2c}\right)e^{i\omega_0 t}, \\
&= i\omega_0\frac{A}{\sqrt{2\pi}}\cos\left(\frac{a\omega_0}{2c}\right)e^{i\omega_0 t}, \\
&= 0.
\end{aligned} \tag{8.9}
$$

Satisfaction of this condition imposes the following constraint:

$$
\frac{a\omega_0}{2c} = \left(n+\frac{1}{2}\right)\pi, \tag{8.10}
$$

where n is an integer. Now set $n=0$, which corresponds to the smallest coil width that satisfies this condition. The smallest n value is chosen because in practice, inductive and resistive losses increase with coil width and hence there is no advantage to designing a wider coil. This sets the condition on the coil width that:

$$
a = \frac{\lambda}{2}, \tag{8.11}
$$

where λ is the wavelength. This is a result that has been acknowledged in previous publications, although without full derivation [176]. This result can be intuitively explained by considering continuous point sources on a line generating sinusoidal displacement fields. Inspection of figure 8.3 suggests that for every point along the coil's width, the displacement field is completely cancelled by a corresponding point source spaced $\lambda/2$ away. Hence, for a coil larger than $\lambda/2$, there is a continuum in the centre of the coil where all contributions to the displacement field sum coherently, and contributions from the coil edges sum to zero.

Since this model assumes that the pressure loading is uniform, the largest

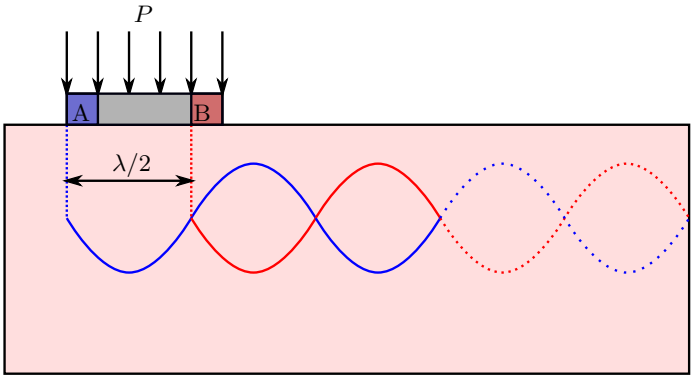

Figure 8.3: Model of a finite-width uniform harmonic pressure source. For each individual point in region A, there is a corresponding point in region B that is displaced by a distance $\lambda/2$, hence waves generated by these segments cancel and only the central region contributes to the total generated signal.

signal amplitudes will be achieved when using the largest possible coil, since the total signal input will increase with coil width. Increasing the coil width increases total displacement only up until the coil width is $\lambda/2$, however, at which point the cancellation effect occurs and the benefits of the larger coil width are lost. Practically, the optimum coil width is lower than $\lambda/2$, since

While this model provides useful intuition of the effect of source with on generation efficiency, it is less helpful for designing typical Rayleigh wave transducers, since in most NDE applications pulsed excitation signals are used, which contain a spectrum of wavelengths.

8.3 Broadband Pulsed Excitation of a Finite Width Coil

Following from the derivation of the harmonic driving case discussed in section 8.2, similar analysis can be performed to investigate the optimal coil parameters for a broadband pulsed excitation, which is more useful for NDE. Ideally, the choice of driving function should be arbitrary, since the pulses generated by EMAT driving circuits are not necessarily simple, smoothly-varying functions of time, however to simplify the analysis, a Gaussian driving function is chosen. This allows for easy computation of the Fourier transform and is a suitable approximation for a pulsed excitation circuit (see section 8.5).

Here, the Gaussian driving function is defined as:

$$u_t(t) = \frac{A}{\sqrt{2\pi\delta^2}} \exp\left(\frac{(t-t_0)^2}{2\delta^2}\right), \tag{8.12}$$

where A is the pulse amplitude, δ is the pulse width parameter and t_0 is the phase

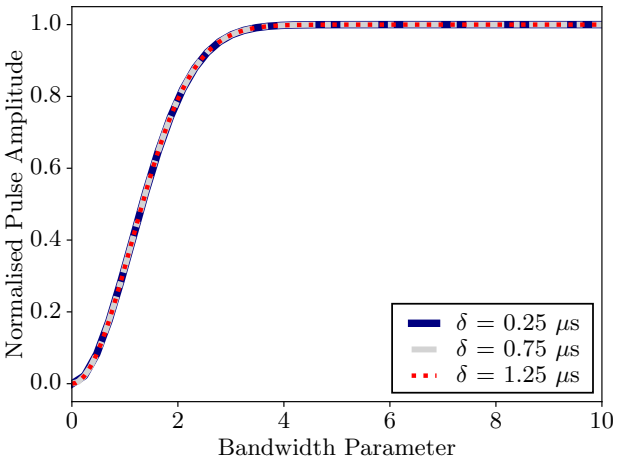

Figure 8.4: Plot of the variation of RMS signal amplitudes with the dimensionless bandwidth parameter, $R = a/\delta c$, for variation of the coil width (a) at fixed pulse width (δ). The plateau of the analytical model occurs when $R \approx 4.0$ for all values of δ.

offset of the pulse. The Fourier transform, describing the temporal bandwidth of the driving function, is given by:

$$\tilde{u}_t(\omega) = \frac{A}{\sqrt{2\pi}} \exp\left(\frac{-\delta^2\omega^2}{2}\right). \tag{8.13}$$

Since this model concerns the effect of broadband pulse excitation across a uniform finite-width coil, the boxcar function is still the appropriate description of the spatial coil profile, and hence the spatial bandwidth is given by equation 8.4. The signal, as recorded at the measurement point P, is therefore given as the time derivative of the inverse Fourier transform of the product of equations 8.4 and 8.13:

$$v(t) = \mathcal{F}^{-1}\left(i\omega \frac{A}{\sqrt{2\pi}} sinc\left(\frac{a\omega}{2c}\right) \exp\left(\frac{-\delta^2\omega^2}{2}\right)\right). \tag{8.14}$$

Evaluation of the integral transform in equation 8.14 is non-trivial. The transform can be evaluated numerically using a discrete inverse Fourier transform of numerical data generated using the bracketed term in equation 8.14.

To determine the optimal coil width parameter, a, fixed values of the temporal pulse width parameter, δ, were chosen and used to calculate the frequency content of the resulting pulses over a frequency range from 0.0 to 10.0 MHz. These were then converted to time domain data using an inverse fast Fourier transform

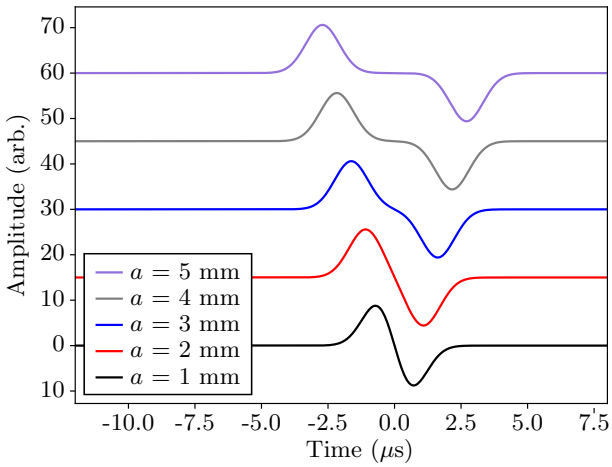

Figure 8.5: Data generated from the analytic convolution model for a fixed value of $\delta = 0.25$ μs showing how progressively-increasing coil widths lead to an optimum signal amplitude when $a = 3$ mm, after which there are no further amplitude improvements due to a plateau effect caused by separation of wave pulses generated by the coil edges.

(IFFT) algorithm, by populating the negative frequency bins of the input array with the positive frequency data, such that the spectrum is symmetric about the y axis at 0.0 MHz. The root mean square (RMS) of the results were then calculated as a measure of the pulses' amplitudes. This procedure was repeated for a range of coil widths between 0.01 and 40 mm and a range of δ values between 0.25 and 1.25 μs (see figure8.4).

The aim of this study is to establish a relationship between the coil width, a, and the temporal width parameter, δ, which gives an optimised RMS pulse amplitude. It is therefore helpful to consider the RMS pulse amplitude as a function of a dimensionless ratio of the coil width and temporal width, here termed the coil bandwidth parameter and defined as:

$$R = \frac{a}{\delta c}. \tag{8.15}$$

The normalised RMS pulse amplitude at a fixed δ was plotted against R for coil width parameters varying from 0 to 10 (see figure 8.4). As the coil width increases with respect to the temporal width of the driving pulse, there is an increase in the RMS amplitude of the Rayleigh wave until $R \approx 4.0$, at which point the function plateaus; since R is a dimensionless quantity, this occurs regardless of the value chosen for δ. This result is interesting, since it suggests that there is an optimal coil

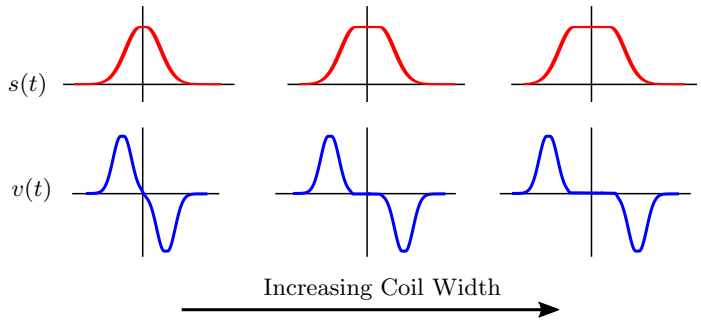

Figure 8.6: Representation of the effect of the convolution operation on the displacement pulse $s(t)$ and the measured surface particle velocity $v(t)$ as the coil width is increased. For larger coil widths, the displacement pulse contains a flat region, which manifests as two distinct pulses in the particle velocity time history. Hence, once pulse separation is achieved, there is no further benefit to increasing the coil width.

width when $R \approx 4.0$, after which there is no further benefit to using a wider coil. This is comparable to the harmonic driving case; increasing the coil width leads to an optimum generation efficiency once the spatial and temporal bandwidths are matched, although since a pulse contains a spectrum of wavelengths, it is less-obviously derived from an explanation based on the superposition of sinusoids as provided by figure 8.3.

Intuitively, this can be explained by considering that the pulse generated by a finite width coil driven by a pulsed excitation current is a convolution of the rectangular shape of the coil with a Gaussian excitation, which, in physical terms, can be considered to be a 'smearing' of the temporal excitation across the rectangular coil (see figure 8.6). Provided the spatial bandwidth due to the coil profile is larger than the frequency bandwidth due to the temporal driving function, the propagated displacement pulse will approximate a Gaussian profile, since the frequency content is dominated by the temporal driving function. As the coil width is made larger, such that the bandwidth due to the coil shape becomes narrower than the temporal bandwidth, the displacement pulse will begin to more resemble the square shape of the coil as the spatial bandwidth starts to dominate. Since the coil in this model is uniform, the displacement profile is flat in its centre when the coil's spatial bandwidth is small relative to the driving pulse (which occurs at large coil widths). Since the EMAT is sensitive to the time derivative of this profile, and the time derivative is zero in the flat region, the pulse shape changes from being a single Gaussian-type pulse, to being composed of two distinct pulses, which only correspond to generation at the coil edges. Thus there are diminishing returns when using increasingly large coils, since the central region of the coil does not contribute

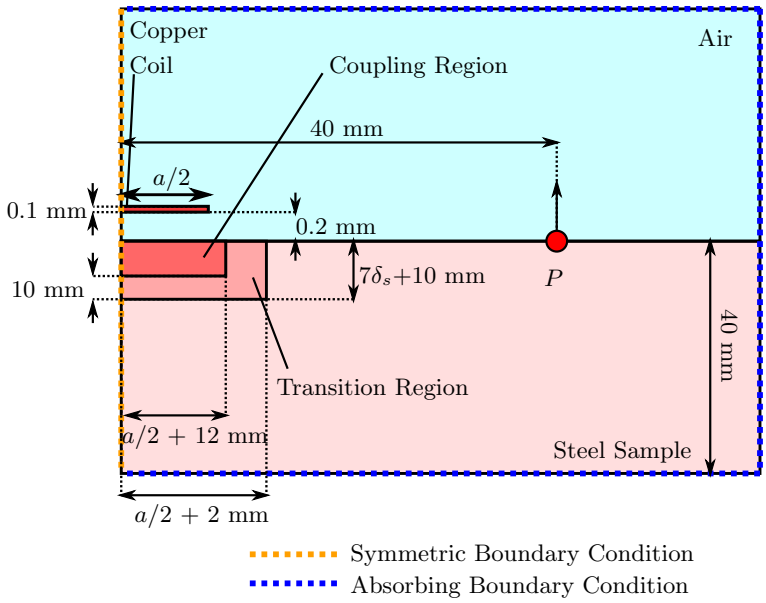

Figure 8.7: Finite element model geometry, showing the relative positions of the coil (with width a), the coupling region (with depth δ_s), the transition region and the sample. The model is simplified through the application of symmetric boundary conditions on the left axis. The detection coil was modeled by recording the surface particle velocity at point P.

to the detected signal.

As the coil width is increased from zero, increasingly more of the coil contributes constructively to Rayleigh wave generation and the RMS amplitude of the wave increases (as discussed in section 8.2 for the harmonic driving function case). As the spatial bandwidth surpasses the temporal bandwidth, the extra contributions no longer contribute to the generation and the RMS amplitude as a function of coil width flattens off.

8.4 Finite Element Modelling

The model presented in section 8.3 is simplistic, in that it does not fully consider material properties or solutions to the wave equation, and so validity of the model for wave propagation in real elastic media is unclear. Experimental verification of the optimum coil result is difficult for several reasons:

1. Real EMAT coils do not behave as rectangular pressure profiles; the analysis above assumes that the pressure applied by the EMAT is uniform across its whole width. In reality, there will be spatial variation in the Lorentz force amplitude across the width of the coil, which means the definition of the coil

width parameter, a, is somewhat ambiguous, and may not correspond to the width of a boxcar function as discussed in section 8.2.

2. Real EMAT pulsing circuits do not typically generate Gaussian current impulses; while the Gaussian impulse provides a reasonable approximation to a broadband current impulse excitation (see figure 8.12), the actual temporal profile of the pulse can be non-trivial and rarely is described by a Gaussian function.

3. There are additional effects that were not considered in the analytical model described above. Namely, any increase in the coil width requires an increase in the number of turns the coil has. The effect of this is to increase the wire length, which introduces resistive losses, which reduce the pressure induced by the coil for any given excitation voltage. It will also change the inductive impedance of the coil-sample system, which will change the frequency response of the system, as will changes the separation between the coil and the sample (the liftoff).

A finite element model was therefore constructed to test the predictions of the analytical model, since it is comparatively simple to model an unphysical coil in which the exerted force per-unit length remains constant with coil width, and where the temporal driving function exactly matches the Gaussian impulse modeled in section 8.3, whilst also fully accounting for the effects of material elasticity, wave propagation and the electrodynamics of the generation mechanism. The commercial software package COMSOL Multiphysics® version 5.3a was used for all following finite element calculations [181]; the magnetic fields interface of the AC/DC module was used to calculate the Lorentz forces induced in the sample, and the solid mechanics interface of the structural mechanics module was used to model elastic waves resulting from the induced electromagnetic forces. The model geometry was specified as shown in figure 8.7.

For valid comparison with the analytical model outlined in section 8.3, a Gaussian Lorentz force profile, with some desired width parameter δ_1, is required. Equation 5.19 demonstrates that the equivalent induced pressure is proportional to the square of the excitation current, and hence the current producing the Lorentz force distribution should be proportional to the square root of a Gaussian with the desired value of δ_1. Inspection of equation 8.12 demonstrates that the square root of a Gaussian with width parameter δ_1 is another Gaussian with width parameter $\delta_2 = \sqrt{2}\delta_1$. The current excitation was therefore chosen to be a Gaussian with $\delta_2 = 0.35$ μs, such that the width of the Gaussian describing the Lorentz force's

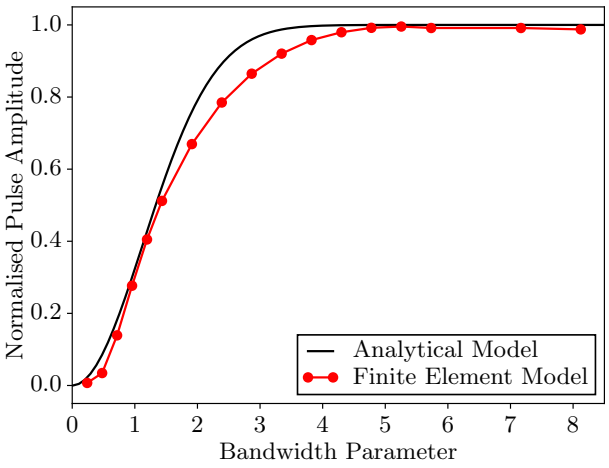

Figure 8.8: Plot of the variation of RMS signal amplitudes with the dimensionless bandwidth ratio parameter, $R = a/\delta c$. The plateau of the analytical model occurs when $R \approx 4.0$, and the plateau of the finite element data occurs at approximately $R = 4.5$.

temporal profile, $\delta_1 = 0.25$ μs, allowing for direct comparison with the experimental results presented in section 8.5. For valid comparison with the analytical model, the Lorentz force per unit area was kept constant by enforcing a constant peak current density in the excitation coil of 583000 Am^{-1} (a value chosen on the basis of the current measurements shown in figure 8.12, to give a peak current amplitude of approximately 1.75 kA in a coil of width 3 mm).

A Fourier transform of a Gaussian with $\delta = 0.25$ μs indicates that the highest frequency of physical phenomena in the model is 3 MHz. At 3 MHz, in a steel sample with an electrical conductivity of 4.032×10^6 Sm^{-1} and a relative permeability of 1, the skin depth, δ_s, is approximately 0.14 mm. To accurately model electrodynamic phenomena associated with induced currents in the sample, the coupling region depth was specified to be $7\delta_s$ (1 mm), so as to allow the induced currents and magnetic fields to fall to approximately zero within this region. The mesh density was specified so that there were 5 elements per skin depth (giving a maximum element size of 0.03 mm), so that spatial variations in the electromagnetic fields could be adequately resolved by the model. Calculating the whole model with this mesh density would be computationally expensive, so a lower mesh density was specified for the sample away from the coil. A transition region with a maximum element growth rate of 1.1 was defined between the coupling region and the rest of the sample to ensure there were no abrupt changes in mesh density.

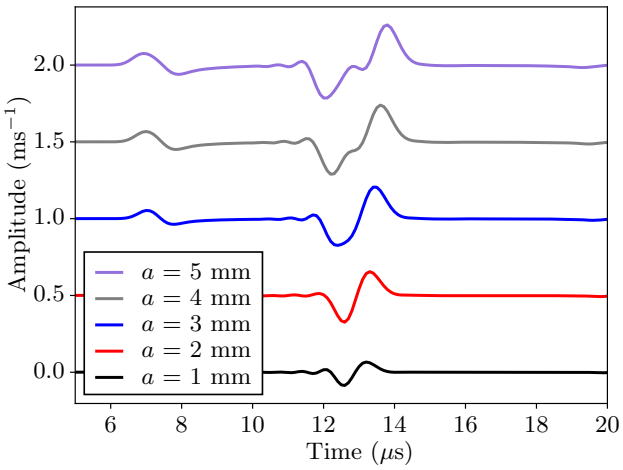

Figure 8.9: Finite element data calculated for a Gaussian excitation of $\delta = 0.25$ μs applied to uniform pressure profiles with width a showing the pulse separation effect described in section 8.3 leading to reduced RMS amplitude.

The slowest wave speed of interest is the Rayleigh wave speed, which is approximately 2900 ms^{-1} in steel, and the highest frequency content in the excitation signal is approximately 3 MHz, giving a minimum wavelength of 1 mm. A minimum mesh density of 16 elements per wavelength for the sample outside of the coupling and transition regions was specified to ensure numerical accuracy for the elastic wave calculations, hence the maximum element size in the sample region, outside of the coupling and transition regions, was set to be 0.06 mm. The whole of the modeled sample region, coupling region and transition region was meshed with free two-dimensional linear quadrilateral elements. The copper coil was modeled using free two-dimensional linear triangular elements with size 0.3 mm, and the region of air was modeled using free two-dimensional linear triangular elements of variable size, but with a specified maximum size of 5 mm and a maximum growth rate of 1.3. The maximum timestep size was set to be half of the propagation time of a longitudinal acoustic wave (with propagation speed 5950 ms^{-1}) across the smallest element in the model (the 0.03 mm skin depth elements), giving a maximum timestep size of 5 ns. These mesh parameters were determined empirically by ensuring that calculated quantities converged and did not deviate by more than 1% when finer mesh parameters were used. They are broadly in agreement with mesh parameters outlined in previous finite element studies of EMAT models [182, 183, 184].

The Gaussian pulse width of the coil's driving current, δ_2 was held constant at 0.35 μs while the coil width, a, was varied between 0.5 and 6.0 mm. The detection

point was modeled by calculating the horizontal component of the node velocity at a chosen measurement node (at a distance of 40 mm from the centre of the pressure load region), since this best-approximates an infinitesimal detection point and EMATs are velocity sensors. As in the case with the analytical model, the RMS of the velocity time history was recorded and plotted against the coil bandwidth parameter, R (see figure 8.4). There is reasonable agreement with the analytical model; similar behaviour is observed in figure 8.7, with a steady rise in the RMS amplitude value as the coil width is increased, up to a maximum value when $R \approx 4.5$ (*c.f.* $R \approx 4.0$ for the analytical model), after which there is a plateau, with no further signal improvements with increasing coil width. The difference between the finite element results and the analytical model is that the rate of increase in the signal amplitude is not as high in the finite element data as the analytical model would suggest. The result of this is that the analytical model predicts the establishment of the plateau for slightly lower coil widths than are seen in the finite element data. There is also a slight drop in signal amplitude with increasing coil width beyond this point, although this is small and the result converges on the high point observed in the plateau. This can be accounted for by considering that the propagation medium is elastic and has some response to the driving function, and that the wave pulse amplitudes resulting from the Gaussian pressure excitation may not follow the driving function identically. Likewise, the spatial extent of the driving function is not strictly localised to the area directly under the modeled coil, since the electromagnetic fields will extend beyond the coil's limits and since the application of a stress profile induces a strain field which will extend beyond the dimensions of the coil.

A-scan data determined from the finite element calculations are plotted in figure 8.9. The data show a gradual increase in pulse amplitude, which is limited beyond $a = 3$ mm as the distinct pulses generated at the coil's edge begin to separate, and hence qualitatively agree with the data generated by the analytic model shown in figure 8.5

Notwithstanding the simple approximations of the convolution model, the finite element data agree well with the analytic calculations. The finite element model itself represents an approximation of true experimental conditions, and so experimental data are necessary to determine the practical usefulness of the result given in figure 8.4.

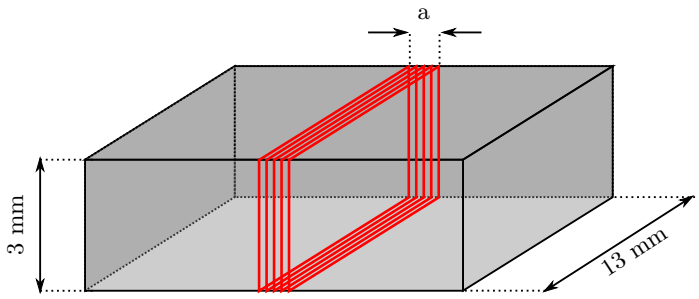

Figure 8.10: Schematic diagram of the linear generation coil design showing the copper wire coil in red and the 3d-printed plastic former in grey.

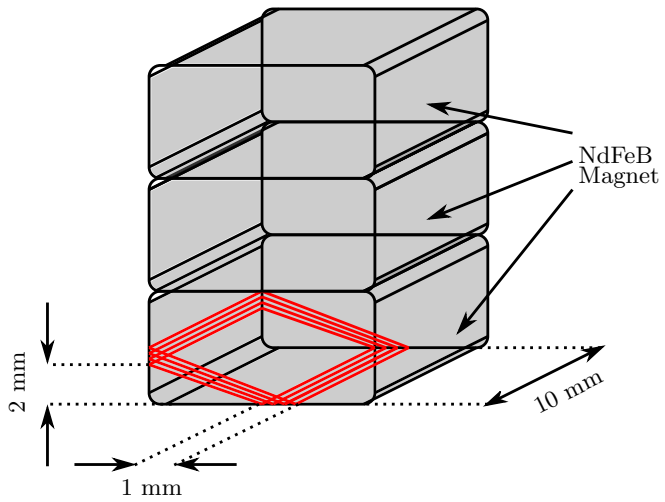

Figure 8.11: Schematic diagram of the detection coil design, showing the copper wire coil in red and the stack of permanent magnets in grey.

8.5 Experimental Verification of the Convolution Model

To validate analytical and computational models discussed in sections 8.3 and 8.4, an experimental study into the effect of coil width on generated Rayleigh wave pulse characteristics was undertaken. As noted in section 8.4, an experimental study would be subject to additional, unmodelled factors, such as variations in electrical impedance with coil width, or a non-Gaussian excitation pulse. The results of these experiments would therefore not be expected to replicate the model results exactly, but the approximate behaviour described by figure 8.4 should be observed.

To validate the model, a series of EMAT generation coils with widths varying between 1 and 7 mm were wound into kapton tape wrapped around 3d-printed plastic formers using 0.14 mm diameter copper wire. A linear coil design was chosen as a reasonable approximation to the boxcar pressure profile used in the analytical and finite element models (see figure 8.10). The EMATs described here operate on the self-field Lorentz mechanism, in which the induced eddy currents resulting from the EMAT coil's dynamic magnetic field themselves interact with the dynamic field (see section 5.1). The mechanical pressure in the sample is the vector cross product of the induced eddy current density and magnetic flux density.

The current excitation was supplied by the pulse generation circuit described in section 5.3. It is important to note that the temporal pressure profile generated by the self-field Lorentz mechanism is proportional to the square of the temporal current profile, as shown in section 5.1, leading to the mechanical force having a higher frequency content than the driving current.

A detection EMAT coil was wound to receive the generated surface wave signals. By invoking the same arguments put forward in section 8.2, where the generation EMAT was considered as a finite width of infinitesimal point sources on the surface of a half-space, it follows that the width of the detection coil will also have a frequency-dependent effect on the measured signal, and hence it is necessary to construct a coil with minimum width, so that the received signals are predominantly a function of the temporal velocity profile of the particles due to surface wave propagation, and so that artefacts arising from the spatial bandwidth of the coil itself are reduced. A 1 mm wide linear detection coil, consisting of 5 turns of 0.14 mm diameter copper wire wound into kapton tape wrapped around a plastic former, was constructed. A stack of 5 NdFeB magnets were placed behind the coil to supply a vertical bias static magnetic field to enable sensitivity to in-plane particle motion. A schematic diagram of the detection EMAT design is presented in figure 8.11.

The generation and detection coils were placed 145 mm apart on a 90 mm thick flat steel sample free of surface-breaking defects. A-scan data were recorded

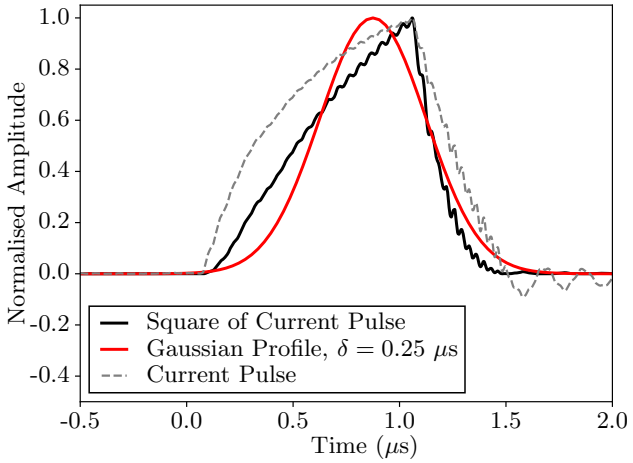

Figure 8.12: Plot of the driving current profile shown in grey, the square of this profile shown in black, and a Gaussian pulse with width parameter $\delta = 0.25$ μs shown in red.

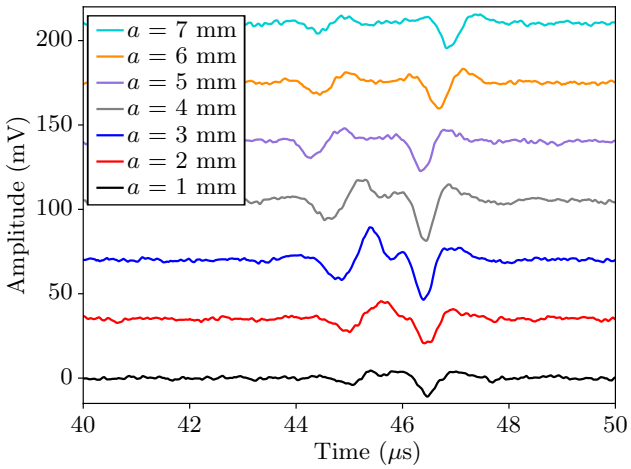

Figure 8.13: Experimental A-scan data recorded for a series of linear self-field EMAT generators showing the pulse separation effect demonstrated schematically in figure 8.6.

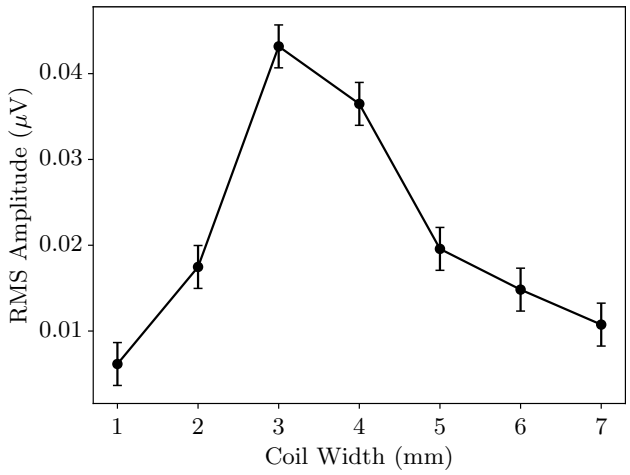

Figure 8.14: RMS values of the Rayleigh wave pulses shown in figure 8.13. The initial increase in wave amplitude up to a coil width value of 3 mm (corresponding to a coil bandwidth parameter $R = 4.0$) is in very good agreement with the analytical and computational modeling presented in sections 8.3 and 8.4). The subsequent drop in RMS amplitude is due to unmodelled factors, such as the increase in the coil's impedance with increasing coil size.

with 128 coherent averages and digitally filtered using a Butterworth bandpass filter between 0.1 and 5.0 MHz. Data were recorded for a range of generation coils, varying in width from 1 - 7 mm. The recorded A-scan data are shown in figure 8.13.

The general behaviour of the pulse characteristics appears to agree with the models described in sections 8.3 and 8.4; there is a clear initial increase in signal amplitude and a gradual separation of two distinct surface wave pulses, corresponding to generation at the coil edges, as the coil width is increased. The behaviour not accounted for in the analytic and finite element models in sections 8.3 and 8.4 does have a clear effect on the experimental results, however. Instead of a plateau in the signal amplitude established after the optimal coil width, there is a sharp decline, as seen in the plot of RMS pulse amplitude values in figure 8.14. This is due to the resistive impedance of the longer coils - since a larger length of wire is required to wind a wider EMAT, energy from the current excitation is lost to resistive losses in the EMAT coil, which reduces the current amplitude in the wire, and therefore leads to lower intensity ultrasound generation.

A rough verification of the model's agreement with experiment can be performed by approximating the Lorentz force supplied by the EMAT pulser as a Gaussian pulse. Taking the square of the current profile gives an approximation

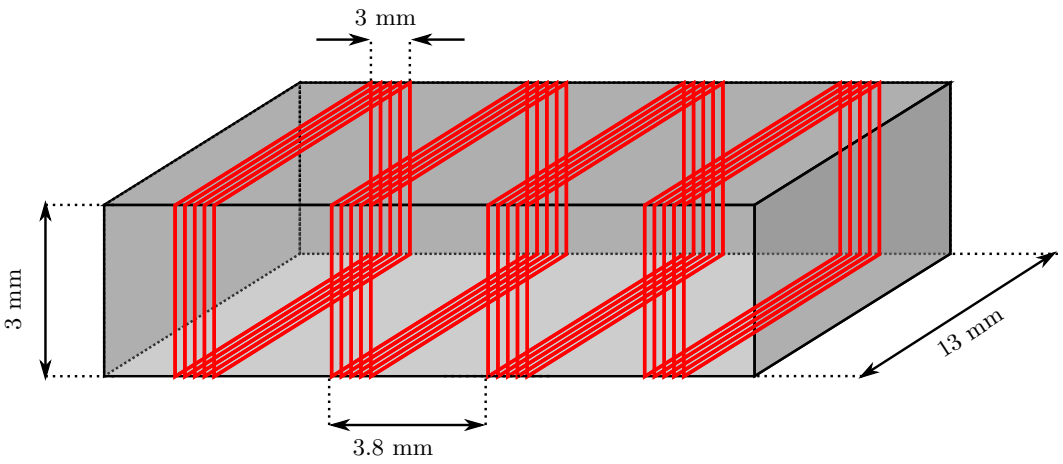

Figure 8.15: Schematic diagram of the phased Rayleigh wave EMAT array, showing the copper wire coils in red and the 3d-printed plastic former in grey.

of the temporal profile of the Lorentz force, which approximates a Gaussian function with width parameter $\delta = 0.25$ μs. The results of the models above indicate that the value of the coil bandwidth parameter at which spatial bandwidth dominates the form of the generation pulse, leading to separation of individual pulses generated at the coil edges, is $R = a/\delta c \approx 4.0$. Hence, for waves generated in steel (which has a Rayleigh velocity of 2900 ms^{-1}) by a temporal pressure profile with width parameter $\delta = 0.25$ μs, the optimal generation coil width is expected to be $a = R\delta c \approx 4.0 \times 0.25 \times 10^{-6} \times 2900$ mm $= 2.9$ mm. In the A-scan data presented in figure 8.13, 3 mm corresponds to the largest coil width before the two pulses become visibly discernible, and likewise corresponds to the highest measured value of the RMS pulse amplitude in figure 8.14, suggesting that the convolution model provides a valid description of EMAT surface wave generation.

8.6 Phased Array Signal Enhancement

The models outlined above demonstrate that when using EMATs, the detected signal strength (as measured by calculating the RMS amplitude of the detected pulse) increases with the generation coil width up to a maximum value before plateauing; the experimental verification study presented in section 8.5 shows that there is actually a decrease in the generated signal amplitude at higher coil widths due to the increased resistive losses in larger coils. There is therefore a limit to the RMS signal amplitude that can be generated by any given current source, before either the RMS signal suffers, or there are effects on the frequency bandwidth of the signal. Improvements in the Rayleigh wave signal amplitude beyond this are dependent on

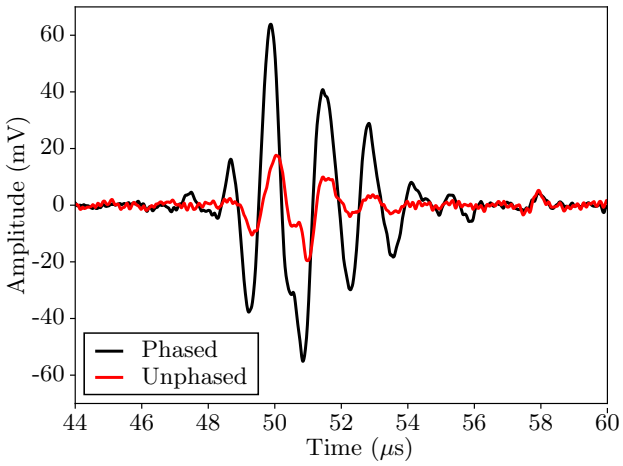

Figure 8.16: A comparison of the Rayleigh wave pulses generated by a single optimised EMAT generation source, and an array of four such sources, with phase delays applied between excitation of the individual sources, such that the Rayleigh wavefront is enhanced.

increasing the current amplitude of the excitation pulse, which itself is limited by the components available in the driving circuit. Extremely high current amplitudes in EMAT coils have been reported for spark gap discharge circuits, but these can be unsuitable for industrial measurements due to their requirements for regular maintenance and unreliable switching [145, 110].

An alternative means of improving the signal amplitude, while maintaining the broad bandwidth characteristics of the pulse, is to apply phase delays to a succession of optimally-sized finite width sources, such that the resulting surface acoustic waves interfere constructively to enhance the amplitude of the incident wave. Using this approach, it is possible to generate Rayleigh waves with relatively large amplitudes using driving electronics that are readily available, provided the excitation pulses can be reliably switched with the necessary phase delays. A phased EMAT pulser (described in section 6.2) was used to apply phase-delayed pulses to a Rayleigh wave EMAT array with dimensions described by figure 8.15. The phased array transducer was constructed by winding four 3 mm wide elements into kapton tape pressed around a 3d-printed plastic template with a separation of 3.8 mm between adjacent elements.

The elements were excited with current pulses as described in section 8.5, with time delays of $\Delta t = x/c = 1.27$ μs between adjacent elements, so that the generated Rayleigh waves coherently summed to produce a single, enhanced, wave

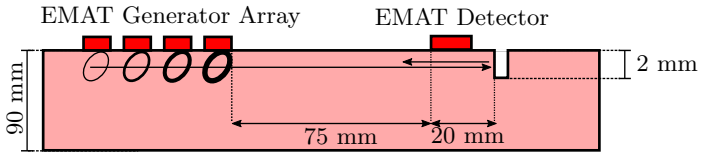

Figure 8.17: Schematic diagram of the surface-breaking defect detection experiment.

front. The signal recorded on the detection EMAT coil is shown in figure 8.16. The RMS amplitude of the generated signal is enhanced by a factor of 3.8 compared to the RMS amplitude of the signal generated by a single coil, which is in good agreement with the value of 4.0 that would be expected from the summation of 4 identical sources (it is expected that this value would be lower due to path lengths and attenuation).

8.6.1 Surface-Breaking Defect Detection

As a demonstration of the application of the phased array Rayleigh wave transducer, a surface defect detection experiment was set up. The four element optimised Rayleigh wave generator shown in figure 8.15 was placed on a steel sample that contained a 2 mm deep artificial vertical notch defect, with the detection transducer depicted in figure 8.11 placed between the generator and the notch (see figure 8.17). As described in section 8.6, phase delays were applied to successive elements of the generation array to constructively add to an incident Rayleigh wavefront. This wavefront is detected at a time of 25 μs as it propagates beneath the detection EMAT, before it reflects off the notch defect. The reflected pulse is detected at a later time of 40 μs (see figure 8.18).

This experiment was repeated when firing a single element of the generation array to quantify the improvement in sensitivity. The RMS amplitude of the wave pulse detected in the time window from 40 to 50 μs was calculated for the reflected pulse generated by the phased array and the reflected pulse generated by a single optimised EMAT coil. For each A-scan, the RMS amplitude of a region of noise without ultrasonic signals, the time window between 52 and 60 μs, was also calculated. The signal-to-noise ratio, as defined by equation 6.2, was then determined to be 4.2 for the signal from the single EMAT coil, and 9.7 for the signal generated by the phased array, suggesting that the use of a four-element phased Rayleigh generation array can improve defect sensitivity by a factor of 2.3 compared to the use of an optimised single-element transducer.

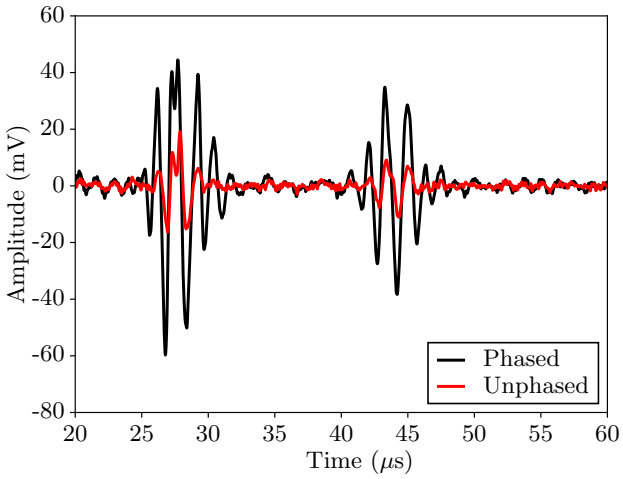

Figure 8.18: A-scan data recorded for the experiment described in figure 8.17. Then signal observed at 25 μs corresponds to the incident Rayleigh wave pulse, and the signal observed at 40 μs corresponds to the reflected defect indication. The use of four-element phased array generation improves the signal-to-noise ratio of the defect indication by a factor of 2.3 compared to the use of a single-element transducer.

8.7 Summary and Conclusion

A simple model of surface wave generation from a finite source was constructed, and it was shown that the generated temporal displacement profile, as measured by a point-like detector, is approximated by a convolution between the temporal driving function and spatial profile of the source. Analysis of this model indicates that optimal generation is achieved when the coil width is equal to a half-wavelength in the case of a harmonic excitation, which is in agreement with previously-published studies on EMAT generation of Rayleigh waves, although this result seems to have been determined from arguments of intuition rather than from robust derivation [176]. In the case of a pulsed Gaussian pressure excitation, the model predicts that optimal generation is achieved when the coil bandwidth parameter, $R = 4.0$. This result was verified using finite element analysis and experimental measurements using self-field linear EMAT coil designs and a high-powered pulsed current excitation.

This result has implications for further designs of Rayleigh wave EMAT coils. Firstly, it provides a useful and simple rule for optimal design of linear Rayleigh wave EMATs. Secondly, the verification of the convolutional model for surface wave generation allows for an extension of the analysis to other EMAT coil geometries, which may be more suitable for a given application. Spiral and racetrack designs, for example, are known to be relatively efficient generation sources due to the closed looped

eddy current profiles they generate, and previous studies have deliberately used transducers with spatially-varying generation profiles for the purposes of matched filtering.

Phased array enhancement of the optimised coils was also presented as a means to overcome the limitations of a given driving circuit, provided phase-delayed current excitations can be reliably provided. It was shown that in the case where four optimised Rayleigh wave generators were fired sequentially with appropriate time delays, the resulting Rayleigh wave's RMS amplitude was enhanced by a factor of 3.8, compared to the wave generated by a single EMAT coil, and the signal-to-noise ratio of the reflected signal from a crack increased by a factor of 2.3, presenting the prospect of a great improvement in surface defect measurement sensitivity. Further studies could investigate the lateral arrangement of these optimised Rayleigh wave sources, so that the wave enhancement can be performed across a two-dimensional plane, allowing for dynamic beamforming and imaging using surface waves.

Chapter 9

Conclusions

9.1 Thesis Summary

The inspection of thick, highly attenuative, rough-surfaced metal structures is an interesting research problem with broad industrial relevance from power generation to civil engineering [4, 5, 6, 7]; this thesis specifically concerns the problem of defect detection during continuous casting of steel, and outlines the development of a novel ultrasonic transduction technique that is capable of achieving practicable signal-to-noise ratios in as-cast steel samples, and has the potential to be applied in a harsh industrial environment. An introduction to steel casting and defect formation was presented in chapter 1. Chapter 2 provided an overview of non-destructive measurement technologies and presented the motivation for choosing electromagnetically-generated ultrasound for this application. The necessary background theory describing ultrasonic wave propagation and mechanical coupling of electromagnetic waves to electrically-conducting and magnetic media are introduced in chapters 3 and 4 respectively.

Chapter 5 detailed an original derivation of the equivalent surface pressure generated by a coil-only Lorentz force EMAT device, and showed that the surface pressure load is given by the magnetic pressure due to the surface flux density. The Lorentz force profile from a coil-only device can therefore be easily evaluated if the surface flux density is known. The method of complex images was used to analytically compute the equivalent surface Lorentz pressure for an infinitesimal wire current source, and this result was used to compute the equivalent surface pressure resulting from finite-width, one-dimensional current distributions representing EMAT coils. Section 5.2.2 demonstrated the use of these calculations in determining input pressure loads for finite element models of acoustic wave propagation.

Chapter 6 presented the motivation for developing a high-power phased

EMAT array instrument for generating ultrasound in as-cast steel samples. For this purpose, a new, high power phased EMAT array pulser system was developed, that is capable of supplying each of its four independent channels with currents of up to 1.75 kA for pulses with rise times of 1 μs. The modeling results from chapter 5 were used to support a finite element optimisation study aimed at designing a phased EMAT array suitable for inspection of internal defects near the centreline of a 225 mm thick industrial cast steel slab sample. The finite element data suggested that the optimised array should enhance the transmitted longitudinal ultrasound pulse by a factor of 3.5 compared to a single EMAT coil, and this result was validated experimentally using the pulsing system on a real industrial sample. Further signal enhancements were demonstrated with the use of an array of detection EMATs, and a preliminary defect detection experiment was presented.

Chapter 7 concerned the use of the phased array system developed in chapter 6 for the detection of defects in as-cast steel slab samples. The preliminary results of section 6.9 motivated the investigation of a transmission experiment and attempts to reconstruct images of the sample's interior using forward-scattered, mode-converted shear waves. Finite element analysis was used to demonstrate the proposed mode conversion imaging technique, and experimental validation was shown on a non-cast thick steel sample. The same technique applied to an industrial as-cast steel sample yielded much lower signal-to-noise ratios, and suggests that the limit of detection using this system in these samples lies above10 mm, as reliable detection of a defect of this size was not demonstrated. Attempts were then made to exploit the beam steering properties of the phased array to detect real vertical cracking defects in industrial steel samples. A finite element model of the proposed angle-transmission experiment suggested that variation in the transmitted signal amplitude and the appearance of spurious, mode-converted signals corresponding to scattering events at the crack tips indicate the presence of a defect. This result was verified experimentally on an artificial, side-drilled hole defect. The technique was then used to demonstrate the detection of real casting defects in industrial slab samples.

Chapter 8 introduces the problem of detection of surface-breaking defect detection in as-cast steel slabs. An original analytical description of Rayleigh wave generation from a linear EMAT coil of finite width, a, is derived and used to determine the optimal coil width parameters for the case of continuous sinusoidal current excitation. The model determines that the optimal width for the case of sinusoidal excitation is $\lambda/2$, which is in agreement with previous deductions of optimal coil width based on arguments of physical intuition. Using the magnetic pressure result from chapter 5.1, the case of Gaussian excitation of a high power EMAT device is

also derived, and the optimum coil width, as parameterised by the dimensionless ratio $R = a/\delta c$, where δ is the width parameter of the Gaussian excitation and c is the Rayleigh wave speed, is found to be given by $R = 4.0$. Finite element and experimental data are then presented in support of this result. The phased excitation of several optimised EMAT generator devices in a linear array to constructively enhance a generated Rayleigh wavefront is demonstrated as a means to improve the SNR beyond the limit suggested by the model.

9.2 Further Work

The work presented in this thesis has demonstrated that internal defects in as-cast industrial steel samples can be detected using EMAT-generated ultrasound, and has developed the concept of using arrays of high-powered generation devices to improve signal-to-noise ratios. The results presented in section 7.2 demonstrate that severe casting defects can be readily detected, although the detection of less-severe (though relatively large) defects in section 7.1 proved problematic due to the intrinsic attenuation of the material and coherent noise due to grain structures. The ability to detect severe crack-like defects is advantageous to casting machine operators, as these defects do periodically occur and economic savings can result from their early detection, but smaller defects, such as the mm-scale porosity defects associated with centreline segregation, are of much greater interest to steel manufacturers. The results of section 7.1 demonstrate that detection of these defects using the EMAT array system developed in this thesis would not be possible. Imaging algorithms for coarsely-grained, anisotropic materials have been developed for piezoelectric transducer arrays [185], though the specific problem of porosity imaging in as-cast steel slabs is not addressed in the literature, and the relative size of these defects compared to the typical grain size in steel slabs would likely make their detection difficulty, even using specialised imaging algorithms and more efficient transducers. The system developed in this thesis is therefore unlikely to be capable of detecting these smaller defects with further development, but the work presented in chapters 7 and 8 demonstrates a capability to detect severe internal cracking defects, and mm-scale surface defects, which is nonetheless useful to steel manufacturers.

All work presented in this thesis concerns only measurements performed under lab conditions, and at present, the experimental system developed during this project is not suitable for high temperature or industrial application. The EMAT devices developed in this thesis (see, for example, figure 6.9) consist of insulated copper wire wound directly onto a 3d-printed plastic substrate using kapton tape, and contain NdFeB magnets that are not robust to high temperature operation. For

application during continuous casting, the problems of robustness to high temperatures and to mechanical damage must be addressed.

Several studies have previously addressed the specific engineering problem of developing high temperature EMAT devices, including for bespoke application in the steel industry. For example, Baillie *et al.* developed a water-cooled EMAT detector for use with an ablative laser generation source for detecting surface-breaking cracks formed during the continuous casting of steel billets. The EMATs developed during this study were manufactured in a similar manner to those developed in this thesis; insulated copper wires were wound directly onto a permanent magnet using kapton tape. Robustness to high temperatures was achieved by keeping the sensor components themselves at relatively low temperatures; the EMAT was housed in a stainless steel casing that included a water jacket, and a continuous flow of water was used to remove heat from the sensor components. Thermal protection of the front face of the transducer was achieved through the use of an alumina ceramic tile, and protection from scraping damage was provided by a thin layer of austenitic stainless steel foil (which has both a low electrical conductivity and magnetic permeability, and so does not interfere with the EMAT's operation). Constant EMAT liftoff was achieved by using a pantograph to hold the sensor flush to the sample surface.

Other high temperature EMAT studies suggest the use of more thermally-robust sensor components instead of attempting to actively cool the sample. Lunn *et al.* used a bespoke high Curie-point magnet in a permanent magnet design, where bare copper wire coils were wound between alumina ceramic discs and electrically-isolated using alumina ceramic adhesive. The sensor was housed in a stainless steel casing, and a high-temperature coaxial cable using a ceramic inner insulated was used to connect the sensor to its supporting electronics.

With regards to the problem of robustness to mechanical damage, Petcher *et al.* developed an EMAT for high speed operation on rail that consisted of a permanent magnet held in a rigid case, and a thin, flexible titanium wear plate that held the EMAT coil, allowing for close proximity between the coil and the sample (thus reducing losses associated with sensor liftoff) while protecting the coil and magnet from the high speed scan over the rough rail head surface.

These examples demonstrate several strategies for the improvement of the EMAT sensors developed in this thesis for application during continuous casting. The successful operation of the laser-EMAT system demonstrated by Baillie *et al.* suggests that first attempts should be made by developing a stainless steel EMAT housing for the array sensors, that contains a water jacket for active cooling and

alumina ceramic thermal isolation between the sensor and sample. Replacing fragile components of the sensor design (such as insulated copper wire wound into kapton tape) with the high temperature components used by Lunn *et al.* (in this case, bare copper wire electrically isolated using alumina ceramic adhesive) would reduce the required efficiency of the active cooling system and help ensure robustness to high temperatures. Protection from mechanical damage would be best-achieved through the use of a titanium wear plate as demonstrated by Petcher *et al.*. though the experimental trials conducted by Baillie *et al.* suggest that the combination of an alumina ceramic plate with austenitic stainless steel foil should be sufficient.

Of further relevance to the problem of industrial robustness is the removal of permanent magnets from the detector EMAT design. Recent work published by Rueter details the development of a coil-only detector, in which the bias field is supplied by a large-amplitude, low frequency current excitation through the detection coil [163]. The removal of permanent magnets from the detection coils would make the problem of application at high temperature simpler, and may permit the close packing of elements in a detection array, improving the prospects for signal enhancement, or image reconstruction (as discussed in section 7.1.1).

The modeling frameworks outlined for surface pressure loading (in chapter 5) and efficient generation of surface waves (in chapter 8) are not specific to the intended application of this project. The inherent inefficiency of EMATs discussed in section 6.1 is often problematic; careful design choices must often be made to ensure maximum sensitivity regardless of the intended application. Previous frameworks reported for modelling EMATs mostly consider finite element models of complete electrodynamic-mechanical systems [186, 187, 188, 189], which can be computationally expensive and are more difficult to implement than the model outlined in chapter 5. Analytical models of EMAT surface pressure loading have been reported, but relied on numerical integration of analytically-derived integral expressions for the eddy current density, which presents numerical difficulties in the determination of appropriate cut-off regions and implementation of the integration [190, 191, 192]. The method presented in chapter 5 removes the requirement for numerical integration of Maxwell's equations to determine surface pressure loading by expressing the Lorentz force algebraically, reducing the complexity and computation time of EMAT models, and hence lending itself to future EMAT modelling studies.

The model of surface wave generation from a finite-width pulsed EMAT device presented in chapter 8 can similarly be easily extended to consider alternative EMAT coil configurations and temporal driving functions, allowing for optimisation of surface wave transducers for other intended applications; for example previous

studies have used concentrically-wound meander-line EMAT coils to perform geometric focusing of Rayleigh waves [82]. The convolution model described in section 8.2 could be applied to such EMAT designs for their optimisation.

The phased EMAT array for Rayleigh wave generation demonstrated in chapter 8 enables improvements in the signal-to-noise ratio of surface defect detection experiments, but in terms of the functionality and directivity of the resulting acoustic wavefield, the device behaves similarly to a single-element transducer. Recent publications have demonstrated the use of geometric focusing of Rayleigh waves using a concentrically-wound meander-line coil, for the purpose of obtaining fine resolution scans of surface quality [82]. A lateral arrangement of the Rayleigh wave EMAT elements would present the potential for dynamic Rayleigh wavefront focusing and steering, as was demonstrated for bulk longitudinal ultrasound in chapter 6. Such an experiment would demonstrate a novel capability to reconstruct ultrasonic images of sample surfaces without the need for scanning, and allow for beam forming and focusing in the plane of the surface to improve the signal-to-noise ratio.

Bibliography

[1] J. Sirgo, R. Campo, A. Lopez, A. Diaz, and L. Sancho, Industry Applications Conference, 2006. 41st IAS Annual Meeting. Conference Record of the 2006 IEEE **1**, 516 (2006).

[2] F. Boue-Bigne, Spectrochim. Acta, Part B (2008).

[3] H. Presslinger *et al.*, ISIJ Int. **46**, 1845 (2006).

[4] D. Diercks, W. Shack, and J. Muscara, Nucl. Eng. Des. **194**, 19 (1999).

[5] J. Collingwood, NDT Int. **20**, 33 (1987).

[6] S. Lee and N. Kalos, J. Civ. Eng. Manag. **21**, 654 (2015).

[7] W. Megid, M. Chainey, P. Lebrun, and D. Hay, Eng. Fract. Mech. **211**, 198 (2019).

[8] A. McNab, K. Kirk, and A. Cochran, IEEE Proc.-Sci Meas. Technol. **145**, 229 (1998).

[9] R. Turner, P. Fuierer, R. Newnham, and T. Shrout, Appl. Acoust. **41**, 299 (1994).

[10] J. Blitz and G. Simpson, *Ultrasonic Methods of Non-destructive Testing* (Champman & Hall, London, 1996).

[11] I. Baillie, P. Grifith, and S. Dixon, Insight **49**, 87 (2007).

[12] D. Cannon, K. Edel, S. Grassie, and K. Sawley, Fatigue Fract. Eng. Mater. Struct. **26**, 865 (2003).

[13] T. Swift, Int. J. Fatigue **16**, 75 (1994).

[14] *Boiler and Pressure Vessel Code, Section XI, Rules for in-Service Inspection of Nuclear Power Plant Components* (ASME, 2001).

[15] S. Mizoguchi, Ann. Rev. Mater. Sci. **11**, 151 (1981).

[16] J. Laing, *Machine for Making Pipes of Lead and Other Soft Metals,* (U.S. patent no. 3023, 1843).

[17] B. Tarmann and W. Poppmeier, Iron Steel Inst. London Spec. Rep. **89**, 131 (1965).

[18] J. Veitch-Michaelis *et al.*, 2016 13th Conference on Computer and Robot Vision (CRV) (2016).

[19] J. Brimacombe and K. Sorimachi, Metall. Trans. B **8B**, 489 (1977).

[20] V. S. Rutes, N. M. Lapotyshkin, V. Y. Genkin, and M. G. Chigrinov, Stal Engl. USSR **6**, 631 (1969).

[21] Y. Nakano, Y. Noguchi, F. Hoshi, and Y. Muranaka, Metals Society/IRSID Conference on Continuous Casting, (1976).

[22] H. Schrewe and K. Wuennenberg, Steelmaking Proc. AIME **61**, 335 (1978).

[23] H. Vom Ende and G. Vogt, J. Iron Steel Inst. **210**, 889 (1972).

[24] M. Reger, V. Balazs, and R. Josza, Acta Polytechnica Hungarica **11**, 119 (2014).

[25] X. Yang, Q. Xu, C. Wu, and Y. Chen, IOP Conf. Ser.: Mater. Sci. Eng. **283**, 1 (2017).

[26] D. Hurtuk and A. Tzavaras, JOM , 40 (1982).

[27] W. Tiller and J. Rutter, Can. J. Phys. **34**, 96 (1956).

[28] J. Feng and X. H. Shi, Metallurgical Industry Press **154** (2005).

[29] W. Irving, *Continuous Casting of Steel* (The institute of Materials, 1993).

[30] N. Vanaparthy and M. Srinivasan, Modell. Simul. Mater. Sci. Eng. **6**, 237 (1998).

[31] T. Pikkarainen, V. Vuorenmaa, I. Rentola, M. Leinonen, and D. Porter, IOP Conf. Ser.: Mater. Sci. Eng. **117**, 1 (2016).

[32] G. Van Drunen and J. Brimacombe, Ironmaking Steelmaking **2**, 125 (1975).

[33] J. Brimacombe, *Continuous Casting, Heat Flow, Solidification and Crack Formation vol 2* (The Institute of Materials, 1984).

[34] P. Drozdz, Arch. Metall. Mater. **62**, 911 (2017).

[35] N. Gupta and S. Chandra, ISIJ Int. **44**, 1517 (2004).

[36] C. Herrera, D. Ponge, and D. Raabe, Steel Res. Int. **79**, 482 (2008).

[37] P. Xu, F. Yin, and K. Nagai, Mater. Trans. **45**, 2456 (2004).

[38] J. See, Hum. Factors **57**, 1427 (2015).

[39] M. Yanoff and S. Duker, *Ophthalmology* (Elsevier Health Sciences, 2009).

[40] C. Harding and G. Hugo, *Review of Literature on Probability of Detection for Liquid Penetrant Nondestructive Testing* (Maritime Platforms Division DSTO Defence Science and Technology Organisation, 2011).

[41] D. Popescu, F. Anania, C. Cotet, and C. Amza, Int. J. Simul. Process Model. **12**, 82 (2013).

[42] M. Stadthaus, Insight **39**, 882 (1997).

[43] S. Burke and R. Ditchburn, *Review of Literature on Probability of Detection for Magnetic Particle Nondestructive Testing* (Maritime Platforms Division DSTO Defence Science and Technology Organisation, 2013).

[44] R. Barnes and D. L. Atherton, NDT & E Int. **26**, 3 (1993).

[45] W. Han, Russ. J. Nondestr. Test. **44**, 184 (2008).

[46] Z. Zhang, Y. Zhang, L. Udpa, and S. S. Udpa, Rev. Prog. in Quant. Nondestr. Eval **16**, 1307 (1997).

[47] Z. Wang, Y. Gu, and Y. Wang, J. Magn. Magn. Mater. **324**, 382 (2012).

[48] W. Gilboy, Nucl. Instrum. Methods Phys. Res. **221**, 193 (1984).

[49] P. Withers, Mater. Today **10**, 26 (2007).

[50] M. Vollmer and K. Moellmann, *Infrared Thermal Imaging: Fundamentals, Research and Applications* (John Wiley and Sons, 2011).

[51] V. Vavilov, Quant. InfraRed Thermogr. **11**, 66 (2014).

[52] C. Ibarra-Castanedo *et al.*, Infrared Phys. Technol. **46**, 75 (2004).

[53] V. Vavilov, NDT & E Int. **71**, 23 (2015).

[54] B. Wiecek, Proc. 2005 IEEE, Eng. Med. Biol. , 686 (2005).

[55] Y. Y. Hung *et al.*, Mater. Sci. Eng., R **64**, 73 (2009).

[56] R. Usamentiaga *et al.*, Sensors **14**, 12305 (2014).

[57] J. Garcia-Martin, J. Gomez-Gil, and E. Vazquez-Sanchez, Sensors **11**, 2525 (2011).

[58] G. Tian, Z. Zhao, and R. Baines, Sens. Actuators, A **69**, 148 (1998).

[59] N. Kasai, S. Ogawa, T. Oikawa, K. Sekine, and K. Hasegawa, J. Nondestr. Eval. **29**, 175 (2010).

[60] B. Abu-Nabah and P. Nagy, NDT & E Int. **40**, 555 (2007).

[61] R. Ko and S. Pipenbery, Rev. Prog. Quant. Nondestr. Eval. **14**, 755 (1995).

[62] K. Kaiser, *Electromagnetic Shielding* (CRC Press, 2004).

[63] D. Park, C. Angani, M. Kishore, G. Vertesy, and D. Lee, J. Magn. **18**, 342 (2013).

[64] A. Bernieri, G. Betta, L. Ferrigno, and M. Laracca, IEEE Trans. Instrum. Meas. **62**, 544 (2013).

[65] G. Tian, Y. Li, and C. Mandache, IEEE Trans. Magn. **45**, 184 (2009).

[66] R. Hughes, Y. Fan, and S. Dixon, NDT & E Int. **66**, 82 (2014).

[67] J. Krautkraemer and H. Krautkraemer, *Ultrasonic Testing of Materials* (Springer Verlag, 1983).

[68] R. Thompson, IEEE Ultrasonics Symposium **1**, 735 (1996).

[69] S. Tretbar, P. Plinkert, and P. Federspil, IEEE Trans. Biomed. Eng. **56**, 733 (2009).

[70] J. Rose, *Ultrasonic Waves in Solid Media* (Cambridge University Press, 1999).

[71] S. Davies, C. Edwards, G. Taylor, and S. Palmer, J. Phys. D: Appl. Phys. **26**, 329 (1993).

[72] W. Grandia, IEEE Ultrasonics Symposium , 697 (1995).

[73] R. Hanke, A. Kugel, and P. Troup, World Conference on NDT (2004).

[74] P. Myrach *et al.*, 19th World Conference on Non-Destructive Testing **21**, 1 (2016).

[75] F. He, D. He, Z. Deng, A. Xu, and N. Tian, Ironmaking Steelmaking **42**, 194 (2015).

[76] Y. Iizuka and Y. Awajiya, J. Phys. Conf. Ser. **520**, 012011 (2014).

[77] G. Alers and H. Wadley, Rev. Prog. Quant. Nondestr. Eval. **6A**, 627 (1987).

[78] H. Kolsky, *Stress Waves in Solids* (New York: Dover, 1963).

[79] G. Arfken, H. Weber, and F. Harris, *Mathematical Methods for Physicists* (Academic Press, 2013).

[80] I. Viktorov, *Rayleigh and Lamb Waves* (Plenum Press, New York, 1967).

[81] R. Edwards, S. Dixon, and X. Jian, Ultrasonics **44**, 93 (2006).

[82] C. Thring, Y. Fan, and R. Edwards, NDT&E Int. **81**, 20 (2016).

[83] C. Huygens, *Treatise on Light (English Translation)* (London: Macmillan, 1912).

[84] P. Laugier and G. Haiat, *Bone Quantitative Ultrasound* (Springer Science and Business Media, 2011).

[85] E. Papadakis, J. Appl. Phys. **34**, 265 (1963).

[86] R. Smith, W. Reynolds, and H. Wadley, Metal Science **15**, 554 (1981).

[87] H. Huntington, J. Acoust. Soc. Am **22**, 362 (1950).

[88] R. White, J. Acoust. Soc. Am **30**, 771 (1958).

[89] J. Faran, J. Acoust. Soc. Am **23**, 405 (1951).

[90] Y. Liu, R. Wu, and C. Ying, Geophys **142**, 439 (2000).

[91] J. Tichy, J. Erhart, E. Kittinger, and J. Privratska, *Fundamentals of Piezoelectric Sensorics* (Springer Verlag Berlin, 2014).

[92] C. Brown, R. Kell, R. Taylor, and L. Thomas, IRE Trans. Compon. Parts **100**, 99 (1962).

[93] H. Tao and J. Wu, J. Mater. Chem. C **5**, 1601 (2017).

[94] A. Castellano *et al.*, Composites B **66**, 299 (2014).

[95] J. Chen, X. Tan, W. Jo, and J. Roedel, J. Appl. Phys. **106**, 034109 (2009).

[96] S. Abrahams, H. Levinstein, and J. Reddy, J. Phys. Chem. Solids **27**, 1019 (1966).

[97] B. Tittmann and M. Aslan, Jpn. J. Appl. Phys., Part 1 **38**, 3011 (1999).

[98] F. Cegla, P. Cawley, J. Allin, and J. Davies, IEEE T. Ultrason. Ferr. **58**, 156 (2011).

[99] R. White, J. Appl. Phys. **34**, 3559 (1963).

[100] I. Veres, T. Bere, and P. Burgholzer, Ultrasonics **53**, 141 (2013).

[101] G. Taylor, C. Edwards, and S. Palmer, Nondestr. Test. Eval. **5**, 135 (1990).

[102] A. Hoffmann and W. Arnold, Appl. Surf. Sci. **96-98**, 71 (1995).

[103] T. Murray and J. Wagner, J. Appl. Phys. **85**, 2031 (1999).

[104] T. Kundu, *Ultrasonic Nondestructive Evaluation: Engineering and Biological Material Characterization* (CRC Press, 2003).

[105] R. Dewhurst and Q. Shan, Meas. Sci. Technol. **10**, R139R168 (1999).

[106] M. Hirao and H. Ogi, *EMATs for Science and Industry* (Springer Science and Business Media, 2003).

[107] M. Yang *et al.*, Rare Met. **37**, 983 (2018).

[108] X. Jian, I. Baillie, and S. Dixon, J. Phys. D: Appl. Phys. **40**, 1501 (2007).

[109] F. Hernandez-Valle and S. Dixon, NDT & E Int. **43**, 171 (2010).

[110] D. Rueter, Ultrasonics **65**, 200 (2016).

[111] X. Jian, S. Dixon, R. Edwards, and J. Morrison, Ultrsonics **44**, 653 (2006).

[112] M. Miller, M. Bao, K. Akio, and C. Ume, Mechatronics **12**, 1259 (2002).

[113] S. Dixon, C. Edwards, and S. Palmer, Rev. Prog. Quant. Nondestr. Eval. **18**, 1995 (1999).

[114] R. McMaster, *Nondestructive Testing Handbook* (The Ronald Press Company, 1963).

[115] B. Drinkwater and P. Wilcox, NDT&E Int. **39**, 525 (2006).

[116] C. Wong *et al.*, Ultrasonics **73**, 181 (2017).

[117] R. Dunki-Jacobs and L. Thomas, Rev. Prog. Quant. Nondestr. Eval. **11**, 805 (1992).

[118] C. Holmes, B. Drinkwater, and P. Wilcox, NDT&E Int. **38**, 701 (2005).

[119] Oralkan *et al.*, IEEE T. Ultrason. Ferr. **49**, 1596 (2002).

[120] T. Lukomski, Ultrasonics **70**, 241 (2016).

[121] F. Kremkau and J. Taylor, J. Ultrasound Med. **5**, 227 (1986).

[122] P. Barthez, R. Leveille, and P. Scrivani, Radiology and Ultrasound **38**, 387 (1997).

[123] B. Steinberg, *Principles of Aperture and Array System Design* (Wiley, New York, 1976).

[124] J. Isla and F. Cegla, Ultrasonics **78**, 1 (2017).

[125] J. Lehane and P. Thonemann, Proc. Phys. Soc. **85**, 301 (1965).

[126] A. Jonscher, Br. J. Appl. Phys. **15**, 365 (1964).

[127] F. Chen, Plasma Sources Sci. Technol. **24**, 014001 (2015).

[128] K. Saermark and P. Larsen, Phys. Lett. **24 A**, 374 (1967).

[129] E. Dobbs, J. Phys. Chem. Solids **31**, 1657 (1970).

[130] J. Houck, H. Bohm, B. Maxfield, and J. Wilkins, Phys. Rev. Lett. **12**, 224 (1967).

[131] A. Betjemann, H. Bohm, D. Meredith, and E. Dobbs, Phys. Lett. **25A**, 753 (1967).

[132] P. Petcher, M. Potter, and S. Dixon, NDT&E Int. **65**, 1 (2014).

[133] P. Ostiguy, N. Quaegbeur, and P. Masson, NDT&E Int. **76**, 17 (2015).

[134] H. Ogi, M. Hirao, and T. Ohtani, IEEE T. Ultrason. Ferr. **46**, 341 (1999).

[135] C. Vasile and R. Thompson, J. Appl. Phys. **50**, 2583 (1978).

[136] D. Griffiths, *Introduction to Electrodynamics* (Prentice-Hall, Upper Saddle River, New Jersey, 1999).

[137] R. Ribichini, P. Nagy, and H. Ogi, NDT & E Int. **51**, 8 (2012).

[138] P. Drude, *The Theory of Optics* (Academic Press, New York, 1999).

[139] S. Blundell, *Magnetism in Condensed Matter* (Oxford University Press, Oxford, 2001).

[140] Y. Mnyukh, Am. J. Condens. Mater. Phys. **4**, 78 (2014).

[141] Y. Wan, D. Fang, and K. Hwang, Int. J. Non Linear Mech. **38**, 1053 (2003).

[142] H. Ogi, E. Goda, and M. Hirao, Jpn. J. Appl. Phys. **42**, 3020 (2003).

[143] M. Gori, S. Giamboni, E. D'Alessio, S. Ghia, and F. Cernuschi, Ultrasonics **34**, 339 (1996).

[144] R. Taherian, *Electrical Conductivity in Polymer-Based Composites: Experiments, Modelling and Applications* (Elsevier Inc., 2019).

[145] D. Rueter and T. Morgenstern, Ultrasonics **54**, 2141 (2014).

[146] J. Wait and K. Spies, Can. J. Phys. **27**, 2731 (1969).

[147] P. Bannister, Radio Sci. **21**, 605 (1986).

[148] D. Boteler and R. Pirjola, Geophys. J. Int. **132**, 31 (1998).

[149] N. Wilson and P. Bunch, Conference Record of the 1991 IEEE Particle Accelerator Conference , 2322 (1991).

[150] J. Woolman and R. Mottram, *The mechanical and physical properties of the British Standard En steels (B.S. 970-1955)* (Oxford: Pergamon, 1969).

[151] X. Tang, Z. Zhenya, and M. Toksz, J. Acoust. Soc. Am. **95**, 71 (1994).

[152] D. Gridin, J. Acoust. Soc. Am. **105**, 2565 (1999).

[153] E. Kausel, Proceedings of the Royal Society A **469** (2013).

[154] G. Wojcik, D. Vaughan, N. Abboud, and J. Mould, IEEE Ultrasonics Symposium Proceedings , 11071112 (1993).

[155] N. Neogi, D. Mohanata, and P. Dutta, EURASIP Journal on Image and Video Processing **50** (2014).

[156] G. Goode and R. Lewis, Non-Destructive Testing , 313 (1975).

[157] G. Canella and F. Monti, NDT Int. , 10 (1980).

[158] X. Jian, I. Baillie, and S. Dixon, J. Phys. D: Appl. Phys. **40**, 1501 (2007).

[159] C. Scruby and B. Moss, NDT & E Int. **26**, 177188 (1993).

[160] E. Papadakis, L. Lynnworth, K. A. Fowler, and E. H. Carnevale, J. Acoust. Soc. Am **52**, 850 (1972).

[161] H. Ogi and M. Hirao, J. Acoust. Soc. Am. **103**, 2411 (1998).

[162] T. Takishita, K. Ashida, N. Nakamura, H. Ogi, and M. Hirao, Jpn. J. Appl. Phys **54**, 07HC04 (2015).

[163] D. Rueter, Sensors **17**, 926 (2017).

[164] N. Pradhan *et al.*, Scand. J. Metall. **34**, 232 (2005).

[165] D. Bhattacharya, T. Roy, and V. Mahashabde, J. Fail. Anal. Prev. **16**, 95 (2016).

[166] M. da Cunha and J. Jordan, Frequency Control Symposium and Exposition, 2005. Proceedings of the 2005 IEEE Int. , 426 (2005).

[167] O. Rompelman and H. Ros, J. Biomed. Eng. **8**, 24 (1986).

[168] B. Dupont and F. Berthelot, Characterization of small defects using total focusing method, in *11th European Conference on Non-Destructive Testing, Prague, Czech Republic*, 2014.

[169] L. Jeune, S. Robert, and E. Lopez Villaverde, Ultrasonics **64**, 128 (2016).

[170] S. Bannouf, S. Robert, O. Casula, and C. Prada, J. Phys. Conf. Ser. **457**, 012007 (2013).

[171] C. He *et al.*, Int. J. Acoust. Vibr. **22**, 541 (2017).

[172] K. Hall, Non-Destr. Test. **9**, 121 (1976).

[173] D. Zeitvogel *et al.*, NDT&E Int. **62**, 144 (2014).

[174] E. Burstein, H. Talaat, J. Schoenwald, J. Quin, and E. Lean, IEEE Ultrasonics Symposium Proceedings **73**, 564 (1973).

[175] T. Moran and R. Panos, J. Appl. Phys. **47**, 2225 (1976).

[176] X. Jian, S. Dixon, and R. Edwards, Nondestr. Test. Eval. **20**, 43 (2005).

[177] P. Stepanishen, J. Acoust. Soc. Am. **49**, 1629 (1971).

[178] J. A. Jensen, J. Acoust. Soc. Am. **89**, 182 (1991).

[179] C. Zou *et al.*, Sensors **16**, 1873 (2016).

[180] J. Cheng, J. Lu, W. Lin, and Y. Qin, Ultrasonics **5**, 229237 (2011).

[181] Comsol multiphysics® v. 5.3a, www.comsol.com, COMSOL AB Stockholm, Sweden.

[182] W. Shi *et al.*, Nondestr. Test. Eval. **33**, 56 (2018).

[183] X. Song and G. Qiu, Sensors **17**, 2722 (2017).

[184] P. Yi, K. Zhang, Y. Li, and X. Zhang, Sensors **14**, 19687 (2014).

[185] E. Villaverde, S. Robert, and C. Prada, J. Acoust. Soc. Am **140**, 541 (2016).

[186] R. Ludwig, Z. You, and R. Palanisamy, IEEE Trans. Magn. **29**, 2081 (1993).

[187] S. Thomas, S. Obayya, R. Taneja, and W. Balachandran, Int. J. Comput. Methods Eng. Sci. Mech. **10**, 124 (2009).

[188] R. Jafari-Shapoorabadi, A. Konrad, and A. Sinclair, IEEE Trans. Magn. **37** (2001).

[189] M. Kaltenbacher, K. Ettinger, and R. Lerch, IEEE Trans. Magn. **35**, 1610 (1999).

[190] Y. Xie, W. Yin, Z. Liu, and A. Peyton, Ultrasonics **66**, 154 (2016).

[191] Y. Li, T. Theodoulidis, and G. Tian, IEEE Trans. Magn. **43**, 4010 (2007).

[192] X. Jian and S. Dixon, Sens. Actuators, A **136**, 132 (2007).